



TECHNISCHE  
UNIVERSITÄT  
MÜNCHEN

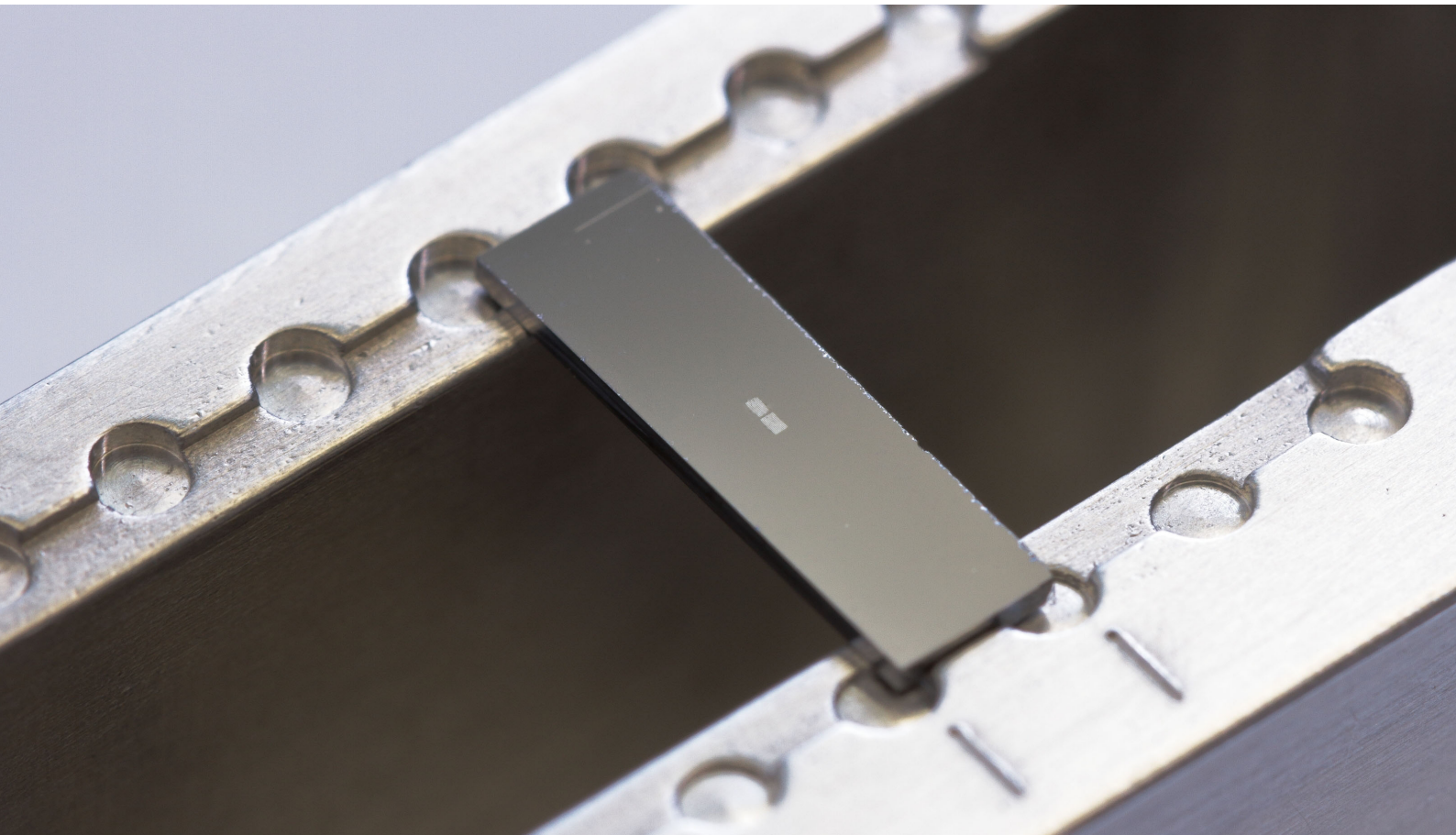


WALTHER - MEISSNER -  
INSTITUT FÜR TIEF -  
TEMPERATURFORSCHUNG



BAYERISCHE  
AKADEMIE DER  
WISSENSCHAFTEN

# A scalable 3D quantum memory



**PhD Thesis**

Edwar Xie

Supervisor: Prof. Dr. Rudolf Gross

Munich, September 2018



# TECHNISCHE UNIVERSITÄT MÜNCHEN

Lehrstuhl E23 für Technische Physik

Walther-Meißner-Institut für Tieftemperaturforschung  
der Bayerischen Akademie der Wissenschaften

## **A scalable 3D quantum memory**

Edwar Xie

Vollständiger Abdruck der von der Fakultät für Physik der Technischen  
Universität München zur Erlangung des akademischen Grades eines

**Doktors der Naturwissenschaften**

genehmigten Dissertation.

Vorsitzender:

Prüfer der Dissertation: 1. Prof. Dr. Rudolf Gross

2.

Die Dissertation wurde am \_\_\_\_\_ bei der Technischen Universität München  
eingereicht und durch die Fakultät für Physik am \_\_\_\_\_ angenommen.



Dedicated to my hard-working parents  
谢盛友 and 张申华



# Abstract

Nowadays, quantum computing using superconducting circuits is on the cusp of being the supreme technology as compared to digital computing. The advantageous resources over digital computing, such as quantum superposition states and entanglement, also pose a challenge on the memories for such states due to quantum mechanical restrictions. One type of storage is the encoding of quantum information in photons, which are trapped in superconducting 3D microwave resonators. The photon lifetimes are relatively long in such systems due to small losses in the superconducting material. Nevertheless, there are two particular drawbacks with such memories. First, the 3D cavity architecture is bulky in comparison to its (less coherent) 2D counterpart. Second, the huge quality factors  $Q$  of the 3D microwave cavities result in a long cavity ring down and, in turn, in long readout times. A more scalable device with fast readout can be built by exploiting the multi-mode structure of the 3D cavity. In such configuration, one high- $Q$  mode can be used for storage, while another low- $Q$  mode can be used for readout. In this work, we present an experimental study on such a device: a transmon qubit capacitively coupled to two distinct modes of a single 3D microwave cavity. We analyze the system parameters of such a device and implement a quantum information storage protocol. Finally, we find that our device offers a fast readout capability simultaneously with a cavity enhanced coherence time, which is limited only by the internal quality factor of the superconducting cavity.

## Kurzfassung

Die Quanteninformationsverarbeitung basierend auf supraleitenden Schaltkreisen steht heutzutage kurz davor, eine führende Technologie zu werden. Im Vergleich zur klassischen, digitalen Informationsverarbeitung ergeben sich Vorteile durch die Ausnutzung von genuinen Quanten-Ressourcen wie Superposition und Verschränkung. Gleichzeitig stellen diese jedoch aufgrund quantenmechanischer Einschränkungen eine neuartige Herausforderung für die Speicherung solcher Zustände dar. Eine Möglichkeit besteht darin, die Quanteninformation in Form von Photonen zu speichern, welche sich in einem supraleitenden 3D Mikrowellenresonator befinden. Bedingt durch die besonderen Materialeigenschaften des Supraleiters, nämlich die nahezu verlustfreie Stromleitung, ist die Lebensdauer solcher Photonen relativ hoch. Trotzdem weist diese Art von Speicher zwei grundlegende Nachteile auf. Erstens benötigt die 3D Hohlraumarchitektur mehr Platz als ähnliche Systeme mit planarer Geometrie, welche aber wiederum über geringere Kohärenzzeiten verfügen. Zweitens führen die hohen Gütefaktoren der 3D Mikrowellenresonatoren zu langen Einschwing- und Abklingzeiten, welche die Auslesegeschwindigkeit beeinträchtigen. Durch Ausnutzung der Multimodenstruktur eines 3D Hohlraumresonators kann ein Speicher mit einer höheren Skalierbarkeit und einer kurzen Auslesezeit konstruiert werden. Hierfür wird eine Mode mit hoher Güte für die Speicherung verwendet und eine andere Mode mit geringer Güte für das Auslesen. Die vorliegende Arbeit beinhaltet eine experimentelle Studie eines solchen Speichers: ein Transmon Quantenbit ist kapazitiv an zwei unterschiedliche elektromagnetische Moden eines einzigen 3D Mikrowellenresonators gekoppelt. Die Parameter dieses System werden analysiert und ein Protokoll für das Speichern von Quanteninformation wird implementiert. Schlussendlich wird gezeigt, dass diese Art von Speicher eine schnelle Auslese ermöglicht und gleichzeitig eine durch den Hohlraumresonator gesteigerte Kohärenzzeit besitzt. Diese ist im Idealfall nur durch den internen Gütefaktor des supraleitenden Resonators begrenzt.

*"And the light shineth in darkness;  
and the darkness comprehended it not."*

The Gospel of John

# Contents

<b>Introduction</b>	<b>1</b>
<b>1 Theory of dispersive circuit QED</b>	<b>5</b>
1.1 3D waveguide cavity . . . . .	5
1.1.1 Cavity eigenmodes and quantum states . . . . .	5
1.1.2 External coupling and photon lifetimes . . . . .	8
1.1.3 Internal damping mechanisms . . . . .	10
1.2 The superconducting transmon qubit . . . . .	14
1.2.1 Quantum bits . . . . .	14
1.2.2 The Josephson junction . . . . .	15
1.2.3 The transmon circuit . . . . .	17
1.3 Strong coupling of qubit and cavity . . . . .	20
1.3.1 Jaynes-Cummings Hamiltonian . . . . .	20
1.3.2 Dispersive Hamiltonian . . . . .	21
1.4 Dynamics of a driven qubit-cavity system . . . . .	25
1.4.1 Excitation of sideband transitions . . . . .	25
1.4.2 Energy relaxation and dephasing . . . . .	27
1.4.3 Purcell effect . . . . .	28
1.4.4 Dephasing of a quasi-harmonic mode . . . . .	29
<b>2 Methods and techniques</b>	<b>31</b>
2.1 Fabrication . . . . .	31
2.1.1 3D cavity design . . . . .	31
2.1.2 Transmon qubit design . . . . .	39
2.1.3 Fabrication of Josephson junctions . . . . .	42
2.2 Qubit spectroscopy . . . . .	49
2.2.1 Cryogenic setup . . . . .	49
2.2.2 Single-tone transmission measurement . . . . .	51
2.2.3 Single-tone determination of the dispersive shift . . . . .	53
2.2.4 Two-tone measurement and higher qubit levels . . . . .	54
2.2.5 AC Stark shift and photon number calibration . . . . .	56
2.2.6 Triple-tone measurement . . . . .	58
2.3 Time domain measurements . . . . .	63

2.3.1	Pulse generation setup . . . . .	64
2.3.2	Basic pulse protocols and automatic tune-up . . . . .	65
2.3.3	Pulse shaping . . . . .	66
2.3.4	Qubit phase control . . . . .	69
2.3.5	IQ-mixer calibration . . . . .	70
2.3.6	Quantum state tomography . . . . .	72
2.3.7	Quantum process tomography . . . . .	75
2.3.8	Suppression of state leakage . . . . .	79
<b>3</b>	<b>Results</b>	<b>83</b>
3.1	Quantum memory protocol . . . . .	83
3.1.1	Optimized storage and readout mode . . . . .	84
3.1.2	Memory pulse sequence . . . . .	87
3.2	Coherent population transfer and decoherence effects . . . . .	87
3.3	Enhanced quantum information storage time . . . . .	89
3.3.1	Higher cavity memory modes . . . . .	93
3.3.2	Storage of superposition states . . . . .	94
3.4	Quantum memory fidelity . . . . .	95
3.4.1	Reduction of fidelity variation . . . . .	96
3.4.2	State leakage fidelity limit . . . . .	97
<b>4</b>	<b>Conclusions and Outlook</b>	<b>99</b>
<b>A</b>	<b>Experimental setup details</b>	<b>103</b>
A.1	Measurement strategy . . . . .	103
A.2	Band-pass filter for RF drive line . . . . .	103
A.3	Direct measurement of coherent state decay . . . . .	104
<b>B</b>	<b>Sample overview</b>	<b>105</b>
B.1	Cavity samples . . . . .	105
B.2	Qubit samples . . . . .	105
B.3	Sample fabrication recipe . . . . .	105
<b>C</b>	<b>FEM simulation with CST</b>	<b>109</b>
C.1	Cavity simulation models . . . . .	109
C.2	Frequency solver . . . . .	110
C.3	Eigenmode solver . . . . .	110
<b>D</b>	<b>Maximum likelihood estimation</b>	<b>111</b>
D.1	MLE for the density matrix . . . . .	111
D.2	MLE for the process matrix . . . . .	112

---

<b>E Additional measurement data</b>	<b>115</b>
E.1 Quantum state tomography and quantum process tomography of a single qubit . . . . .	115
E.2 Quantum process tomography of the quantum memory protocol . . . . .	116
<b>Bibliography</b>	<b>119</b>
<b>List of publications</b>	<b>132</b>
<b>Acknowledgments</b>	<b>135</b>

# Introduction

A memory has the purpose of recording information, storing it and releasing it after a certain time. This idea of using a memory for information storage and retrieval can be found throughout the whole history of mankind. In the beginning, information was stored and retrieved by passing on stories and tales orally [1]. Later on, information could be stored in written word and retrieved by later generations [2]. The invention of the printing press in the 15th century [3] made it possible to store information in many redundant copies and with increased fidelity. Nowadays, information technology, based on the fundamental principle of storing and retrieving information, has grown to a massive pillar of modern civilization. In a simplified picture, the operation method of a computer relies on countless information storage and retrieval processes [4]. We observe, that the information density and the total capacity of memories have grown throughout the centuries from orally told stories to redundantly stored information in a computer. However, all these resources mentioned above have one thing in common: they are purely classical.

Considering the storage and retrieval of quantum information, the challenge is more complex. This is the case, because the conditions for faithful quantum information storage are much more difficult to fulfill than those for the storage of classical information. In strong contrast to the classical realm, we face the no-cloning theorem [5], which forbids to redundantly store information. Furthermore, the uncontrolled loss of information to the environment is many orders of magnitude higher in quantum systems [6, 7]. As a result, quantum resources are fairly fragile and decay on a short timescale. Nevertheless, if such constraints can be circumvented, the idea of a quantum computer, which can store and process quantum information, is indeed very appealing [8, 9], because a quantum computer is mathematically proven to outperform a classical supercomputer in specific tasks such as database search algorithms [10] or prime factorization [11]. Moreover, engineered quantum systems are a versatile resource for quantum communication [12, 13], quantum simulation [14] and quantum cryptography [15].

One of the most promising platforms for quantum computing today is found in the field of circuit quantum electrodynamics (circuit QED) [16–18]. Here, superconducting circuits act as quantum bits (qubits) [19]. In circuit QED, one method to increase the information storage time is to isolate the quantum resource from the environment [20]. This is typically done by coupling the qubit to a superconducting resonator for precise control of the environment [21] and for readout [17, 22]. Physically, this isolation limits

the information leakage to the environment. Consequently, the difficulty of retrieving the information is increased just as much as the storage time is extended. In the end, however, a fast retrieval and a long storage time are required simultaneously.

In this work, the isolated environment is provided by a superconducting 3D microwave cavity. Such superconducting cavities are known for decades from particle physics, where low loss is a crucial criterion for generating high energy particle beams at reduced operation costs [23, 24]. The application of 3D cavities in the field of circuit QED, however, is relatively recent. When qubits were placed the first time in a superconducting 3D cavity [21], the coherence times jumped almost one order of magnitude [25] compared to previous systems with planar 2D resonators. The microwave 3D cavity architecture has opened up a variety of interesting experiments on the Quantum Zeno effect [26, 27], on magnetic YIG spheres coupled to a qubit [28], on wireless Josephson parametric amplifiers [29] and on quantum trajectories of qubits [30]. The manipulation of Fock states [31, 32] and of Schroedinger cat states [33, 34] is facilitated due to the long photon lifetimes provided by the cavities. Furthermore, CNOT gates between two multiphoton cavity qubits [35] and resonator-induced phase gates with up to 5 qubits [36] have been demonstrated. The inevitable bulkiness of 3D cavities has led to architectures comprising compact 2D structures [37] and to networks of multiple 3D cavities [38–40].

In this work, our simple carrier and processor of quantum information, a single qubit, is fully enclosed by the cavity. The cavity itself can be designed to decay much slower than the qubit. For extending the lifetime of a quantum state during idling times, it is possible to intermediately store the qubit state in such a long-lived resonator. In terms of coherence, superconducting microwave 3D cavity resonators yield the best results so far, reaching the millisecond scale [41, 42]. Other memory systems are constructed using 2D resonators [43], microscopic defect states [44], nano-mechanical oscillators [45], electron spin ensembles [46, 47] and nuclear spins [48].

With regard to the excellent control over the electromagnetic environment and the ability to precisely engineer a wide range of sample parameters as desired, we choose superconducting microwave 3D cavities for the construction of a quantum memory. Until now, the multimode structure of 3D cavities has mostly been seen as a source of irritation than a profitable feature. We, however, take advantage of this feature to create a compact and scalable quantum memory system, which will be useful as a building block for larger systems. In order to fulfill the requirement of a fast retrieval and a long storage, we have to optimize the cavity architecture towards this goal. In addition, we need to understand the qubit-cavity coupling mechanisms and how they can be carefully adjusted with respect to the demands. To this end, the design and fabrication of the qubit plays a crucial role and a reliable design routine and fabrication recipe has to be established. The experimental control knobs, namely the methods for quantum state preparation and manipulation, have to be adapted and extended to suit the quantum memory application. This includes an accurate and automatized

calibration scheme and the implementation of a memory pulse sequence. In terms of a working memory, we aim at a fidelity close to unity for state storage and retrieval.

The first chapter lays the theoretical foundation for this thesis. We start with a classical electromagnetic description of the waveguide cavity and include coupling mechanisms and internal damping effects (cf. Sec. 1.1). Then, the transmon qubit is reviewed (cf. Sec. 1.2), before we put the pieces together and describe the coupled qubit-cavity system (cf. Sec. 1.3). We close the chapter with a discussion of the dynamics of the qubit-cavity system (cf. Sec. 1.4).

In the second chapter, we report on design recipes for the 3D cavity and the transmon qubit (cf. Sec. 2.1). Subsequently, we introduce a set of qubit characterization measurements required to reliably determine the relevant fabrication parameters (cf. Sec. 2.2). The qubit dynamics is analyzed in the time domain with the focus on pulse shaping and the resulting improvements (cf. Sec. 2.3). Moreover, first measurements towards quantum state and quantum process tomography are discussed.

Finally, we present a functional quantum memory based on a high- $Q$  3D cavity. Necessary optimizations are reviewed and the memory pulse protocol is introduced (cf. Sec. 3.1). We show data from different stages of the memory protocol and discuss decoherence effects (cf. Sec. 3.2). Lastly, the memory is characterized in terms of its enhanced storage time and its fidelity (cf. Sec. 3.3). Limitations on the fidelity are analyzed for future improvements (cf. Sec. 3.4).

Moreover, with all the investigations at hand, we are able to estimate the technical optimizations necessary to enhance the memory storage time. In terms of scalability, we give options on how to increase the amount of stored quantum information by scaling from the current sample to larger systems.



# Chapter 1

## Theory of dispersive circuit QED

In this chapter, we review the theory of circuit QED. First, we introduce the two main components used in this work, which are a 3D waveguide cavity and a superconducting transmon qubit. The cavity is described in terms of its eigenmode spectrum and external and internal damping mechanisms. For the transmon qubit, we derive its anharmonic level structure caused by the non-linear Josephson inductance. Combining both, we arrive at a strongly coupled system of qubit and cavity. Here, we focus on the dispersive regime and sideband transitions due to the fixed frequency nature of our system. We conclude this chapter by looking at the system dynamics under an external drive and discuss decoherence effects with the help of the Lindblad formalism.

### 1.1 3D waveguide cavity

A 3D waveguide cavity relies on the principle of an electromagnetic wave subdued to specific boundary conditions. This is similar to quantum optics, where two mirrors are used to build an optical cavity [20]. For microwave light, superconducting waveguide cavities provide state-of-the-art coherence properties [42, 49], which makes them a successful tool in circuit QED.

#### 1.1.1 Cavity eigenmodes and quantum states

We start with defining a plane wave, which propagates through a lossless medium in  $z$  direction with the wavevector  $\vec{k} = (0, 0, k)$ .

$$\vec{E}(x, y, z) = E_y^+ \exp(-ikz) + E_y^- \exp(ikz) \quad (1.1)$$

Here,  $E_y^+$  and  $E_y^-$  are the amplitudes of the electric field, which oscillates in the  $y$ -direction. According to Maxwell's equations [51], the  $H$ -field oscillates perpendicular to the  $E$ -field. Both fields are orthogonal to the direction of propagation, which is characteristic for transverse electromagnetic waves. By placing conducting walls around

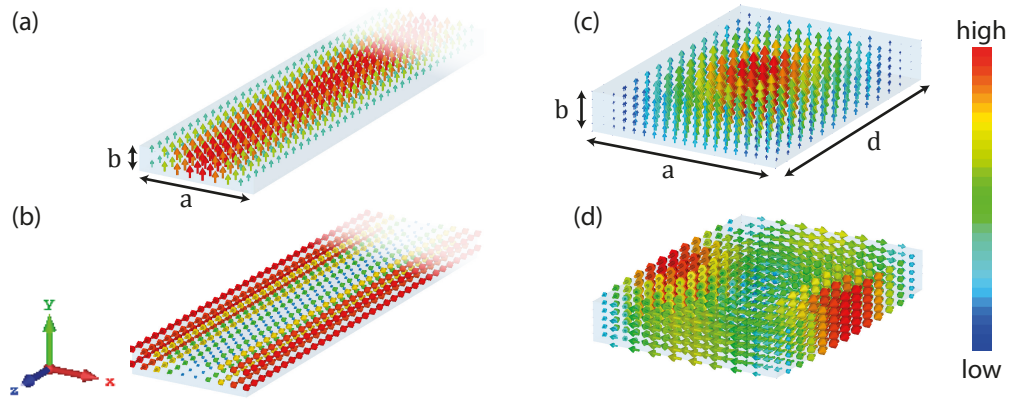


**Figure 1.1:** Drawing of (a) electric and (b) magnetic field for an infinitely long waveguide with cross-section  $a \times b$ . Shown is the fundamental mode. The magnetic and electric field are phase-shifted by  $90^\circ$ . (c) and (d) are the corresponding drawings for a waveguide cavity with the boundary condition  $\vec{E} = 0$  on all sides. Graphics are taken from CST Microwave Studio [50].

the propagation direction of the wave, one changes the boundary conditions<sup>1</sup> and obtains a waveguide with a rectangular cross-section of  $a \times b$  [cf. Fig. 1.1 (a)]. Then, only certain transverse electric (TE) or transverse magnetic (TM) modes can propagate [52]. We restrict ourselves to a discussion of the TE modes<sup>2</sup>, which are from a theoretical point of view equivalent to the TM modes. In a waveguide, the TE mode is expressed as

$$\vec{E}_t(x, y, z) = \vec{e}(x, y) \left[ E^+ \exp(-i\beta_{mn}z) + E^- \exp(i\beta_{mn}z) \right] \quad (1.2)$$

where  $\vec{e}(x, y)$  describes the transverse mode profile. The propagation constant of the  $m, n$ th mode is

$$\beta_{mn} = \sqrt{k^2 - \left(\frac{m\pi}{a}\right)^2 - \left(\frac{n\pi}{b}\right)^2}. \quad (1.3)$$

Now, we close the waveguide on both ends with conducting walls and a distance  $d$  in between [cf. Fig. 1.1 (b)]. To satisfy this new boundary condition,  $\vec{E}_t = 0$  for  $z = 0, d$  we have to solve the equation

$$\vec{E}_t(x, y, d) = -\vec{e}(x, y) 2E_0 i \sin(\beta_{mn}d) \stackrel{!}{=} 0 \quad (1.4)$$

which assumes  $E^+ = E^- = E_0$  for a perfectly reflecting surface. Hence, the argument of the sine needs to be an integer multiple of  $\pi$ :  $\beta_{mn}d = l\pi$  with  $l = 1, 2, 3, \dots$ . We identify these standing waves with the eigenmodes of the cavity. The frequency of these

<sup>1</sup>This is only valid if the frequency of the electromagnetic waves is smaller than the plasma frequency of the metal. Since the following experiments are carried out in the gigahertz regime, this assumption is fulfilled.

<sup>2</sup>The discussion of the TE and TM modes is found in Ref. [52]

TE $_{mnl}$  modes can be calculated as [52]

$$\nu_{mnl} = \frac{c}{2\pi\sqrt{\mu_r\epsilon_r}} \sqrt{\left(\frac{m\pi}{a}\right)^2 + \left(\frac{n\pi}{b}\right)^2 + \left(\frac{l\pi}{d}\right)^2} \quad (1.5)$$

with the relative permittivity  $\epsilon_r$  and the relative permeability  $\mu_r$  for media other than vacuum. The fundamental mode is referred to as the TE $_{101}$  mode. For cavities with a quadratic footprint,  $a = d$ , one finds degenerate mode frequencies such as  $\nu_{201} = \nu_{102}$ . From Eq. (1.5), we observe that, when changing only one mode number and keeping the other two constant, the mode frequencies have an equidistant spacing consistent with a 1D system such as a string.

We look at the quantum properties of a 3D waveguide cavity by introducing the quantum harmonic oscillator<sup>3</sup>, which is described by the textbook Hamiltonian

$$\mathcal{H}_{\text{osc}} = \hbar\omega_c \left( \hat{a}^\dagger \hat{a} + \frac{1}{2} \right) \quad (1.6)$$

with  $\omega_c$  being the oscillator frequency and  $\hat{a}^\dagger$  ( $\hat{a}$ ) the photon creation (annihilation) operator, respectively. Since the actual cavity is a multimode system, its Hamiltonian reads

$$\mathcal{H}_{\text{cavity}} = \hbar \sum_{m,n,l} \omega_{mnl} \left( \hat{a}_{mnl}^\dagger \hat{a}_{mnl} + \frac{1}{2} \right) = \hbar \sum_i \omega_i \left( \hat{n}_i + \frac{1}{2} \right) \quad (1.7)$$

with  $\hat{n} = \hat{a}^\dagger \hat{a}$  being the number operator and  $i$  being the index of the eigenmode in the ascending order of their frequencies. The eigenstates of the number operator are Fock states  $|n\rangle$  corresponding to  $n$  photons in the cavity:

$$\hat{n}|n\rangle = n|n\rangle. \quad (1.8)$$

However, in experiment, it is not easily possible to address such a photon number state directly due to the harmonicity of the cavity. A classical resonant drive on the cavity leads to a coherent state  $|\alpha\rangle$ , which is a Poisson-distributed superposition of Fock states:

$$|\alpha\rangle = \exp\left(-\frac{|\alpha|^2}{2}\right) \sum_{n=0}^{\infty} \frac{\alpha^n}{\sqrt{n!}} |n\rangle. \quad (1.9)$$

These are the eigenstates of the annihilation operator  $\hat{a}$  and we obtain  $\hat{a}|\alpha\rangle = \alpha|\alpha\rangle$ . The eigenvalue  $\alpha = |\alpha|e^{i\phi}$  is a complex number determined by the amplitude  $|\alpha|$  and phase  $\phi$  of the drive.

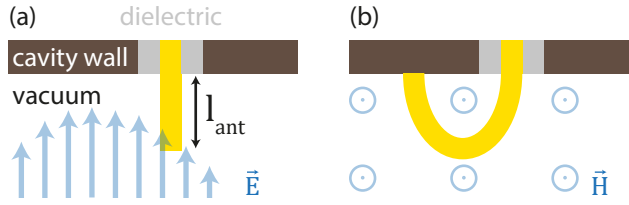


**Figure 1.2:** Schematic drawing of a (a) dipole antenna for electric field coupling and (b) loop antenna for magnetic field coupling.

### 1.1.2 External coupling and photon lifetimes

In order to excite the eigenmodes, energy has to be coupled into the cavity. Generally, one can couple to the electric field via stub antennas or to the magnetic field via loop antennas [cf. Fig. 1.2 (a) and Fig. 1.2 (b)]. We limit ourselves to stub antennas in this paragraph, since only these are used throughout this work. In this case, the coupling is capacitive and can be approximated as dipolar coupling with the dipole moment  $\vec{p}$ . Hence, we can write  $\hbar\kappa_x = \vec{p} \cdot \vec{E}(x,y,z)$ , where  $\kappa_x$  is the rate of photons excited in the cavity. The charge  $q$  in the dipole moment  $\vec{p} = q\vec{l}_{\text{ant}}$  can be calculated via  $q = C_x \int E_{\parallel,\text{ant}}(x,y,z)dy$ , where  $C_x$  is the coupling capacitance and  $E_{\parallel,\text{ant}}$  the electric field parallel to the direction of the stub antenna with length  $l_{\text{ant}}$ . Here, we let the antenna point in the  $y$ -direction. In conclusion, we obtain for the coupling rate

$$\kappa_x = \frac{C_x}{\hbar} \int_{-\infty}^{l_{\text{ant}}} E_{\parallel,\text{ant}}(x,y,z)dy \vec{l}_{\text{ant}} \cdot \vec{E}(x,y,z) \quad (1.10)$$

$$= \frac{C_x}{\hbar} \left( \int_{-\infty}^{l_{\text{ant}}} E_{\parallel,\text{ant}}(x,y,z)dy \right)^2. \quad (1.11)$$

For the last step, we assume a non-constant field in the  $y$ -direction and, hence, integrate the electric field along the antenna. As a result, the coupling depends on the field amplitude  $E_{\parallel,\text{ant}}(x,y,z)$  at the antenna position and the antenna dipole length  $l_{\text{ant}}$ . A carefully chosen position of the antenna enables us to set high or low coupling to specific cavity modes according to their electric field distribution. More details on the coupling based on the cavity geometry used for the experiments in this work are found in Sec. 2.1.1.

Antennas as input ports also serve as output ports. Photons, which enter the cavity, can also leave the cavity via the same or another port. The total rate, at which this happens, is defined as  $\kappa = 4\pi^2\Delta\nu$  with  $\Delta\nu$  being the linewidth of the cavity transmission<sup>4</sup>. To account for the total energy loss caused by the coupling to the output ports, one defines the external  $Q$ -factor. The  $Q$ -factor in general is the ratio of total

<sup>3</sup>For the derivation of circuit quantization, we refer the reader to Refs. [53, 54].

<sup>4</sup>This definition of the linewidth is valid, if the Lorentzian of the cavity transmission magnitude is

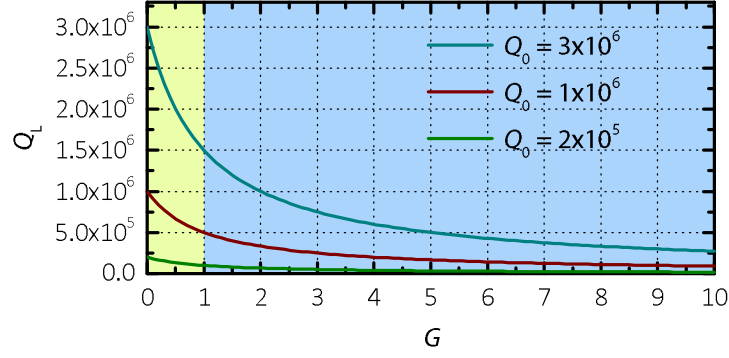


**Figure 1.3:** The loaded  $Q_L$  depending on the coupling coefficient  $G$  for three different internal  $Q$ -factors. The undercoupled regime is marked in green, the overcoupled regime in blue.

energy to dissipated energy [55].

$$Q_L \equiv \frac{2\pi \cdot \text{average energy stored}}{\text{energy loss/cycle}} = \frac{\hbar\omega}{\hbar\Delta\omega} = \frac{\nu}{\Delta\nu} \quad (1.12)$$

We can distinguish between external losses  $\kappa_x$  and internal losses  $\kappa_0$ . The causes for the latter ones are reviewed in the next section. In the end, the loaded  $Q$ -factor can be written as

$$\frac{1}{Q_L} = \frac{1}{Q_0} + \frac{1}{Q_x} = \frac{1}{Q_0}(1 + G). \quad (1.13)$$

The latter definition is expressed with a coupling coefficient  $G = Q_0/Q_x = \kappa_x/\kappa_0$ , which is proportional to the antenna length and the electric field at the antenna position according to Eq. (1.11). In experiment,  $Q_0$  is set by material parameters (cf. Sec. 1.1.3) and can be treated as constant. Hence, the coupling is  $G \propto 1/Q_x$ , meaning highly coupled cavities exhibit a low  $Q_x$  and vice versa. Moreover, the coupling coefficient helps us to distinguish between three regimes (cf. Fig. 1.3).

$$\begin{cases} Q_0 < Q_x, & G < 1, \text{ undercoupled} \\ Q_0 = Q_x, & G = 1, \text{ critically coupled} \\ Q_0 > Q_x, & G > 1, \text{ overcoupled} \end{cases} \quad (1.14)$$

The loaded  $Q$ -factor determines, how long a photon will circulate inside the cavity before being absorbed internally or having left the cavity through the output port.

---

defined as

$$L(\nu) = \frac{1}{2} \frac{\Delta\nu/2}{(\nu - \nu_c)^2 + (\Delta\nu/2)^2}$$

$$L(\omega) = \pi \frac{\Delta\omega/2}{(\omega - \omega_c)^2 + (\Delta\omega/2)^2}.$$

It is normalized such that  $L(\nu_c) = L(\omega_c) = 1$ .

Therefore, the average photon lifetime  $\bar{\tau}$  depends on the total quality factor as [56]

$$\bar{\tau} = \frac{Q_L}{\omega} = \frac{1}{\Delta\omega} = \frac{2\pi}{\kappa}. \quad (1.15)$$

With this knowledge, we can now estimate the power required to excite an average number  $\bar{n}$  of photons of frequency  $\omega$  inside the cavity [57],

$$P_{\text{in}} = \bar{n} \frac{\hbar\omega}{\bar{\tau}} = \bar{n} \hbar\omega \frac{\kappa}{2\pi}. \quad (1.16)$$

For a cavity with low internal losses, the output power almost equals the input power,  $P_{\text{in}} \simeq P_{\text{out}}$ . The practical importance of this equation is that a cavity with a large  $\kappa$  can be probed with a relatively high power while still keeping the average cavity photon number low. This relieves the requirements on signal amplification of the output signal. In the case of an overcoupled cavity, the rate  $\kappa$  imposes a limit on how fast quantum information can be retrieved from the cavity.

### 1.1.3 Internal damping mechanisms

Until now, we have assumed the damping to be solely external. This only holds for ideal systems. In reality, internal damping into uncontrolled channels plays an important role. In this section, we will introduce the mechanism of surface loss at the cavity walls and discuss the insertion of a lossy medium.

#### Surface losses

In the case of microwave 3D waveguide cavities, the electromagnetic field exists mainly in vacuum, which is lossless. Moreover, 3D cavities are advantageous in terms of surface loss, because the field is strongly diluted by a geometric factor at the material surface as compared to 2D planar resonators. The power loss at the surface of a conductor is caused by eddy currents induced by the oscillating magnetic field tangential to the surface [52] (cf. Fig. 1.4)

$$P_{\text{surf}} = \frac{R_{\text{surf}}}{2} \int_{\text{surf}} |H_t|^2 dx^2 \quad (1.17)$$

with  $R_{\text{surf}} = \sqrt{\omega\mu_0/2\sigma}$  being the surface resistance and  $\sigma$  the conductivity of the material. For a superconducting material, the surface resistance is  $R_{\text{surf}}^{\text{sc}} = R_{\text{BCS}} + R_{\text{res}}$ , where  $R_{\text{BCS}} \propto (\omega^2/T) \exp(-1.76T_c/T)$  is the BCS surface resistance [58] due to oscillating normal-conducting electrons and  $R_{\text{res}}$  is the residual resistance caused by lattice distortions and other defects. For the TE<sub>10</sub> $l$  mode in a rectangular cavity,  $H_t$

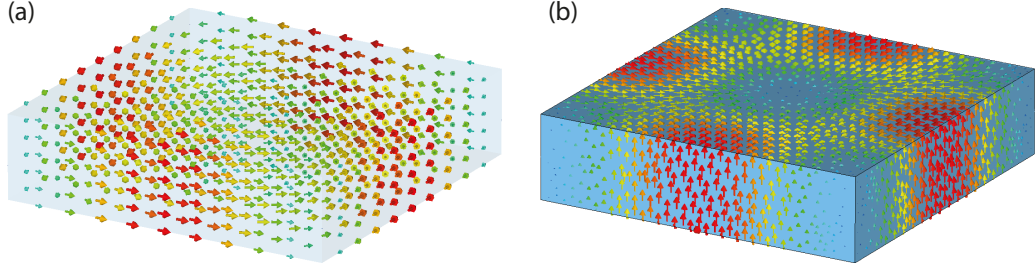


**Figure 1.4:** (a) Magnetic field in 3D cavity. (b) Surface current created by tangential magnetic field. Graphics are taken from CST Microwave Studio [50].

consists of components in  $x$  and  $z$  direction

$$H_x = \frac{-iE_0}{k} \sqrt{k^2 - \left(\frac{\pi}{a}\right)^2} \sqrt{\frac{\epsilon_0}{\mu_0}} \sin\left(\frac{\pi x}{a}\right) \cos\left(\frac{l\pi z}{d}\right) \quad (1.18)$$

$$H_z = \frac{iE_0 \pi}{k a} \sqrt{\frac{\epsilon_0}{\mu_0}} \cos\left(\frac{\pi x}{a}\right) \sin\left(\frac{l\pi z}{d}\right). \quad (1.19)$$

By calculating the integral in Eq. (1.17), one obtains the dissipated power at the surface

$$P_{\text{surf}} = \frac{R_{\text{surf}} \epsilon_0 E_0^2 \lambda^2}{8\mu_0} \left( \frac{l^2 ab}{d^2} + \frac{bd}{a^2} + \frac{l^2 a}{2d} + \frac{d}{2a} \right) \quad (1.20)$$

where  $\lambda = 2\pi/k$  is the wavelength and  $k$  the associated wave vector. For determination of the  $Q$ -factor, we additionally need the total energy stored in the cavity. The electromagnetic energy in this cavity volume  $V$  accounts to

$$W_{\text{em}} = \frac{1}{4} \int_V (\epsilon_0 \vec{E}^2 + \mu_0 \vec{H}^2) dr^3 = \frac{\epsilon_0 abd}{8} E_0^2. \quad (1.21)$$

Finally, we can express the expected contribution to  $Q_0$  of a rectangular cavity due to lossy walls as

$$Q_{\text{surf}} = \frac{2\omega W_{\text{em}}}{P_{\text{surf}}} = \frac{(kad)^3 b}{2\pi R_{\text{surf}}} \sqrt{\frac{\mu_0}{\epsilon_0}} \frac{1}{(2l^2 a^3 b + 2bd^3 + l^2 a^3 d + ad^3)}. \quad (1.22)$$

Cavity modes with higher  $l$  display an increase in surface loss, hence, a lower overall  $Q$ -factor. This can be explained by having a look at  $H_t$  for higher modes. The more antinodes of a mode are cramped into the cavity volume, the higher is the field in the direct vicinity of the surface (cf. Fig. 1.5). For a cavity with quadratic footprint ( $a = d$ ) and a realistic ratio of  $b/a = 1/5$ , we expect  $Q_{\text{surf}}$  to scale with  $1 : 0.4 : 0.2$  for TE101 : TE201 : TE301.

Moreover, the relation  $Q_{\text{surf}} \propto 1/R_{\text{surf}}$  from Eq. (1.22) can be understood intuitively.

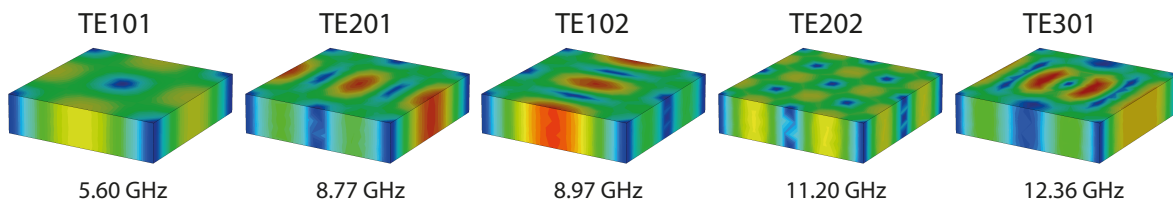


**Figure 1.5:** Simulated surface currents for the first five cavity modes sorted according to their mode frequency. The displayed range is normalized to the maximum surface current value of the TE301 case. The simulation results are obtained from the eigenmode solver (cf. Sec. C.1 in the appendix). Graphics are taken from CST Microwave Studio [50].

For a superconducting cavity casing, the surface resistance is very low, leading to high internal  $Q$ -factors. The remaining resistance stems from quasiparticles [59, 60], material impurities [61] and the finite  $H$ -field penetration depth of the superconductor, which is also geometrically linked to the surface roughness. In addition, a non-conducting or poorly conducting slit in the cavity acts as an obstacle to the surface current, hence, leading to a higher surface resistance.

### Dielectric losses

Another source for dissipation is the insertion of a dielectric. Usually, the qubit is inserted into the cavity as a separate chip. Therefore, we need to discuss the effects of such a lossy medium placed in the cavity. For reasons of simplicity, we discuss the case of a cavity, which is completely filled with a lossy dielectric with a loss tangent  $\tan(\delta)$  and a relative permittivity  $\epsilon_r$ . In this way, we obtain a lower bound for the quality factor, since, in experiment, the chip only partially occupies the cavity volume. The resulting  $Q$ -factor reads<sup>5</sup>

$$Q_{\text{diel}} = \frac{s'}{\tan(\delta)}. \quad (1.23)$$

We introduce a susceptibility factor  $s' \geq 1$  as a proportionality constant, which takes into account the volume participation ratio and the field at the chip position. Higher values of  $s'$  stand for the mode's resilience to be disturbed by the dielectric, whereas  $s' = 1$  means that the whole mode volume is filled with the dielectric.

In addition, the cavity resonance frequency will also change due to this perturbation. To this end, we define the change in the permittivity as  $\Delta\epsilon = (\epsilon_r - 1)\epsilon_0$  and neglect changes in the permeability  $\Delta\mu = 0$ , since in experiment, the materials are all non-magnetic. If we assume that the dielectric perturbation is small, we can approximate the perturbed fields with the original mode fields  $\vec{E}$  and  $\vec{H}$  and express the change in

<sup>5</sup>A detailed derivation can be found in Ref. [52].

resonant frequency as

$$\frac{\nu_0 - \nu}{\nu_0} \approx \frac{\int_V (\Delta\epsilon \vec{E}^2 + \Delta\mu \vec{H}^2) dr^3}{\int_V (\epsilon_0 \vec{E}^2 + \mu_0 \vec{H}^2) dx^3} = \frac{2 \int_V \Delta\epsilon \vec{E}^2 dr^3}{\epsilon_0 abd E_0^2}. \quad (1.24)$$

For the last step, we insert the result from Eq. (1.21) for the denominator. A change in the dielectric properties of the cavity ( $\Delta\epsilon > 0$ ) can be treated as an increase of the energy stored in the cavity as compared to the unperturbed case. Furthermore, the resonant frequencies of the cavity modes will decrease depending on the field distribution and the positioning of the dielectric material.

In the following, we estimate the frequency change for the TE<sub>101</sub> mode, if a small Si chip ( $\epsilon_r \simeq 11.7$ ) is inserted at the center  $\vec{r} = (a/2, b/2, d/2)$  of the cavity. We need to solve the integral  $\int_V \Delta\epsilon \vec{E}^2 dr^3$  for  $\vec{E} = E_0 \sin(\pi x/a) \sin(\pi z/d) \vec{e}_y$  and the dimensions of the chip  $V_{\text{chip}} = a_c b_c d_c$ . Since the dielectric perturbation  $\Delta\epsilon$  is finite for  $V_{\text{chip}}$  and zero elsewhere, we can write

$$\begin{aligned} \int_V \Delta\epsilon \vec{E}^2 dr^3 &= \int_{a/2-a_c/2}^{a/2+a_c/2} \int_{b/2-b_c/2}^{b/2+b_c/2} \int_{d/2-d_c/2}^{d/2+d_c/2} \Delta\epsilon E_0^2 \sin\left(\frac{\pi x}{a}\right)^2 \sin\left(\frac{\pi z}{d}\right)^2 dx dy dz \\ &= \Delta\epsilon E_0^2 b_c \left[ \frac{a_c}{2} + \frac{a}{2\pi} \sin\left(\frac{\pi a_c}{a}\right) \right] \left[ \frac{d_c}{2} + \frac{d}{2\pi} \sin\left(\frac{\pi d_c}{d}\right) \right] \\ &\approx \Delta\epsilon E_0^2 b_c a_c d_c = \Delta\epsilon E_0^2 V_{\text{chip}}. \end{aligned} \quad (1.25)$$

The approximation to linearize the sine in the second to last step is based on  $a_c, d_c \ll a, d$ . If we insert this expression into Eq. (1.24), we obtain

$$\frac{\nu_0 - \nu}{\nu_0} \approx \frac{2\Delta\epsilon E_0^2 V_{\text{chip}}}{\epsilon_0 E_0^2 V} = 2(\epsilon_r - 1) \frac{V_{\text{chip}}}{V}. \quad (1.26)$$

This equation states that, in the case of the TE<sub>101</sub> mode, a small piece of dielectric at the center of the cavity experiences a constant electric field  $E_0$ . If we insert typical chip and cavity dimensions, we can estimate the fractional frequency downshift to 4%. We note, that this approximation is only valid for small chips compared to the size of the cavity. Another way to determine the frequency shift taking into account the electric field distribution and the chip position is to use an FEM simulation tool.

To sum up, the internal  $Q$ -factor is mainly determined by surface losses ( $Q_{\text{surf}}$ ) and the insertion of lossy dielectric media into the cavity ( $Q_{\text{diel}}$ ).

$$Q_0 = \left( \frac{1}{Q_{\text{surf}}} + \frac{1}{Q_{\text{diel}}} \right)^{-1} \quad (1.27)$$

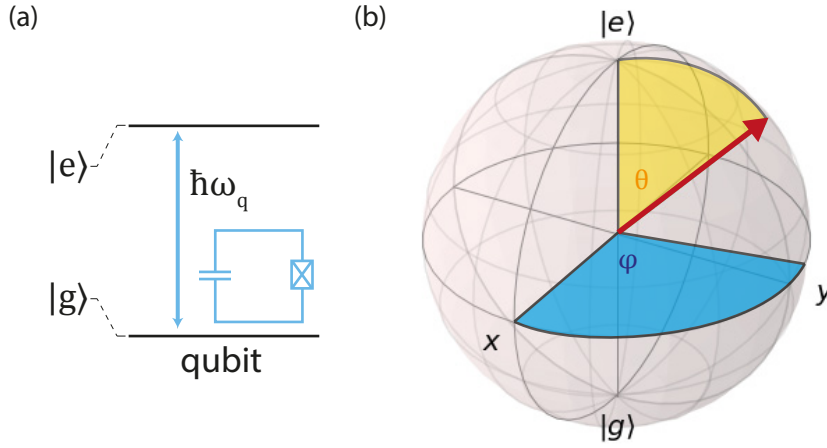


**Figure 1.6:** (a) Energy level scheme of a qubit. The qubit has a transition frequency between ground state  $|g\rangle$  and excited state  $|e\rangle$  of  $\omega_q/2\pi$  in the gigahertz regime for superconducting qubits. Inset: Circuit diagram of a superconducting qubit consisting of a capacitor and a Josephson junction. (b) Bloch sphere representation of an arbitrary pure qubit state.

## 1.2 The superconducting transmon qubit

Historically, the transmon (transmission line shunted plasma oscillation) qubit has evolved from the Cooper pair box (CPB) [62]. To date, the transmon circuit is the most successful qubit architecture [63–66] and has been used to built circuits containing up to 50 qubits [19] and 72 qubits [67]. We begin this section with the general description of a qubit, before we explain the Josephson physics necessary for the transmon circuit.

### 1.2.1 Quantum bits

A qubit can be viewed as an artificial atom in terms of its energy level scheme [cf. Fig. 1.6 (a)]. Commonly, the qubit is approximated as a two-level system with a ground state  $|g\rangle$ , excited state  $|e\rangle$  and a level separation of  $\hbar\omega_q$  in between. Such a two-level system is naturally found in trapped ions [68, 69], cold atoms [70] or NV centers [46, 47], but can also be built artificially. Semiconductor quantum dots [71] or topologically protected Majorana qubits [72] are just two examples. Our chosen approach is to harness superconducting circuits for this task.

Mathematically, the qubit state is expressed as  $|\Psi\rangle = \tilde{p}_g|g\rangle + \tilde{p}_e|e\rangle$  with  $p_g = |\tilde{p}_g|^2$  ( $p_e = |\tilde{p}_e|^2$ ) being the population of the ground (excited) state. They obey the normalization condition  $|\tilde{p}_g|^2 + |\tilde{p}_e|^2 = 1$ . Hence, the qubit state can be represented graphically as a point on a unit sphere centered at the origin of a Cartesian coordinate system, the

Bloch sphere [cf. Fig. 1.6 (b)]. In spherical coordinates, the state then reads<sup>6</sup> [73]

$$|\Psi\rangle = \cos\left(\frac{\theta}{2}\right)|g\rangle + e^{i\varphi}\sin\left(\frac{\theta}{2}\right)|e\rangle = \begin{pmatrix} e^{i\varphi}\sin(\theta/2) \\ \cos(\theta/2) \end{pmatrix} \quad (1.28)$$

for  $0 \leq \theta \leq \pi$  and  $0 \leq \varphi < 2\pi$ . All states on the surface of the sphere correspond to pure quantum states, whereas points inside the sphere are mixed states, where energy relaxation and/or dephasing into the environment has taken place. These effects are discussed in Sec. 1.4.2. Rotations of the state about the Cartesian  $x, y, z$  axes by an angle of  $\pi$  are accomplished using the Pauli matrices

$$\hat{\sigma}_x \equiv \begin{pmatrix} 0 & 1 \\ 1 & 0 \end{pmatrix} \quad \hat{\sigma}_y \equiv \begin{pmatrix} 0 & -i \\ i & 0 \end{pmatrix} \quad \hat{\sigma}_z \equiv \begin{pmatrix} 1 & 0 \\ 0 & -1 \end{pmatrix}. \quad (1.29)$$

The expectation value of the Pauli matrices,  $\langle \hat{\sigma}_x \rangle$ ,  $\langle \hat{\sigma}_y \rangle$  and  $\langle \hat{\sigma}_z \rangle$ , are measurement observables and fully describe the quantum state of the qubit. Typically, the  $z$ -axis is chosen as the energy quantization axis and, then, the Hamiltonian for our qubit reads

$$\mathcal{H}_{\text{qubit}} = \frac{\hbar}{2}\omega_q\hat{\sigma}_z. \quad (1.30)$$

A more complete way to express the qubit state is accomplished by the density matrix [73]

$$\hat{\rho} \equiv \frac{1}{2}(\mathbb{1} + \vec{\sigma} \cdot \vec{a}) \quad (1.31)$$

$$= \frac{1}{2} \begin{pmatrix} 1 + \cos(\theta) & \sin(\theta)\cos(\varphi) - i\sin(\theta)\sin(\varphi) \\ \sin(\theta)\cos(\varphi) + i\sin(\theta)\sin(\varphi) & 1 - \cos(\theta) \end{pmatrix} \quad (1.32)$$

which includes the description of mixed states. Here,  $\vec{a} \equiv (\sin\theta\cos\varphi, \sin\theta\sin\varphi, \cos\theta)$  is the Bloch vector and  $\vec{\sigma} \equiv (\hat{\sigma}_x, \hat{\sigma}_y, \hat{\sigma}_z)$  a vector of the Pauli matrices. In the case of a single qubit,  $\hat{\rho}$  is a  $2 \times 2$  matrix. To be physically valid, it is normalized to  $\text{Tr}\rho = 1$  and positive ( $\rho \geq 0$ ). If we limit our discussion to pure qubit states ( $\text{Tr}\rho^2 = 1$ ), we can express the density matrix using Eq. (1.28) as  $\hat{\rho} = |\Psi\rangle\langle\Psi|$ .

## 1.2.2 The Josephson junction

In terms of circuit QED, a superconducting qubit can be thought of as an anharmonic oscillator. In order to introduce such an anharmonicity into an otherwise linear harmonic  $LC$ -circuit, we have to consider a non-linear circuit element. Typically, such a nonlinearity is engineered as a Josephson junction. It consists of two superconducting

---

<sup>6</sup>We use the physically intuitive convention of  $|g\rangle \equiv \begin{pmatrix} 0 \\ 1 \end{pmatrix} = (0, 1)$  and  $|e\rangle \equiv \begin{pmatrix} 1 \\ 0 \end{pmatrix} = (1, 0)$ , which is in contrast to the convention used in information theory.

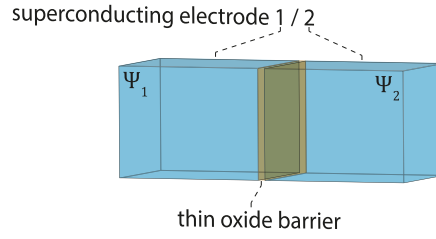


**Figure 1.7:** Schematic drawing of a Josephson junction consisting of two superconductors with wavefunctions  $\Psi_1$  and  $\Psi_2$  separated by a thin oxide barrier.

electrodes weakly coupled by, for example, a thin insulating layer as drawn in Fig. 1.7. This structure is described by the two Josephson equations [74]

$$I_s = I_c \sin(\varphi) \quad (1.33)$$

$$\frac{d\varphi}{dt} = \frac{2\pi}{\Phi_0} V. \quad (1.34)$$

In general, a superconducting state is described by a macroscopic wavefunction  $\Psi_{1,2} = \Psi_0 \exp(i\theta_{1,2})$ , with  $\Psi_0$  being the amplitude and  $\theta_{1,2}$  the phase. Here, the wavefunctions  $\Psi_1$  and  $\Psi_2$  refer to the superconducting electrode 1 and 2. The first Josephson equation relates the supercurrent  $I_s$  and the phase difference  $\varphi \equiv \theta_2 - \theta_1$ . This phase difference  $\varphi$  occurs between the two superconducting electrodes due to the thin barrier of the Josephson junction, leading to a sinusoidally modulated supercurrent  $I_s$  with amplitude  $I_c$ , which is the critical current of the superconductor. Below this critical value, the Josephson junction remains superconducting. The second Josephson equation, the voltage-phase relation, shows that the time derivative of the phase drop  $\varphi$  across the junction is proportional to the externally applied voltage  $V$ . In this context,  $\Phi_0 = h/2e$  is the magnetic flux quantum. The non-linear character of the junction becomes evident by taking the time derivative of the first Josephson equation and inserting the voltage-phase relation. Then, we obtain a relation between  $V$  and  $dI/dt$ . The proportionality constant,

$$L_J = \frac{\Phi_0}{2\pi I_c \cos(\varphi)}, \quad (1.35)$$

can be interpreted in circuit language as a non-linear inductance, because it depends on  $1/\cos(\varphi)$ . Similar to an inductance, where magnetic energy can be stored, the Josephson junction is characterized by a Josephson energy  $E_J = \Phi_0 I_c / (2\pi) [1 - \cos(\varphi)]$ , which describes energy storage in the kinetic energy of accelerated electrons [53]. In addition to its inductive behavior, due to the parallel interface of the two superconducting electrodes, the Josephson junction acts as a parallel plate capacitor with capacitance  $C_J$ .

The corresponding characteristic energy scale is the charging energy

$$E_C = \frac{e^2}{2C_J}. \quad (1.36)$$

$E_J$  and  $E_C$  determine the properties of a Josephson junction. As a result,  $C_J$  and  $I_c$  have to be well-controlled in fabrication.

So far, the Josephson junction has been treated using classical equations of motion. When investigating quantum circuits based on Josephson junctions, as they are necessary for quantum information processing, the semi-classical description of a Josephson junction has to be replaced by a fully quantized model. In the course of this quantization, the classical variable for magnetic flux,  $\Phi = (\Phi_0/2\pi) \varphi$ , and its conjugate, the electric charge,  $Q$ , are promoted to operators, which fulfill the commutation relation  $[\hat{Q}, \hat{\Phi}] = -i\hbar$ . With this quantized model at hand, we introduce the transmon circuit in the next section.

### 1.2.3 The transmon circuit

The transmon circuit consists of a Josephson junction<sup>7</sup> acting as a non-linear inductance (cf. Sec. 1.2.2), which is shunted with a large capacitance  $C_S$  [cf. Fig. 1.8 (a)]. Therefore, it can also be treated as an  $LC$ -circuit with a non-linear inductance. The total capacitance amounts to  $C_\Sigma = C_G(C_S+C_J)/(C_G+C_S+C_J)$  with  $C_G$  being the capacitance to ground. Often, the capacitance  $C_J \simeq 5$  fF (for a typical transmon qubit Josephson junction) is small compared to the other capacitances in the circuit and, hence, can be neglected. In contrast to the CPB, the transmon qubit is operated in the flux regime ( $E_J/E_C \gg 1$ ) and exhibits a significantly increased protection against charge noise due to the flat charge dispersion. However, the improved quantum coherence of the transmon qubit comes at the expense of a strongly decreased anharmonicity, making it not a strict two level system anymore. We now give a short explanation for this behavior. For a transmon circuit, the charging energy  $E_C$  is much smaller than the Josephson energy  $E_J$ . Therefore, we need to treat the system quantum mechanically. The effective Hamiltonian

$$\mathcal{H}_{\text{transmon}} = 4E_C(\hat{N} - N_g)^2 - E_J \cos(\hat{\varphi}) \quad (1.37)$$

contains the number of Cooper pairs  $\hat{N}$  and the Josephson junction phase difference  $\hat{\varphi}$  as quantized operators, which obey the quantum commutation relation  $[\hat{N}, \hat{\varphi}] = 2ie$ .

<sup>7</sup>Tunable transmon qubits are fabricated with two Josephson junctions, which are set in parallel acting as a SQUID. The flux threading the SQUID loop can be used to tune the inductance and, hence, the qubit frequency. Since in our case, the transmon qubit is placed in a superconducting cavity, which shields the qubit from external flux, we use fixed-frequency transmon qubits with a single Josephson junction. By adding normal conducting parts to the superconducting cavity, sufficient magnetic flux can pass through and be used for tuning a qubit [31, 75].

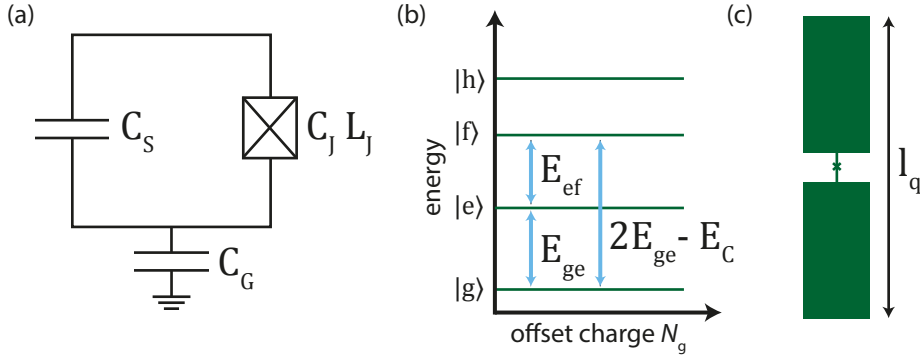


**Figure 1.8:** (a)  $LC$ -circuit representation of a transmon qubit with shunting capacitance  $C_S$  and capacitance to ground  $C_G$ . The circuit comprises a Josephson junction with capacitance  $C_J$  and non-linear inductance  $L_J$ . (b) Energy level scheme of transmon qubit with a flat dispersion relation. (c) Sketch of 3D transmon qubit with dipole length  $l_q$ . The two rectangular "paddles" serve as the shunt capacitance  $C_S$ . The Josephson junction is depicted as an "x" and is positioned on the bridge between the two capacitances.

$N_g$  is the offset charge. By solving this Hamiltonian, one obtains the eigenenergies [64]

$$E_m = -E_J + \sqrt{8E_C E_J} \left(m + \frac{1}{2}\right) - \frac{E_C}{12} (6m^2 + 6m + 3) \quad (1.38)$$

with  $m = 0, 1, 2, \dots$ . Here, the eigenenergies  $E_m$  are approximated by perturbation theory for  $E_J/E_C \gg 1$ . In this limit, they become independent of the offset charge  $N_g$  [64]. In the transmon qubit regime ( $E_J/E_C \simeq 50$ ), the first and second transition energies can be calculated as

$$E_{ge} = E_1 - E_0 \approx \sqrt{8E_C E_J} - E_C \quad (1.39)$$

$$E_{ef} = E_2 - E_1 \approx \sqrt{8E_C E_J} - 2E_C. \quad (1.40)$$

As a result, the difference between  $E_{ge}$  and  $E_{ef}$  is determined by the charging energy  $E_C$ . We specify this detuning as the transmon anharmonicity  $\alpha$ .

$$\alpha \equiv E_{ef} - E_{ge} \approx -E_C \quad \alpha_r = \frac{\alpha}{E_{ge}} \approx -\frac{1}{\sqrt{8E_J/E_C}} \quad (1.41)$$

This anharmonicity distinguishes a transmon qubit from an harmonic oscillator. We note that the term  $\sqrt{8E_C E_J}$  in Eq. (1.39) can be identified with the plasma energy  $\hbar\omega_p$  derived from the harmonic approximation of the transmon qubit potential. In the special case of the transmon circuit, the higher energy levels ( $|f\rangle$ ,  $|h\rangle$ , ...) are of practical importance [76]. Therefore, instead of using the strict two level qubit Hamiltonian expression in Eq. (1.30), it is sometimes more convenient to treat the transmon circuit as an anharmonic Duffing oscillator approximating the transmon circuit. We introduce

the ladder operators  $\hat{\sigma}^+$  and  $\hat{\sigma}^-$  [36, 64], where, similar to an harmonic oscillator,  $\hat{\sigma}^+$  ( $\hat{\sigma}^-$ ) raises (lowers) the number of excitations  $\hat{n}_q = \hat{\sigma}^+ \hat{\sigma}^-$  of the transmon qubit. Based on these, we can express the transmon qubit Hamiltonian as

$$\mathcal{H}_{\text{qubit}} = \hbar\omega_q \hat{\sigma}^+ \hat{\sigma}^- + \frac{\alpha}{2} \hat{\sigma}^+ \hat{\sigma}^- (\hat{\sigma}^+ \hat{\sigma}^- - 1). \quad (1.42)$$

where the first term is similar to the harmonic oscillator Hamiltonian and the second term takes into account the anharmonic level spacing of the higher levels.

The geometry of the transmon circuit [cf. Fig. 1.8 (c)] with its relatively long shunt capacitors offers an elegant way for coupling the transmon qubit to the cavity. The paddles serve as an electric dipole antenna of length  $l_q$ . As a consequence, the transmon qubit couples in first order to an applied electric field parallel to  $\vec{l}_q$ . In general, the characteristic coupling strength per photon is

$$g = \frac{\vec{\mu} \cdot \vec{E}_{\text{rms}}}{\hbar} \quad (1.43)$$

where  $\vec{\mu} = -2el_q \vec{e}_y$  is the dipole moment with  $-2e$  being the charge of one Cooper pair displaced from capacitor plate to the other and  $\vec{E}_{\text{rms}}$  the root mean square of the vacuum electric field, which is given by

$$\vec{E}_{\text{rms}} = \sqrt{\hbar\omega_c/2\epsilon_0 V_{\text{mode}}} \vec{e}_y \quad (1.44)$$

for a cavity with a mode volume  $V_{\text{mode}}$  [77]. However, we need to consider the field distribution of the mode inside the cavity and relate it to the qubit position. This leads us to define an effective mode volume as [78]

$$V_{\text{mode}} = \frac{\int_V \epsilon(\vec{r}) \vec{E}(\vec{r})^2 d\vec{r}^3}{\epsilon(\vec{r}_q) \vec{E}(\vec{r}_q)^2}. \quad (1.45)$$

For a rectangular cavity with the qubit placed in the center ( $\vec{r}_q = 0$ ), we obtain for the fundamental mode  $V_{\text{mode}} = 1/4 V$  and

$$g = -el_q \sqrt{\frac{2\omega_c}{\hbar\epsilon_0 V}} \quad (1.46)$$

where  $V$  is the volume of the cavity. We see that the coupling scales linearly with the length of the qubit. For this reason, designing 3D transmon qubits is straightforward. For typical transmon qubit and cavity geometries<sup>8</sup>, we obtain  $g/2\pi \simeq 57$  MHz. Moreover, the coupling can be enhanced by increasing the mode resonant frequency, but leaving

<sup>8</sup>Typical parameters are  $l_q = 760 \mu\text{m}$ ,  $\omega_c/2\pi = 5.7$  GHz and  $V = (a-b)bd + \pi/4b^2d = 8.785 \text{ cm}^3$  for the cavity dimensions given in Fig. 2.1.

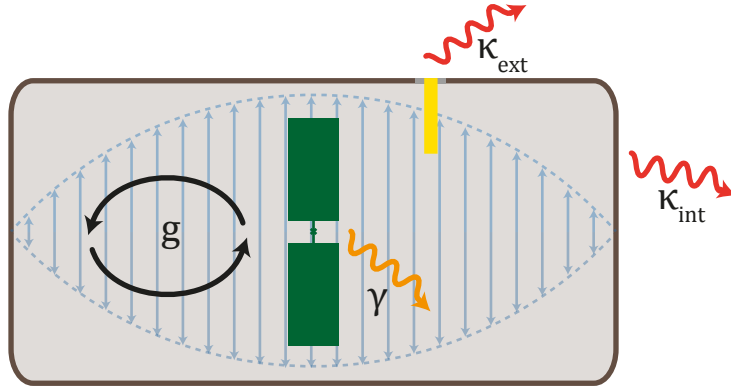


**Figure 1.9:** Scheme of transmon qubit (green) coupled to microwave 3D cavity (grey) in the absence of dephasing. The electric field distribution of the fundamental mode is shown in light blue. Photons can leak from the cavity through an antenna (yellow) with rate  $\kappa_{\text{ext}}$ . The energy relaxation is  $\gamma$  for the qubit and  $\kappa_{\text{int}}$  for the cavity. The coupling of qubit and cavity is described with the coupling strength  $g$ .

the mode volume unchanged. According to Eq. (1.5), cavities with a non-quadratic footprint ( $a \neq d$ ) can be used for this purpose.

### 1.3 Strong coupling of qubit and cavity

Due to their coupling, cavity and qubit can exchange energy quanta. In the absence of dephasing, the ratio between the coupling rate  $g$  and the qubit and cavity decay rates,  $\kappa$  and  $\gamma$ , determines the coupling regime. In the important case of strong coupling,

$$g \gg \kappa, \gamma \quad (1.47)$$

energy can be exchanged coherently before being lost to the environment (cf. Fig. 1.9). An additional requirement here is that  $g$  is small compared to the eigenfrequencies of qubit and cavity. This regime is of fundamental importance for quantum science and technology.

#### 1.3.1 Jaynes-Cummings Hamiltonian

In the case of  $g$  being much smaller than the eigenfrequencies of the system, the interaction of the qubit and the resonator field is well described by the Jaynes-Cummings Hamiltonian

$$\mathcal{H}_{\text{JC}} = \mathcal{H}_{\text{qubit}} + \mathcal{H}_{\text{cavity}} + \mathcal{H}_{\text{coupling}} \quad (1.48)$$

$$= \frac{1}{2}\omega_q \hat{\sigma}_z + \omega_c \left( \hat{a}^\dagger \hat{a} + \frac{1}{2} \right) + g \left( \hat{\sigma}^+ \hat{a} + \hat{\sigma}^- \hat{a}^\dagger \right). \quad (1.49)$$

Beside the terms for qubit and cavity, one finds the coupling Hamiltonian, which describes processes, where one excitation is created in the qubit and one is annihilated in the resonator and vice versa. The Jaynes-Cummings Hamiltonian can be diagonalized analytically [22] to obtain the eigenstates and eigenenergies. In the resonant case of  $\omega_q = \omega_c$ , this energy exchange between qubit and cavity can be observed as vacuum Rabi oscillations with a swap frequency of  $2g$  [22]. In this work, however, the qubit is typically far detuned ( $\Delta \gg g$ ) from the cavity and the energy exchange is prohibited. Therefore, additional coherent drives, which bridge the energy gap between qubit and cavity, have to be applied to the system.

### 1.3.2 Dispersive Hamiltonian

In the dispersive regime, the qubit and cavity frequency are detuned by an amount which is large compared to the coupling strength,

$$\Delta = \omega_q - \omega_c \gg g \quad (1.50)$$

Due to the large  $\Delta$ , the Jaynes-Cummings Hamiltonian can be rewritten to second order in  $g$  into the effective dispersive Hamiltonian [22]

$$\tilde{\mathcal{H}}_{\text{disp}} = \frac{1}{2}\omega_q\hat{\sigma}_z + (\omega_c + \chi\hat{\sigma}_z)\left(\hat{a}^\dagger\hat{a} + \frac{1}{2}\right) \quad (1.51)$$

$$\chi \equiv g^2/\Delta \quad (1.52)$$

with  $\chi$  being the dispersive coupling strength. This quantity describes the effective energy exchange in a system with a large detuning. The effective exchange rate becomes smaller by  $1/\Delta$  for a constant  $g$ . Often,  $\chi$  is also referred to as the dispersive shift, since the impact of the qubit onto the cavity results in a shifted cavity frequency

$$\tilde{\omega}_c = \omega_c + \chi\hat{\sigma}_z. \quad (1.53)$$

From this equation, we see the dependence of the dispersive shift on the qubit state encoded in  $\hat{\sigma}_z$ . In practice, this means that one can use the change in cavity frequency to detect the qubit state.

The dispersive shift in Eq. (1.52) is a general definition and refers to a perfect two-level system, i.e., a qubit, coupled dispersively to a resonator. However, for a transmon qubit with its non-negligible higher levels, the dispersive shift has to be refined to [64]

$$\chi' = \chi_{01} - \frac{\chi_{12}}{2} \quad (1.54)$$

with  $\chi_{ij} = g_{ij}/(\omega_{ij} - \omega_c)$ . The coupling to higher levels<sup>9</sup> scales as  $g_{k,k+1} \simeq \sqrt{k+1}g$ .

<sup>9</sup>The higher energy levels of the transmon circuit have a significantly stronger dispersion as compared

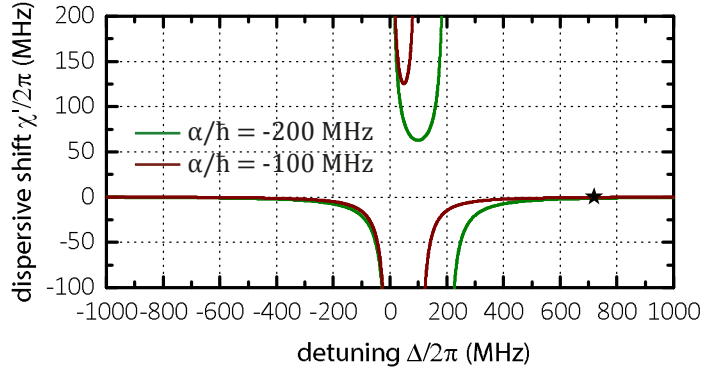


**Figure 1.10:** Dispersive shift  $\chi'$  depending on detuning according to Eq.(1.55) for  $E_J/E_C = 50$  and  $g = 50$  MHz. The star marks a typical detuning of 720 MHz, which results in  $\chi' \simeq -1$  MHz.

We can also express this reduced  $\chi'$  by using the anharmonicity  $\alpha$ .

$$\chi' \approx \frac{g^2}{\Delta} \frac{\alpha}{\hbar\Delta + \alpha} \quad (1.55)$$

Here again, the transmon qubit regime ( $E_J/E_C \gg 1$ ) has to be satisfied. With the correction factor, we meet the requirements, that the dispersive shift of a transmon qubit is significantly altered due to the interactions from higher energy levels as compared to a perfect two-level system. Since the focus of this work lies on transmon qubits, we will use  $\chi'$  instead of  $\chi$  for the dispersive shift. According to Eq.(1.55),  $\chi'$  can become negative depending on the sign and the value of the detuning  $\Delta$ . We plot the dispersive shift depending on the detuning in Fig. 1.10. For large absolute detunings ( $|\Delta| > |\alpha|$ ), the dispersive shift is negative, small and becomes almost independent of  $\Delta$ . If  $\Delta$  is in the range of  $-\alpha$ , we need to distinguish between positive and negative detunings. For  $\Delta < 0$ , the dispersive shift is negative. However, for  $0 < \Delta < |\alpha|$ , we enter the straddling regime [64], where  $\chi' > 0$  and is relatively large.

For future considerations to move to the strong dispersive regime ( $|\chi'| \gg \kappa, \gamma$ ) [64, 79, 80], where the photon number of the cavity is resolved as separate qubit peaks and the qubit state is resolved as separate cavity peaks, one has to ensure that the cavity and qubit decay rates are small and that  $\Delta$  may not be larger than approximately  $\alpha/2\hbar$ . By increasing the anharmonicity of the transmon qubit, higher detunings are also possible.

### Dispersive energy level scheme

For the coupled system, the equidistant energy level ladder of the harmonic cavity is shifted by the qubit energy, if the qubit is excited (cf. Fig. 1.11). Here, we assume

---

to the lowest two levels. As a result, due to the coupling to these higher levels, the sensitivity to charge fluctuations is increased.

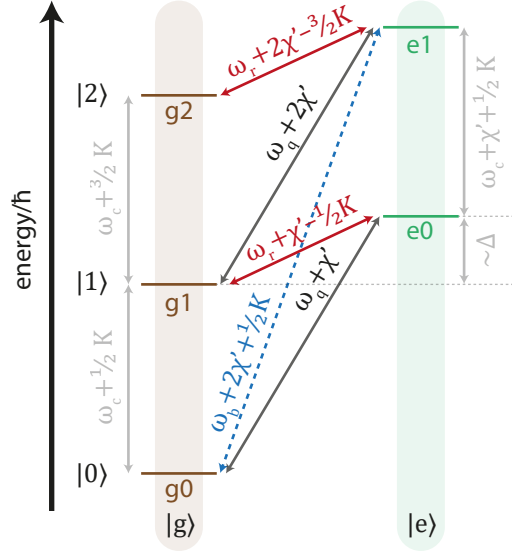


**Figure 1.11:** Energy level scheme of the dispersive ladder restricted to  $|g\rangle$  and  $|e\rangle$  up to the two photon Fock state. The first-order dispersive shift  $\chi'$  and the second-order Kerr non-linearity  $K$  are considered. The red arrow transitions conserve the number of excitations in the system and are covered by the Jaynes-Cummings Hamiltonian. Black arrows indicate the bare qubit transitions and leakage transitions to higher states. The blue dashed arrows are blue sideband transitions.

$\omega_q > \omega_c$ . Between these two ladders, sideband transitions are allowed as second-order processes [81, 82]. When taking the sum (difference) of qubit and cavity energy, the blue (red) sideband are defined as

$$\omega_b \equiv \tilde{\omega}_c + \tilde{\omega}_q \quad \omega_r \equiv |\tilde{\omega}_c - \tilde{\omega}_q| \quad (1.56)$$

where  $\tilde{\omega}_{c,q}$  are the shifted frequencies as discussed in the following.

### Multimode AC Stark shift

Common to quantum mechanics is the fact that the shift  $\chi'$  is a two-way effect. By rearranging Eq. (1.51), one finds a shift in the qubit frequency determined by the photon population in the cavity

$$\tilde{\omega}_q = \omega_q + n\chi' + \frac{1}{2}\chi'. \quad (1.57)$$

In literature, the second term is referred to as the AC Stark shift and the third term as the constant Lamb shift. We plot this linear relation in Fig. 1.12 (a). Equation (1.57) is valid, if the qubit is coupled solely to a single mode of the cavity. In practice, however, the qubit often couples to multiple cavity modes. In this situation, a multimode AC

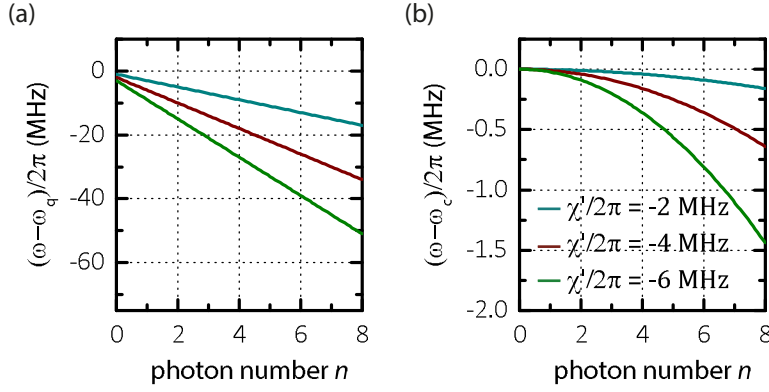


**Figure 1.12:** (a) AC Stark shift according to Eq. (1.57) and (b) Kerr effect according to Eq. (1.59) for different dispersive shifts and  $\alpha/h = -200$  MHz.

Stark shift occurs together with constant Lamb shifts, which is expressed as

$$\tilde{\omega}_q = \omega_q + \sum_i \chi'_i \left( n_i + \frac{1}{2} \right). \quad (1.58)$$

Here, the index  $i$  enumerates the different modes, which are present in the cavity.

### Kerr effect

Besides the AC Stark shift, which is linear in the photon number  $\hat{n}$ , there is also the self-Kerr effect, which scales with  $\hat{n}^2$ . It occurs, because the harmonic cavity partially inherits the anharmonicity of the qubit. We note as a side remark that, when treating the transmon qubit as an anharmonic oscillator as shown in Eq. (1.42), the intrinsic qubit anharmonicity  $\alpha$  is often referred to as the self-Kerr shift of the qubit and the dispersive shift between cavity and qubit as the cross-Kerr shift [83]. For the Kerr-shifted cavity frequency, we obtain

$$\tilde{\omega}_c = \omega_c + \frac{K}{2} \hat{a}^\dagger \hat{a}^\dagger \hat{a} \hat{a} \quad (1.59)$$

with  $K \simeq \chi^2/4\alpha$  [84]. This relation is plotted in Fig. 1.12 (b). Altogether, the full dispersive Hamiltonian for a single qubit coupled to  $i$  harmonic modes reads

$$\mathcal{H}_{\text{disp}}/\hbar = \frac{1}{2} \omega_q \hat{\sigma}_z + \sum_i \left[ (\omega_i + \chi'_i \hat{\sigma}_z) \left( \hat{a}_i^\dagger \hat{a}_i + \frac{1}{2} \right) + \frac{K_i}{2} \hat{a}_i^\dagger \hat{a}_i^\dagger \hat{a}_i \hat{a}_i \right] \quad (1.60)$$

with  $\omega_i$  being the frequency and  $K_i$  the self-Kerr shift of the  $i$ th mode.

## 1.4 Dynamics of a driven qubit-cavity system

Up to this point, we have treated the coupled qubit-cavity setup in a time-independent fashion. Now, we analyze the pure qubit dynamics and then move on to scenarios, where the cavity is also involved. For the first task, we take the qubit Hamiltonian from Eq. (1.30) and add a coherent drive tone with frequency  $\omega_d$ , amplitude  $\Omega_d$  and phase  $\varphi_d$ .

$$\mathcal{H}_{q,\text{drv}} = \mathcal{H}_q + \mathcal{H}_{\text{drv}} \quad (1.61)$$

$$= \frac{\hbar}{2}\omega_q\hat{\sigma}_z + \hbar\Omega_d \cos(\omega_d t + \varphi_d)\hat{\sigma}_x \quad (1.62)$$

If we now move to a frame rotating with the drive frequency and apply a rotating wave approximation (RWA), the Hamiltonian changes to

$$\mathcal{H}_{q,\text{drv}}^{\text{RWA}} = \frac{\hbar}{2}[\delta\hat{\sigma}_z + \Omega_0(\cos(\varphi_d)\hat{\sigma}_x + \sin(\varphi_d)\hat{\sigma}_y)] \quad (1.63)$$

with detuning  $\delta = \omega_q - \omega_d$  and the resonant Rabi oscillation frequency  $\Omega_0$ . In this frame, the qubit Bloch vector rotates about an axis defined by the phase  $\varphi_d$  and  $\delta$ . More quantitatively, near resonance one observes Rabi oscillations with frequency  $\Omega_R = \sqrt{\delta^2 + \Omega_0^2}$  [cf. Fig. 1.13 (a)]. In the resonant case,  $\delta = 0$ , the Rabi frequency assumes its minimum value  $\Omega_0$  [cf. Fig. 1.13 (b)]. From the Rabi frequency, we can define a time period, which is necessary to create a state flip from  $|g\rangle$  to  $|e\rangle$ . Since in this case, the qubit Bloch vector rotates by  $\pi$ , one finds the characteristic time  $T_\pi = 1/2\Omega_0$  [cf. Fig. 1.13 (c)]. Similarly, any polar rotation angle  $\theta$  can be achieved by choosing the proper rotation time  $T_\theta$ . In Fig. 1.13 (d), we plot a Rabi oscillation time trace for zero and finite detuning. For accurate state preparation, it is important to use correct drive amplitudes, lengths and frequencies.

### 1.4.1 Excitation of sideband transitions

In our experiments, the qubit drive is coupled in via the cavity. Since it is typically far off-resonant to the cavity eigenfrequencies, the cavity mode population remains low. However, it is possible to apply a drive at the sum frequency of qubit and cavity mode, which is the blue sideband as defined in Eq. (1.56). In this situation, two excitations, namely one photon in the cavity and one excitation in the qubit, are created (or annihilated) at once. Due to parity conservation (cf. Fig. 1.11), for the blue sideband transition,  $|g0\rangle \Leftrightarrow |e1\rangle$ , a two-photon drive is necessary. In the interaction picture, the

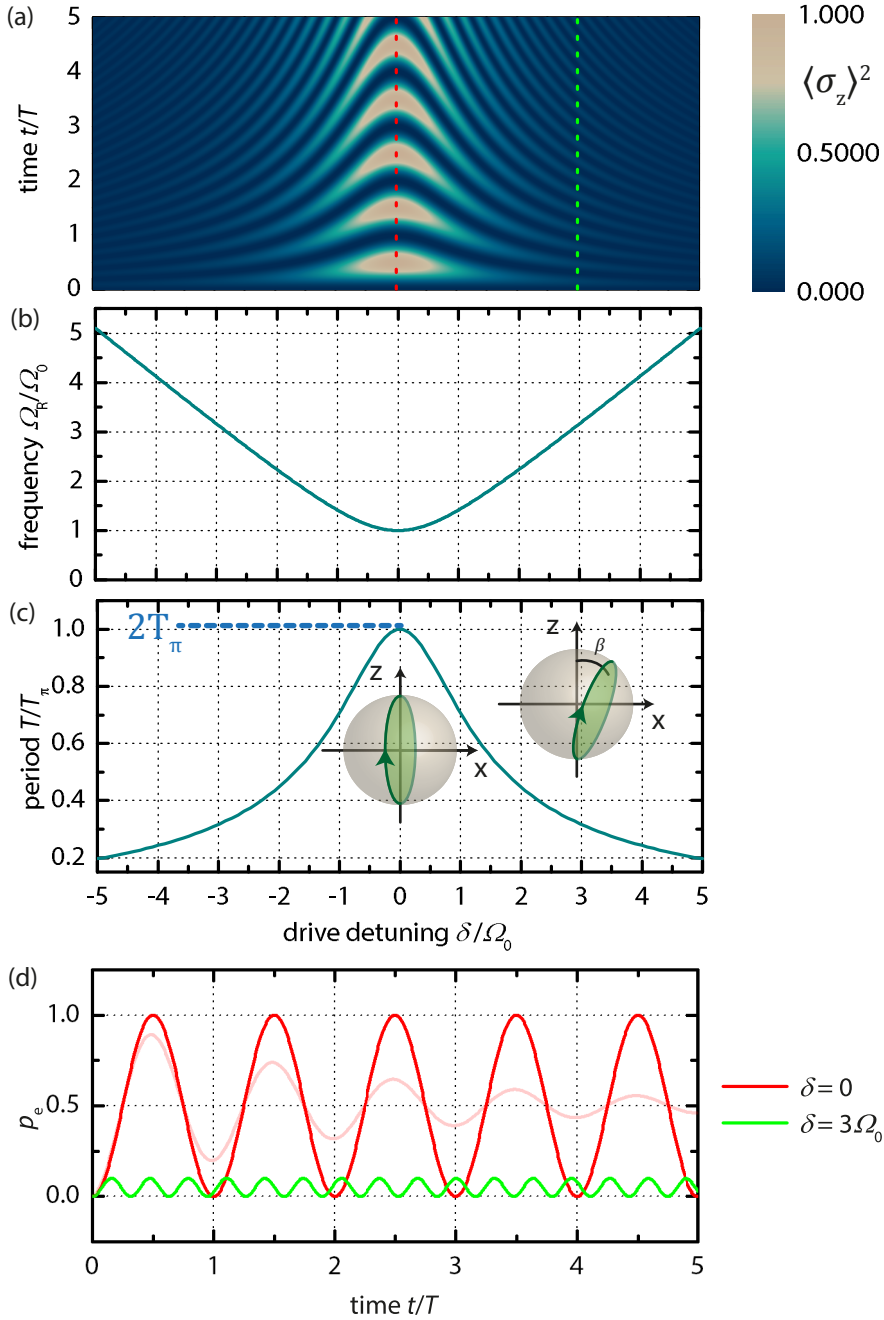


**Figure 1.13:** (a) Rabi oscillations, (b) Rabi frequency  $\Omega_R$  and (c) period  $T = 1/\Omega_0$  depending on the drive detuning. At  $\delta = 0$ , the qubit vector rotates about the  $x$ -axis (inset). Hence, the period is twice  $T_\pi$ . For finite detunings, the rotation plane is tilted by  $\beta = \arctan(\delta/(\Omega_0))$  regarding the  $z$ -axis. (d) Time traces of Rabi oscillations as marked by dotted lines in (a) for zero and finite detuning  $\delta$ . The contrast between excited and ground state is diminished by a factor of  $\Omega_0^2/(\delta^2 + \Omega_0^2)$ . The light red trace takes into account an exponential decay into a mixed state, as discussed in the next section.

Hamiltonian for the blue sideband (BSB) reads [81, 82]

$$\mathcal{H}_{\text{BSB}} = \hbar g \frac{g\Omega_d}{(\omega_m - \omega_b/2)^2} \frac{g\Omega_d}{(\omega_q - \omega_b/2)^2} (\hat{a}^\dagger \hat{\sigma}^+ + \hat{a} \hat{\sigma}^-) \quad (1.64)$$

$$= \frac{\hbar g}{4} \frac{\tilde{\Omega}_m \tilde{\Omega}_q}{\tilde{\Delta}_m \tilde{\Delta}_q} (\hat{a}^\dagger \hat{\sigma}^+ + \hat{a} \hat{\sigma}^-). \quad (1.65)$$

In this equation,  $\omega_m$  is the frequency of the involved mode. The effective drive  $\tilde{\Omega}_{m,q} = \Omega_d \cdot 2g/(\omega_{m,q} - \omega_b/2) = \Omega_d \cdot 2g/\tilde{\Delta}_{m,q}$  is reduced by the dispersive factor  $2g/\tilde{\Delta}_{m,q}$ , where  $\tilde{\Delta}_{m,q} = \omega_{m,q} - \omega_b/2$  is the detuning of the drive at  $\omega_b/2$  from the qubit or the mode, respectively. Due to the presence of the drive, the qubit frequency is dispersively shifted as

$$\tilde{\omega}_q = \omega_q + \frac{\tilde{\Omega}_m \tilde{\Omega}_q}{\tilde{\Delta}_m}. \quad (1.66)$$

Instead of using a single drive providing two photons with the same frequency, we can also combine two separate drives ( $\Omega_{d1}, \Omega_{d2}$ ) and add up the photons. Then, the shift is described as

$$\tilde{\omega}_q = \omega_q + \frac{1}{2} \frac{\tilde{\Omega}_{m1} \tilde{\Omega}_{q1}}{\tilde{\Delta}_{m1}} + \frac{1}{2} \frac{\tilde{\Omega}_{m2} \tilde{\Omega}_{q2}}{\tilde{\Delta}_{m2}}. \quad (1.67)$$

Again, we have introduced effective drives, which are governed by the detuning between the drive frequencies ( $\omega_{d1}, \omega_{d2}$ ) and qubit or mode, respectively.

$$\tilde{\Omega}_{n,i} = \Omega_{d,i} \cdot \frac{2g}{\omega_n - \omega_{di}} = \Omega_{d,i} \cdot \frac{2g}{\tilde{\Delta}_{n,i}} \quad (1.68)$$

with  $n = m, q$  for mode and qubit and  $i = 1, 2$ . This model can also be scaled to more than two drives.

## 1.4.2 Energy relaxation and dephasing

So far, we have discussed the behavior of ideal quantum systems. For a more realistic description, one has to take into account energy relaxation and dephasing. Energy relaxation is related to processes, where state population is lost from the excited to the ground state. Dephasing refers to the loss of phase coherence. In experiment, energy relaxation and dephasing occur simultaneously and the combination of both is specified as decoherence. When these effects become too strong, the observation of coherent quantum evolution is not possible in practice, because, mathematically speaking, an initially pure quantum state turns into a mixed state after a certain time. For time scales much longer than the energy relaxation or dephasing times, the system can be described classically.

We use the density matrix defined in Eq. (1.32), to describe our quantum state in the presence of decoherence. We start with a full Hamiltonian  $\mathcal{H}_{\text{full}}$  containing the actual

quantum system of interest and the environment responsible for decoherence. Then, the time evolution is given by the von Neumann equation

$$\frac{d\hat{\rho}_{\text{full}}}{dt} = -\frac{i}{\hbar}[\mathcal{H}_{\text{full}}(t), \hat{\rho}_{\text{full}}(t)]. \quad (1.69)$$

Here,  $\hat{\rho} = \hat{\rho} \otimes \hat{\rho}_{\text{E}}$  and  $\mathcal{H}_{\text{full}} = \mathcal{H} + \mathcal{H}_{\text{E}}$ , where quantities without index refer to the quantum system of interest and quantities with index E to the environment. When tracing out the environmental degrees of freedom under the Born-Markov approximation [85] (weakly coupled, large environment without memory), we obtain the well-known Lindblad master equation [86, 87]

$$\frac{d\hat{\rho}}{dt} = -\frac{i}{\hbar}[\mathcal{H}(t), \hat{\rho}(t)] + \sum_n \frac{1}{2} \left[ 2\hat{C}_n \hat{\rho}(t) \hat{C}_n^\dagger - \hat{\rho}(t) \hat{C}_n^\dagger \hat{C}_n - \hat{C}_n^\dagger \hat{C}_n \hat{\rho}(t) \right]. \quad (1.70)$$

In this equation,  $\hat{C}_n = \sqrt{\gamma_n} \hat{A}_n$  are the collapse operators, which describe the coupling to the environment with the operator  $\hat{A}_n$  and the rate  $\gamma_n$ . For a two-level system, an important result is that the decoherence time  $T_2 = 2\pi/\gamma_2$  is related to energy relaxation ( $T_1 = 2\pi/\gamma_1$ ) and pure dephasing ( $T_\varphi = 2\pi/\gamma_\varphi$ ) as

$$\frac{1}{T_2} = \frac{1}{2T_1} + \frac{1}{T_\varphi}. \quad (1.71)$$

The corresponding collapse operators are  $\sigma^-$  for energy relaxation and  $\sigma_z$  for dephasing. Next, we give two specific examples of decoherence, which occur in a coupled qubit cavity system.

### 1.4.3 Purcell effect

A qubit coupled to a cavity is subjected to a certain density of states provided by the cavity<sup>10</sup>. It differs significantly from that of an open system  $D_{3\text{D}}(\omega) = \omega^2/\pi^2 c^3$ . This new density of states  $D_{\text{cav}}(\omega)$  is distributed as a Lorentz function around the cavity resonance frequency.

$$D_{\text{cav}}(\omega) = \frac{1}{\pi} \frac{\kappa/4\pi}{(\omega - \omega_c)^2 + (\kappa/4\pi)^2} \quad (1.72)$$

According to Fermi's golden rule  $\Gamma = 2\pi g(\omega)^2 D(\omega)$ , this modified final density of states leads to a new relaxation channel for qubit. It is described by the Purcell decay rate in the limit of large detunings  $\Delta \gg \kappa$  as [89]

$$\kappa_{\text{P}} \simeq \kappa \left( \frac{g}{\Delta} \right)^2. \quad (1.73)$$

<sup>10</sup>One has to use the Bloch-Redfield master equation, which takes into account the microscopic environment [88].

The stronger a qubit is coupled to the cavity, the higher is the impact from the cavity decay. We see an enhanced decay for detunings smaller than the coupling strength. However, in the dispersive regime, this is usually not the case. To sum up, the Purcell rate gives a measure of how well a highly detuned qubit is protected by the reduced density of states imposed by the cavity. In the case of a multimode 3D cavity, a better description of the Purcell effect is via the cavity admittance  $Y(\omega)$  at the qubit transition frequency [90]

$$\kappa_{\text{P}}^{3\text{D}} = \frac{\text{Re}[Y(\omega_{\text{ge}})]}{2\pi C_{\Sigma}}. \quad (1.74)$$

The transmittance  $Y(\omega)$  and the transmon qubit capacitance  $C_{\Sigma}$  can be obtained by HF simulations of the cavity.

#### 1.4.4 Dephasing of a quasi-harmonic mode

A bare harmonic oscillator exhibits no dephasing because the energy level separation does not change as a function of applied fields. However, the situation changes when a qubit is inserted. We can explain this dephasing behavior by considering a stochastic qubit jump rate [42] between the qubit states  $|g\rangle$  and  $|e\rangle$ . For the dephasing rate, we obtain

$$\gamma_{\varphi} = \frac{\gamma}{2} \text{Re} \left[ \sqrt{\left(1 + \frac{2i\chi'}{\gamma}\right)^2 + \frac{8i\chi'p_e}{\gamma}} - 1 \right] \quad (1.75)$$

where  $\gamma$  is the qubit energy relaxation rate,  $\chi'$  is the dispersive shift of the transmon qubit and  $p_e$  the qubit excited state population. The population jumps result in frequency shifts of the mode frequency  $\omega_m$  due to the dispersive interaction and, as a consequence, the loss of phase information. We note that this dephasing relation also holds the other way round, meaning that photon shot noise in the resonator causes the qubit to dephase [91]. For this, one has to exchange the roles of qubit and resonator ( $\gamma \Rightarrow \kappa$ ,  $p_e \Rightarrow n_{\text{th}}$ , where  $n_{\text{th}}$  is the number of thermal photons in the cavity). In our case, however, the qubit-induced resonator dephasing dominates over resonator-induced qubit dephasing due to very high  $Q$  of the cavity. As a result, we expand Eq. (1.75) for  $\chi' \gg \gamma$  and obtain [41]

$$\gamma_{\varphi} \simeq p_e \gamma \left[ 1 - \mathcal{O}\left(\frac{\gamma}{\chi'}\right)^2 \right] \simeq p_e \gamma. \quad (1.76)$$

In other words, the qubit imposes a second-order Kerr non-linearity onto the cavity, making it slightly anharmonic and, therefore, susceptible to dephasing.



# Chapter 2

## Methods and techniques

For a quantum memory to work in practice, a lot of major and minor things have to be considered. In this chapter, we will reveal the details regarding fabrication and measurement of the quantum memory and its components. First, we discuss the fabrication of a high- $Q$  waveguide cavity from scratch. Next, we consider the qubit design with a focus on nano fabrication and the effect of thermal cycling of qubit samples. For characterization of the qubit, we briefly introduce the low-temperature setup and discuss essential types of measurements in the frequency domain. Coming to time resolved measurements, we accentuate the shaping of the pulses developed and used in the course of this work.

### 2.1 Fabrication

The realm of nano fabrication is very diverse. It reaches from self-assembled structuring [92] to sticky-taping graphene [93]. For nanoscale quantum systems, one specific approach is to use electron beam (e-beam) lithography. In the case of superconducting qubit fabrication, many methods are based on strategies developed in the semiconductor industry [94]. This provides optimized fabrication stability, however, prototyping qubits on a small scale still remains a demanding job.

#### 2.1.1 3D cavity design

In principle, a 3D cavity consists of a free space volume surrounded by metal walls. We choose a rectangular shaped cavity because of its easily accessible multimode structure. The height of the cavity is designed such that our standard qubit chips fit in. For the lateral dimension, one can use Eq. (1.5) to roughly estimate the size. However, a more accurate design can be achieved by using an FEM simulator [50] to optimize the length and width for the required eigenfrequencies. For this task, one can setup a transmission simulation and set the target frequency to be the one with maximum transmission in the optimizer. The optimization procedure uses the length and width of the cavity as free parameters in predefined ranges. The frequency of the fundamental mode is set

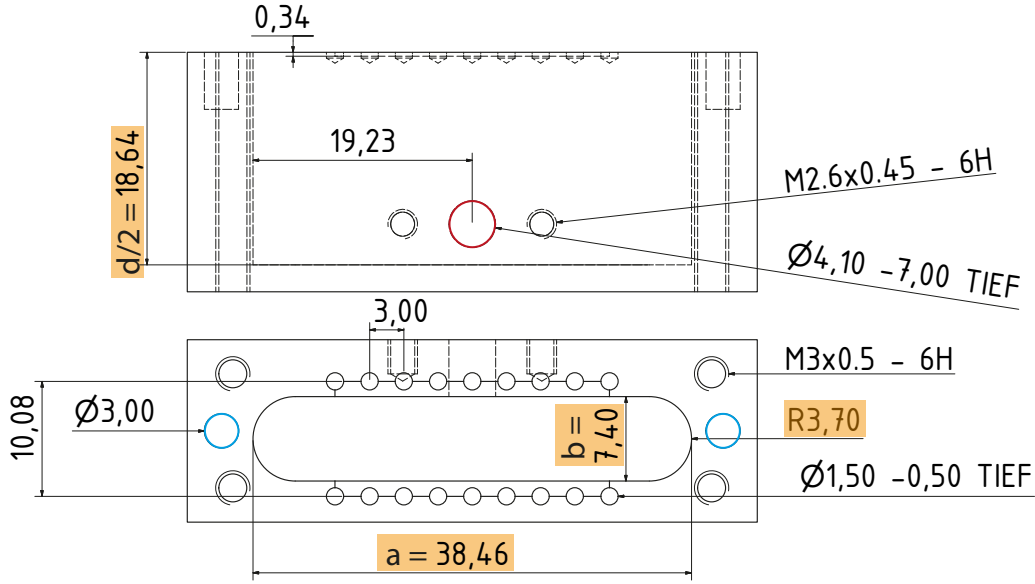


**Figure 2.1:** Technical drawing of one half of the 3D cavity. All dimensions are in mm. The other half has the same dimensions. The relevant parameters for the cavity volume,  $a$ ,  $b$  and  $d$ , are marked in orange color. With the holes (blue) at the side, the cavity is bolted for an accurate positioning of both halves. In the hole (red) at the top, the coupling antenna is inserted and screwed in place using the two threads nearby. For the qubit chip fixation, small dents with a distance of 3 mm are drilled.

to match the rest of the microwave setup, which is typically limited by the cryogenic HEMT amplifiers with a bandwidth of 4 to 8 GHz or a JPA amplifier [95, 96] with a very limited bandwidth of a few tens of MHz around 5.75 GHz. Due to machining constraints, the edges of the cavity are rounded, which has to be taken into account in the simulation. Analytically, we can express these semicircular profile of the edges by defining a new width depending on the height [97] as

$$a'(b) = \frac{1}{b} \left[ b \cdot (a - b) + \pi \left( \frac{b}{2} \right)^2 \right] = (a - b) + \frac{\pi b}{4}. \quad (2.1)$$

By doing so and using Eq. (1.5), we obtain a calculated resonance frequency of  $\nu_{101} = 5.64$  GHz for the cavity dimensions presented in Fig. 2.1. This resonance frequency is altered by the insertion of antenna pins, which is discussed in the next paragraph. Regarding the material, the internal quality factor below  $T_c$  does not significantly differ for casings made of 99.99% or 99.5% aluminum. However, aluminum alloy (EN AW-2007<sup>1</sup>) turns out to be disadvantageous for this task due to its lower intrinsic conductivity [78, 97].

<sup>1</sup>EN AW-2007 is a composition of 88% to 93% Al, 3.3% to 4.6% Cu,  $\leq 1.8\%$  Mn,  $\leq 1.5\%$  Pb, 0.8% Fe, Si, Zn, 0.2% Ni, Ti and 0.1% Cr

### Antenna geometry and external $Q$ -factor

The cavity is coupled to the environment via two antennas for transmission measurements. The position, length and diameter of these antennas determine the capacitive coupling strength. Moreover, as pointed out in Sec. 1.1.1, the coupling depends on the electric field  $E_{\parallel,\text{ant}}(x,y,z)$  at the antenna position. For a simplified cavity model (cf. Sec. C.1 in the appendix), we use CST Microwave Studio [50] to simulate  $E_{\parallel,\text{ant}}(x,y,z)$  of the TE101 mode for different radii of the cylindrical antenna aperture [cf. Fig. 2.2 (a)]. We evaluate  $E_{\parallel,\text{ant}}$  on a line along the  $y$ -direction through the center of the aperture. The origin,  $y = 0$ , is set at the transition from the aperture to the cavity. We find that  $E_{\parallel,\text{ant}}(y)$  inside the aperture and the cavity can be well approximated by the function

$$E_{\parallel,\text{ant}}(y) = \frac{E_0}{e^{y/r} + 1} \quad (2.2)$$

where  $E_0$  is the maximum electric field amplitude and  $r$  is a parameter related to the aperture radius and has the same units as  $y$ . Due to the limited height  $b$  of the cavity in the  $y$ -direction, which prevents the complete emergence of the electric field,  $E_0$  is only reached for small ratios of the aperture radius to the height  $b$ . If the aperture radius becomes large compared to  $b$ , then the electric field is not strictly bound to the cavity volume anymore, but can also emerge into the aperture leading to a smoother field distribution along the examined line. When simulating and fitting the electric field for a cavity with the same dimensions as used for later experiments (cf. Fig. 2.1), we obtain  $r = r_c = 0.92 \text{ mm}$  [cf. Fig. 2.2 (b)] for a real aperture radius of 2.05 mm. In Fig. 2.2 (c) we plot the fitted  $r$  for different aperture radii and find a linear relation between the real aperture radius and the fit parameter. This linear relation is valid up to a ratio of approximately  $r/b \simeq 1/5$ .

Based on the knowledge of  $E_{\parallel,\text{ant}}(y)$ , we are able to use Eq. (1.11) to calculate the external coupling rate

$$\kappa_x(l_{\text{ant}}) = \frac{C_x}{\hbar} \left( \int_{-\infty}^{l_{\text{ant}}} \frac{E_0}{e^{y/r} + 1} dy \right)^2 = \frac{C_x}{\hbar} \{E_0 r \ln[\exp(l_{\text{ant}}/r) + 1]\}^2. \quad (2.3)$$

Here, we assume  $r = r_c$  and  $E_0 = E_{\text{rms}}$  from Eq. (1.44)<sup>2</sup>. In the end, we choose  $C_x$ , such that typical coupling rates in the order of 10 MHz to 100 MHz are obtained. As plotted in Fig. 2.2 (d), we notice that when the antenna pin is pulled out of the cavity volume,  $\kappa_x$  drops very quickly to zero. Inside the cavity, the coupling rate increases approximately as  $\kappa_x \propto l_{\text{ant}}^2$ .

The experimentally accessible parameter, however, is not  $\kappa_x$ , but  $\kappa = \kappa_x + \kappa_0$  or  $Q_L$ . Therefore, we use Eq. (1.12) and Eq. (1.13) to express  $Q_L$  dependent on  $\kappa_x$ . With

<sup>2</sup>For a cavity with  $\omega_c/2\pi = 5.7 \text{ GHz}$  and  $V = (a-b)bd + \pi/4b^2d = 8.785 \text{ cm}^3$  for the dimensions given in Fig. 2.1, we get  $E_{\text{rms}} = \sqrt{2\hbar\omega_c/\epsilon_0 V} \simeq 312 \text{ } \mu\text{V m}^{-1}$

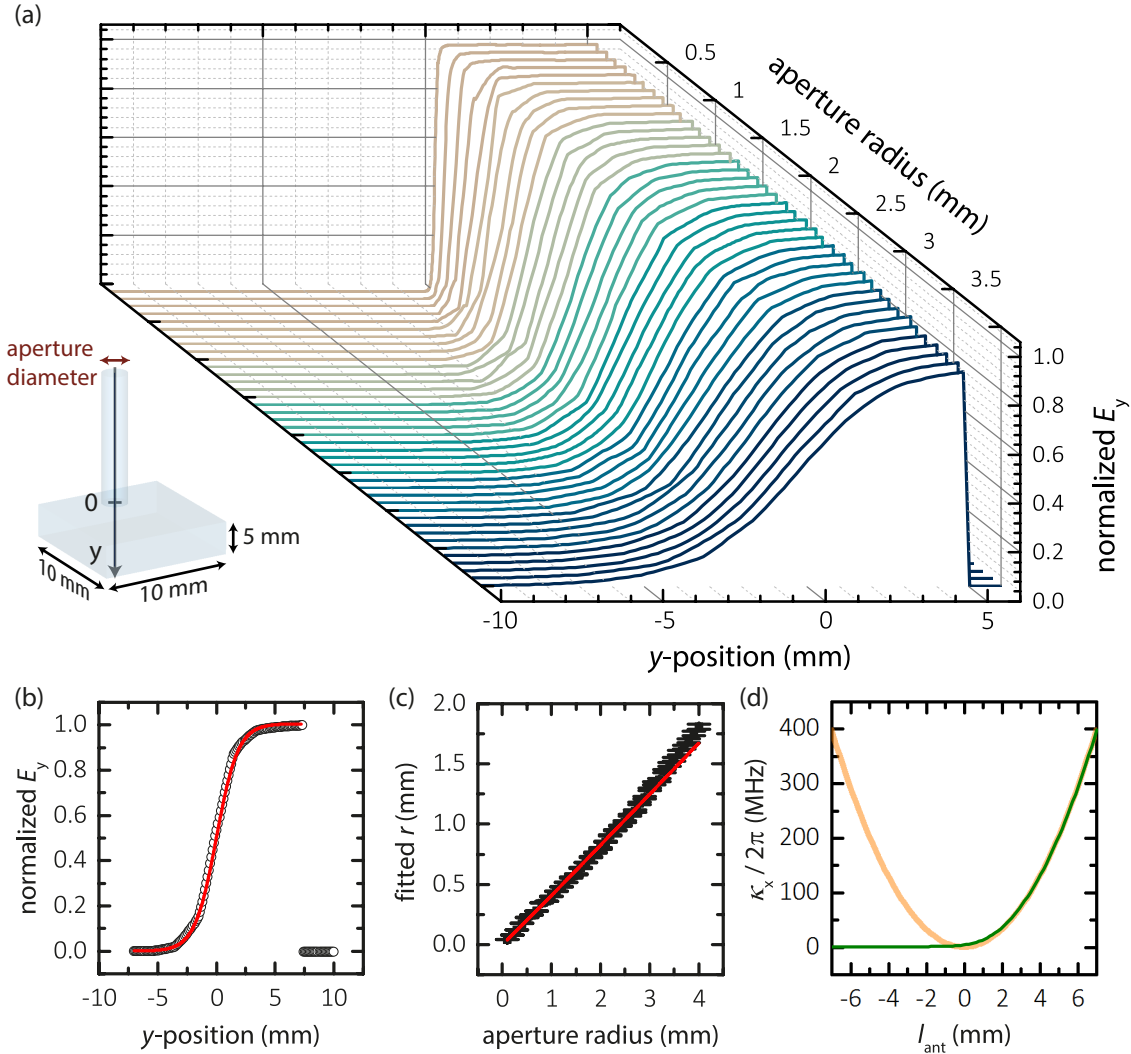


**Figure 2.2:** (a) Simulated  $E_y = E_{\parallel, \text{ant}}$  along a line centered at the antenna aperture and pointing in the  $y$ -direction (cf. inset) for different aperture radii. The wider the aperture becomes, the smoother is the transition from the cylindrical volume to the rectangular cavity volume. The field is normalized to the saturation value  $E_0$  (cf. simplified cavity model in Sec. C.1 in the appendix). (b) Simulated  $E_y$  along the same line as in (a) for real cavity dimensions given in Fig. 2.1. The red line is a fit based on Eq. (2.2). (c) Real aperture radius versus  $r$ , which is obtained from the fits in (a). The red line is a linear fit. (d) Calculated coupling rate  $\kappa_x$  as a function of the length of the antenna  $l_{\text{ant}}$  according to Eq. (2.3) (green line). The light orange parabola reveals the relation  $\kappa_x \propto l_{\text{ant}}^2$  for  $l_{\text{ant}} > 0$ .

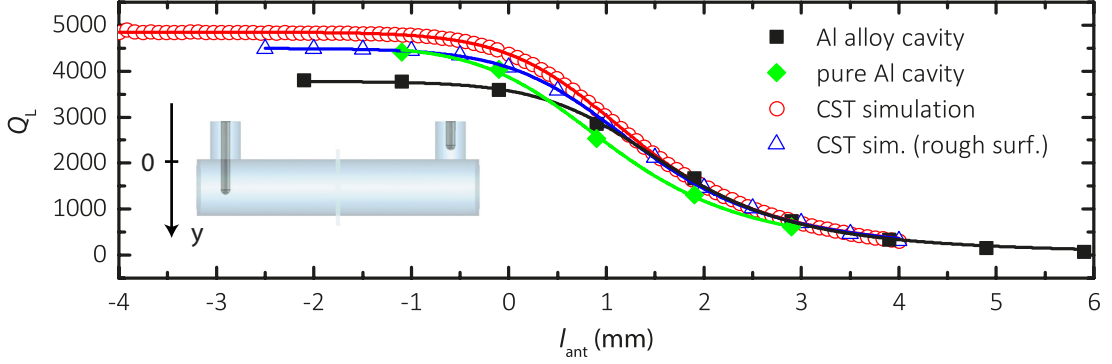


**Figure 2.3:** Simulation (open symbols) and measurement (filled symbols) of the TE101 loaded  $Q$ -factor depending on the antenna length for the pure Al cavity and the Al alloy cavity. The measurement is performed at room temperature. For the simulation to match the data, we need to introduce a surface roughness to lower the simulated internal  $Q$ -factor. At a retracted antenna position, the loaded  $Q$ -factor is approximately the internal  $Q$ -factor. Solid lines are fits using Eq. (2.4) and taking  $E_0 = 312 \mu\text{V m}^{-1}$ ,  $\omega_c/2\pi = 5.7 \text{ GHz}$  and  $r = 0.92$  as fixed parameters.

$Q_L = Q_0/(1 + \kappa_x/\kappa_0)$  we obtain the analytical expression

$$Q_L(l_{\text{ant}}) = \frac{Q_0}{1 + C_x \omega_c \{E_0 r \ln(\exp[(l_{\text{ant}} + l_0)/r] + 1)\}^2 / \hbar Q_0} \quad (2.4)$$

where  $l_0$  is inserted to account for an offset in the antenna length. In order to validate our theoretical model, we measure a cavity with different antenna pin penetration depths and use Eq. (2.4) as a fit function. In Fig. 2.3,  $Q_L$  of a bare cavity at room temperature is shown. In this scenario, the alloy cavity and the pure Al are used (cf. Tab. B.1 in the appendix). The antenna length is adjusted with spacers [78, 97]. When the antenna pin is retracted out of the cavity volume, the cavity is heavily undercoupled and the measured  $Q$ -factor is approximately  $Q_0$ . When comparing the alloy cavity with the pure Al cavity, we observe that already at room temperature the conductivity is significantly lower for the alloy cavity as displayed by the internal  $Q$ -factor<sup>3</sup>. The machined cavities have a certain surface roughness<sup>4</sup>, which has to be taken into account in the simulation to get a good agreement with the data.

Furthermore, we see an excellent agreement of the fits based on Eq. (2.4) with the  $Q_L$  data and the simulation results from CST Microwave Studio [50]. The capacitance  $C_x$ , which is used as a fit parameter, is on the order of 56 to 83 zF for all four fits, meaning that the theory is consistent for this cavity geometry regarding both simulated and

<sup>3</sup>At room temperature, bulk aluminum has a resistivity of  $\rho^{\text{Al}} = 2.65 \cdot 10^{-8} \Omega \text{ m}$  and aluminum alloy approximately  $\rho^{\text{alloy}} = 5.0 \pm 0.5 \cdot 10^{-8} \Omega \text{ m}$  [98, 99].

<sup>4</sup>At the curved sides of the machined and unpolished cavity, the average roughness is  $R_a = 1.280 \mu\text{m}$ , at the flat surfaces it is  $R_a = 0.3 \mu\text{m}$ . A definition of the average surface roughness can be found in Ref. [100].

	CST sim.	CST sim. (rough surf.)	Al alloy cavity	pure Al cavity
$C$ (zF)	60.2	60.6	83.2	55.7
$Q_0$	4850	4495	3777	4559
$x_0$ (mm)	-0.9	-0.9	-1.3	-0.5

**Table 2.1:** Fit parameters of the  $Q_L$ -fits. The fits are displayed in Fig. 2.3.

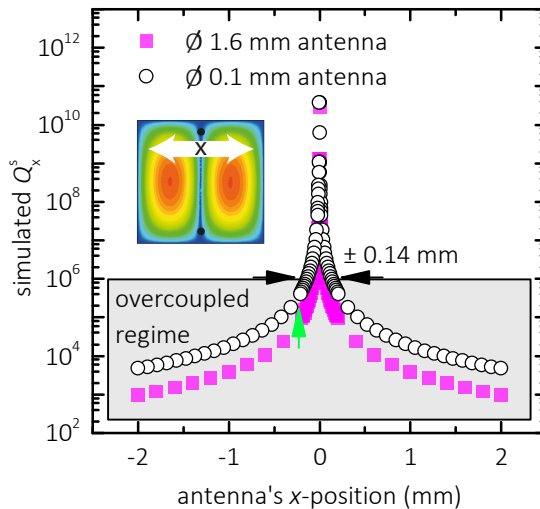


**Figure 2.4:** Simulation of the TE201 mode external  $Q$ -factor depending on the antenna  $x$ -position for two different antenna diameters (cf. Sec. C.1 in the appendix). The overcoupled regime is marked for  $Q_{\text{int}} = 1 \cdot 10^6$ . In experiment, we achieve  $Q_L \simeq 3.7 \cdot 10^5$ , which is indicated by the green arrow.

measured data. With this fit, we are able to determine the internal quality factor  $Q_0$  of the cavities. The fit parameters are summarized in Tab. 2.1.

Next, we investigate the antenna position on the cavity  $x$ -axis. In Fig. 2.4 (b), a simulation of the TE201 mode's external  $Q$ -factor is performed (cf. Sec. C.1 in the appendix). One of the antenna pins is kept at a constant position, whereas the other one is moved in the  $x$ -direction. When sweeping the antenna  $x$ -position, the electric field antinode of TE201 is crossed. Exactly in the center between the field maxima at  $x = 0$ , the coupling vanishes and  $Q_{\text{ext}}$  becomes several orders of magnitude larger. This increase of  $Q_{\text{ext}}$  is also determined by the diameter of the antenna. Two antenna geometries are simulated, which differ in the antenna diameter. For a slimmer antenna, the positioning window for reaching a high external  $Q$ -factor is larger than for a commercial 1.6 mm antenna<sup>5</sup>. The slim antenna is manufactured by soldering a thin 0.1 mm Au wire onto a shortened connector. The wire is centered by placing it in a 0.15 mm hole drilled in the center of the connector end.

<sup>5</sup>Huber+Suhner 23\_SMA-50-0-13

### Chip positioning and internal $Q$ -factor

The chip containing the qubit structure is clamped in between the two cavity halves. We use small pieces of ductile indium for fixation and thermalization. The cavity halves possess machined dents in a periodic pattern at the mounting edge for flexible chip positioning in the  $x$ -direction. Simulations show [cf. Fig. 2.5 (a)], how the internal  $Q$ -factor is lowered by the insertion of a dielectric medium as described in Sec. 1.1.3. First, the loss tangent of the material influences the  $Q$ -factor as described in Eq. (1.23). From the product of  $Q_{\text{diel}}$  and  $\tan(\delta)$  we obtain the susceptibility factor  $s'$ , which is constant for each mode and causes the offsets of the curves. A mode with high  $s'$  is less susceptible to the insertion of a dielectric at a specific position. This can be seen at the example of the TE202 mode, where the dielectric chip is placed at a field node [cf. Fig. 2.5 (c)]. Hence, its influence on the mode is small and a high  $Q$ -factor is still possible.

For a better understanding of the effect of off-center chip positions, we fix the loss tangent to 0.01 and let the chip move from cavity edge to edge along the  $x$ -axis in a simulation [cf. Fig. 2.5 (b)]. We confirm that, if the chip is at a field antinode, the  $Q$ -factor is spoiled most and the field is also distorted<sup>6</sup> as it can be seen for the TE201 mode in Fig. 2.5 (c). This behavior can also be seen in Fig. 2.5 (d), which is a frequency-resolved transmission measurement of the alloy cavity (cf. Tab. B.1 in the appendix) with a bare Si chip inserted in order to have similar conditions as in the simulations. The Si chip of size  $6 \times 10 \times 0.525 \text{ mm}^3$  is positioned at the center of the cavity, where we should observe a TE101 field antinode in the bare cavity case. However, the TE101 transmission peak does not appear at room temperature due to the relatively high impurity conductivity of the Si chip, which damps the mode. The situation changes at 4 K, because all charge carriers are frozen out and the dielectric damping is lowered sufficiently to let the TE101 mode reappear. This observation turns out to be advantageous for low-temperature experiments with qubits on Si chips.

### $Q$ -factor stability

For planar 2D resonators, a strong power dependence of the  $Q$ -factor is observed [60, 101, 102]. The internal quality degrades at single photon power levels. This behavior can be explained by taking into account two-level fluctuators at the substrate-metal or metal-air interface, which are saturated at higher power levels, but fluctuate at low power levels. In the case of 3D cavities, we do not encounter such a behavior. The quality factor is constant for excitation powers over several orders of magnitude down to single photon level (cf. Fig. 2.6). The bare pure Al cavity (cf. Tab. B.1 in the appendix)

<sup>6</sup>We note, that the frequencies of the TE201 mode and the TE102 mode are almost degenerate. Hence, if the chip is moved close to the center position at  $x = 0$ , the frequency of the TE201 mode becomes larger than the frequency of the TE102 mode due to a higher participation ratio of the TE102 mode at the center position.

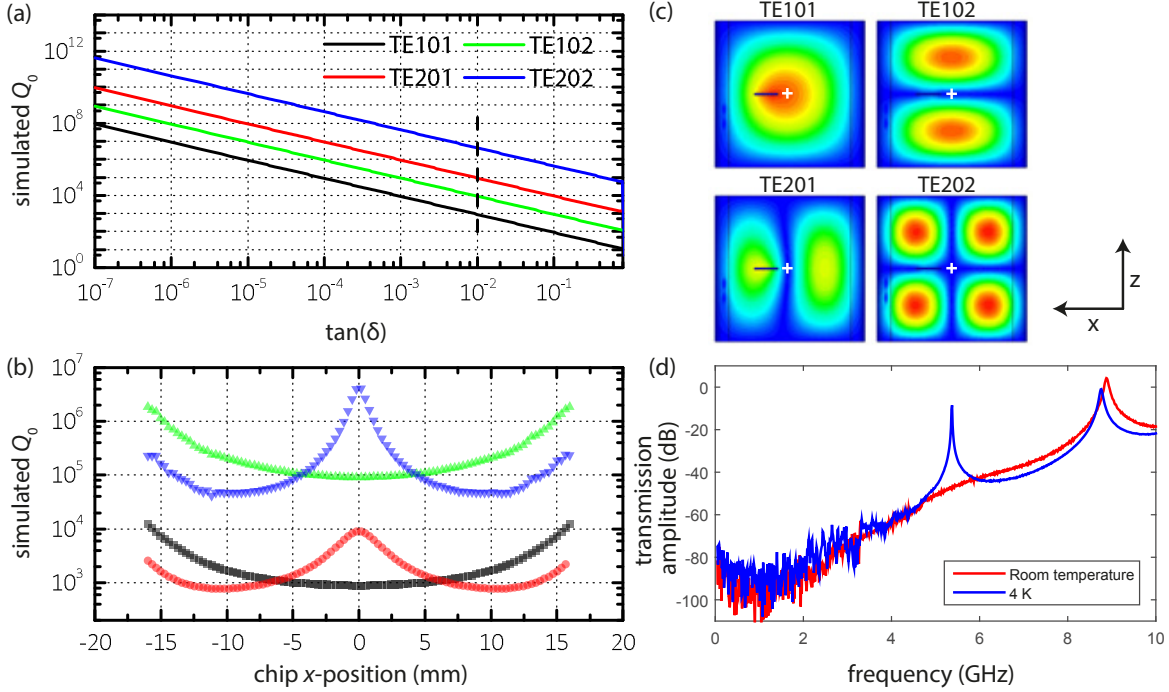


**Figure 2.5:** (a) Simulation of  $Q_0$  of four cavity modes. A chip of the size  $6 \times 10 \times 0.525 \text{ mm}^3$  is positioned in the cavity center at  $x = 0$ . The loss tangent of the chip material is varied over several orders of magnitude. The lines follow Eq. (1.23) and we obtain the susceptibility factors  $8.9, 920.2, 90.3, 43 \cdot 10^3$  for the modes in ascending order. The vertical dashed line marks the constant loss tangent used in the simulation in (b). For (a) and (b), we use a simplified cavity model (cf. Sec. C.1 in the appendix). (b) Simulation of  $Q_0$  for the same configuration as in (a). This time, the chip has a constant  $\tan(\delta) = 0.01$  and the chip position is varied in the  $x$ -direction. The internal  $Q$ -factor is affected depending on the electric field amplitude at the chip position. A high  $Q_0$  is reached when the chip is in a electric field node, such as for the TE202 mode at  $x = 0$ . (c) Simulation of the electric field amplitude for the lowest four modes. Here, the dimensions of the cavity are the same as depicted in Fig. 2.1. Due to an off-center chip placement, the modes TE101 and TE201 with significant field amplitude at the chip position are slightly distorted. The cavity center ( $x, z = 0$ ) is marked with a white cross. (d) Transmission measurement of the alloy cavity (cf. Tab. B.1 in the appendix) with a  $6 \times 10 \times 0.525 \text{ mm}^3$  undoped high-resistivity Si chip with natural oxide at the cavity center. The conductivity of the chip at room temperature due to free charge carriers is sufficiently high to fully damp the TE101 mode. At a temperature of 4 K, the charge carriers are frozen out and the TE101 mode is visible as a Lorentz peak.

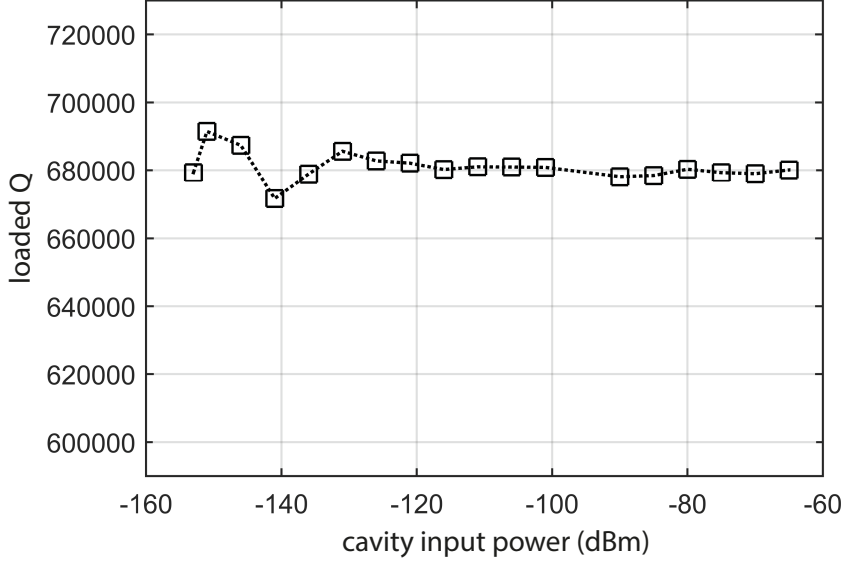


**Figure 2.6:** Loaded  $Q$ -factor for the pure Al cavity (cf. Tab. B.1 in the appendix) at 50 mK depending on probe power. The single photon power is reached at  $-115$  dBm. The slight variations at low power originate from higher fit inaccuracies due to noisy data. Graphics taken from Ref. [78].

has an internal  $Q$ -factor of  $1.5 \cdot 10^6$  for the TE<sub>101</sub> mode at 50 mK [78]. The remaining losses can be attributed to surface losses on the cavity walls.

### 2.1.2 Transmon qubit design

In order to design a transmon qubit suitable for a 3D cavity, we need to predict the transition frequency  $\omega_q$  and the coupling strength  $g$ . In the following, we show how the design of a fixed-frequency transmon qubit can be boiled down to a single parameter, the total capacitance  $C_\Sigma$ . The approximate transmon qubit frequency is given by Eq. (1.39). By taking into account the transmon qubit criterion with a targeted ratio of  $E_J/E_C \sim 50$ , we get

$$\omega_q = 19 \frac{E_C}{\hbar} = 9.5 \frac{e^2}{\hbar C_\Sigma}. \quad (2.5)$$

The dipole length  $l_q$  of the qubit parallel to the electric field determines the coupling [cf. Eq. (1.43)]. This length is mainly given by the length of the capacitance  $l_C$ . It is difficult to analytically calculate the total capacitance of the transmon qubit inside the cavity, because the capacitance to ground is defined by the geometrical distance of the capacitor paddles to the cavity walls. Therefore, we use FEM simulations to simulate the capacitances to get the correct length and width of the transmon qubit.

### Simulation of 3D transmon qubit geometry

One approach to design the size of the capacitor plates is to use the behavior of the transmon qubit as an  $LC$ -resonator. We find, that it is not sufficient to only simulate the electrostatic capacitance [103]. The basic idea behind this RF approach is to use a waveguide with a geometry similar to the 3D cavity and probe an  $LC$ -structure similar to the transmon qubit with  $\omega_{LC} = 2\pi/\sqrt{LC_\Sigma}$  [cf. Fig. 2.7 (a)]. In contrast to a cavity with discrete and narrow transmission peaks, a waveguide has the advantage of a broad bandwidth, which makes it possible to probe a large frequency range in transmission. The waveguide is modeled by expanding the cavity volume at both ends in the direction perpendicular to the transmon qubit chip surface [cf. Fig. 2.7 (b)]. Instead of the cavity walls at the ends, we define waveguide ports on each side.

The trick is then to insert a lumped element inductance  $L$  in between the two capacitive plates of the transmon circuit, such that the  $LC$ -frequency lies above the lower waveguide cutoff frequency. In our case, the frequency range between 8 to 11.5 GHz is advantageous, because it is a passband without sharp waveguide eigenmodes. We emphasize, that the modeled  $LC$ -frequency, where  $L$  is a free parameter, and the final qubit transition frequency do not have to be the same in this simulation. For a transition frequency of  $\omega_q/2\pi \approx 7$  GHz, the capacitance should be  $C_\Sigma \approx 53$  fF according to Eq. (2.5). Hence, an inductance of  $L \approx 9.8$  nH is chosen to have the  $LC$ -frequency lie in the passband of the waveguide. In the simulation, we can change the length  $l_C$ , width  $w_C$  and gap  $g_C$  [cf. Fig. 2.7 (a)] in order to move  $\omega_{LC}$  to the desired 11.29 GHz, which corresponds to the optimal capacitance. The lumped inductance  $L$  can be chosen in a relatively free manner, because we only need to match the simulation parameter  $\omega_{LC}$ . However, it is useful to choose a value close to the expected Josephson inductance  $L_J$  in order to simulate the capacitance in a similar high-frequency regime.

The ratio between  $l_C$  and  $w_C$  can be tuned to have larger or smaller coupling to the cavity electric field. For the coupling, the length  $l_q = 2l_C + g_C$  [cf. Eq. (1.43)] is the relevant factor. An electrostatic simulation approach [103] shows a linear dependence of the capacitance on  $w_C$ , whereas increasing  $l_C$  lets the capacitance rise as  $c_1 - \exp(-l_C/c_2)$  with  $c_1$  and  $c_2$  being geometric constants. As a third tuning knob, the gap capacitance depends linearly on  $g_C$ .

We validate our simulation with one 3D transmon qubit sample, which has been successfully simulated and measured (cf. sample TQ1 in Tab. B.2 in the appendix). Each capacitive plate has a dimension of  $705 \times 355 \mu\text{m}^2$  with a gap of  $50 \mu\text{m}$ , which results in  $C_\Sigma^{\text{meas}} \approx 123 \pm 49$  fF based on the transmon qubit approximations ( $E_J/E_C \approx 63$ ). The simulated capacitance is  $C_\Sigma^{\text{sim}} \approx 143 \pm 3$  fF, which lies within the measurement uncertainty. A qubit transition frequency of  $\omega_q/2\pi \simeq 3.645$  GHz and a coupling of  $g/2\pi \simeq 50$  MHz is measured. If one wants to increase the qubit-cavity coupling, a reshaping of the capacitances is possible. We need to increase  $l_C$ , however, in order to keep  $\omega_q$  the same, we need to maintain  $C_\Sigma$ , which is achieved by decreasing  $w_C$ .

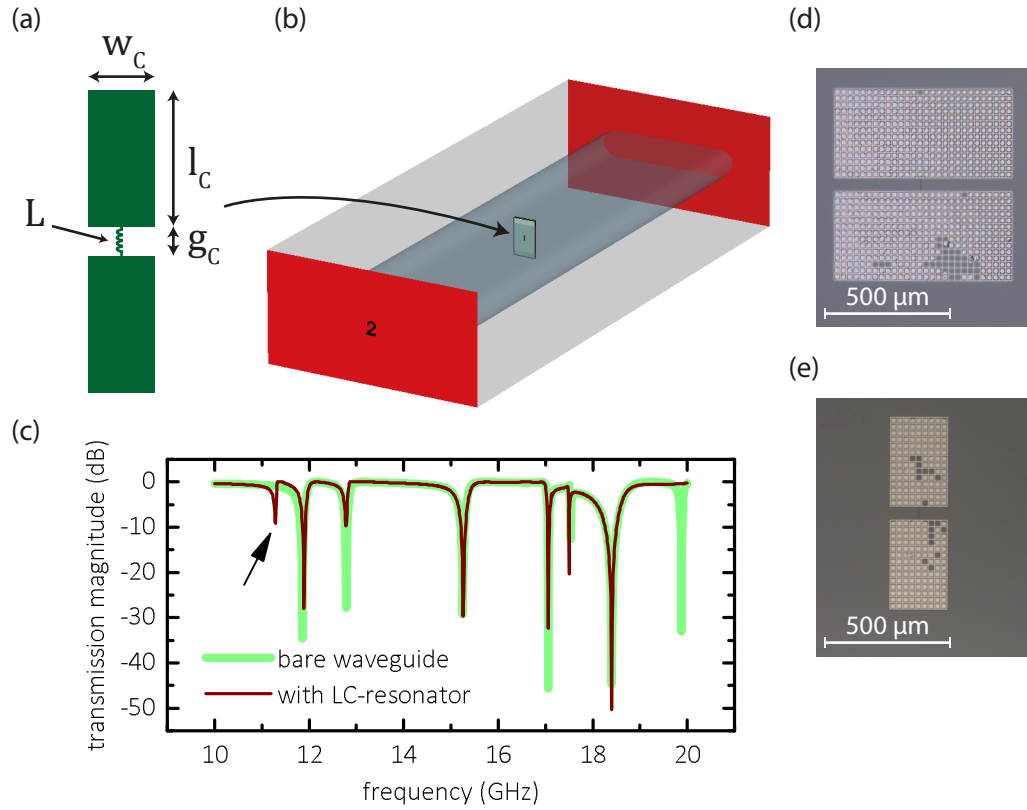


**Figure 2.7:** (a) Drawing of transmon-qubit-like  $LC$ -resonator with a lumped element inductance instead of a Josephson junction. (b) Simulation model of waveguide with  $LC$ -resonator chip inside. The geometry of the waveguide is similar to that of the 3D cavity. The red surfaces are the waveguide ports for transmission measurement. The grey transparent part is a perfect electrical conductor, which encloses the blueish colored vacuum (cf. Sec. C.1 in the appendix). (c) Transmission simulation of the model with and without  $LC$ -resonator. The additional resonance dip marked by the arrow stems from the  $LC$ -resonator and provides information on the capacitance. We note that due to the presence of the  $LC$ -resonator, the waveguide resonance close to 12 GHz also shifts slightly to higher frequencies. (d) and (e) Micrographs of transmon qubit samples with paddle length  $l_C = 355 \mu\text{m}$  and widths  $w_C = 755 \mu\text{m}$  and  $w_C = 305 \mu\text{m}$ , respectively. The grid structure consisting of  $20 \times 20 \mu\text{m}^2$  holes with  $5 \mu\text{m}$  separation is expected to pin moving flux vortices. The gap between the two paddles is  $g_C = 50 \mu\text{m}$ . A  $500 \text{ nm}$  wide bridge with the submicron Josephson junction in the center connects the two paddles.



**Figure 2.8:** Josephson junction fabrication process. The established steps are colored in turquoise, the steps in light turquoise are optional.

A small drawback of this RF method is that the waveguide differs from the cavity by having no grounded walls on two sides. Hence, the simulated transmon qubit  $C_G$  deviates from that of the real sample. However, we may argue that the contribution to the total capacitance of the transmon qubit from these two specific walls is small due to the different lengthscales of the transmon qubit itself and the cavity. Based on  $C_\Sigma \propto 1/r$ , where  $r$  is the distance from the paddles to ground, the contributions from walls further away is less than from walls close to the transmon qubit, i.e., the walls above and below. Another approach for simulating transmon qubit capacitances is the black-box quantization [83], which is a bit more accurate, because it relies on the exact cavity dimensions.

### 2.1.3 Fabrication of Josephson junctions

The fabrication process for nanoscale Josephson junctions (cf. Sec. 1.2.2), which are an essential element for superconducting qubits, is summarized in Fig. 2.8. A recipe can be found in Sec. B.3 in the appendix.

#### Fabrication overview

At the beginning, we start with a suitable substrate for the transmon qubit. In the course of this work, two different silicon substrates are used. The oxidized silicon substrate comes with a 50 nm thick thermally pre-oxidized silicon oxide layer, whereas the surface of non-oxidized silicon substrate consists only of the natural silicon oxide layer. Experiments with both substrates show that two-level systems in the silicon oxide are a significant loss channel for superconducting quantum circuits [60, 104], which, in turn, leads to limited qubit coherence times. Hence, the non-oxidized substrate is preferable. Moreover, there are attempts to remove the natural silicon oxide before spin-coating by dipping the substrate into hydrofluoric acid [105, 106] or before metal deposition by milling away the silicon oxide with Ar ions [107]. Both the oxidized and the

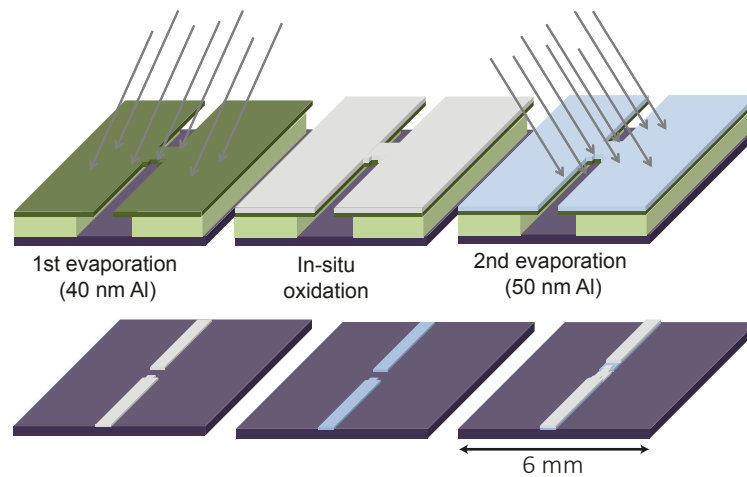


**Figure 2.9:** Schematic overview of the Dolan shadow evaporation. The substrate (purple) is covered with two layers of resist (light and dark green). In the top layer, the pattern for Josephson junction fabrication is visible after e-beam lithography and resist development.

non-oxidized substrates are undoped, have a thickness of  $525\ \mu\text{m}$  and a specific resistance of  $>1\ \text{k}\Omega\ \text{cm}$  at room temperature. The  $100\ \text{mm}$  wafers are diced into  $6 \times 10\ \text{mm}^2$  chips by the supplier<sup>7</sup>. In contrast to planar qubit-resonator structures it is advantageous for 3D cavity experiments, that both sides of the substrate are polished, in order to reduce losses from an unpolished backside.

In the first fabrication step, a clean silicon chip is spin coated with a double layer resist system. The two layers are necessary for a Dolan shadow evaporation step [108] (cf. Fig. 2.9). We use an e-beam lithography system to write the pattern for the Josephson junctions and other circuit elements onto the chip. After resist development, two aluminum layers are evaporated from different angles onto the chip with an in-situ oxidation in between to obtain the typical sandwich structure of a Josephson junction. The specific pattern for the Josephson junctions creates overlap areas of the two metal layers separated by a thin oxide barrier.

For further details, we refer to the fabrication recipe in Sec. B.3 in the appendix and to Refs. [107, 109, 110]. In a chronological order, the spin coating process and e-beam focusing was optimized in Ref. [109]. In Ref. [110], the structure development and the yield of working Josephson junctions was made reliable, and in Ref. [107] the new e-beam lithography system was set up and the oxidation was analyzed. Hence, in this work, we only focus on the principal points necessary for transmon qubit junctions. The two key steps of the process are the nano-patterning to define the size of the Josephson junction and the metallization with in-situ oxidation to define the thickness of the oxide barrier.

<sup>7</sup>CrysTec GmbH Kristalltechnologie

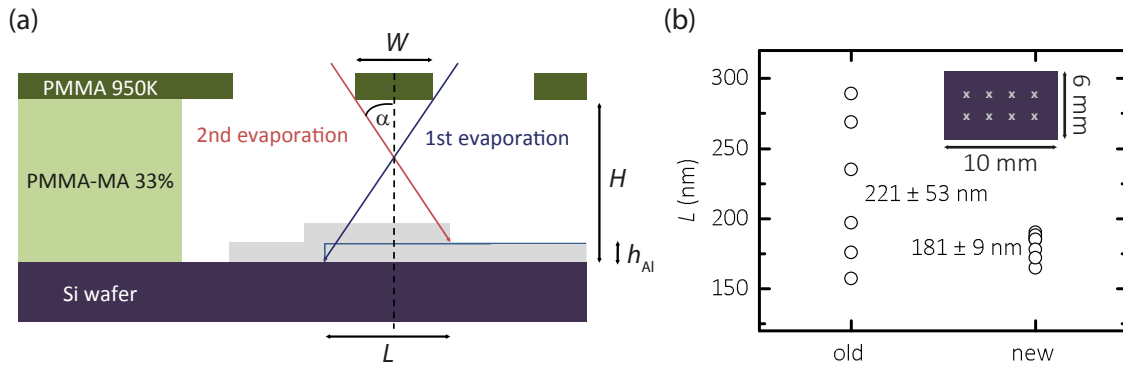


**Figure 2.10:** (a) Schematic view of metal deposition during Dolan shadow evaporation. The Josephson junction overlap  $L$  can be calculated from the tilting angle  $\alpha$  and the height  $H$  of the bottom resist as stated in the text. The height  $h_{Al}$  of the first metal layer can be neglected. (b) Measured  $L$  from two different samples using a scanning electron microscope. We compare the resulting overlaps from the old and the new spin coater. The numbers are the average value and the standard deviation of the data. The inset shows the positions (x) of the fabricated Josephson junctions on one chip.

### Double layer resist system

The double layer resist system<sup>8</sup> consists of a 690 nm bottom layer of PMMA-MA 33% and a 70 nm top layer of PMMA 950K. The latter one acts as a mask during evaporation and defines the final structure resolution. The quality of this resist system in terms of the homogeneity and the surface flatness is important for subsequent process steps. In particular for the Dolan shadow evaporation, the area of the Josephson junction depends strongly on the thickness  $H$  of the bottom resist as pointed out in Fig. 2.10 (a). During the course of this work, a new spin coater has been set up<sup>9</sup>. For benchmarking the resist quality [107], we fabricate Josephson junctions on two separate chips using the old<sup>10</sup> and the new spin coater and investigate the spread of the junction overlap length  $L$  [cf. Fig. 2.10 (b)]. From this data, we obtain the thickness variations via  $\Delta H = \Delta L \tan(\alpha)$ , where  $\alpha = 17^\circ$  is the tilting angle during the evaporation. The old spin coater produces resist thickness variations of approximately 230 nm throughout the whole  $6 \times 10 \text{ mm}^2$  chip compared to 80 nm for the new spin coater. This number of resist thickness variations does not include the edge beads [109] of the chip, since the evaluated positions on the chip are 2 mm away from the chip edge. The flatter and more homogeneous resist layer leads to more reliable initial conditions for the e-beam lithography.

<sup>8</sup>The trade names are AR-P 617.08 for PMMA-MA 33% and AR-P 679.02 for PMMA 950K from Allresist.

<sup>9</sup>New spin coater Laurell WS-650 since 2015

<sup>10</sup>Old spin coater BLE Delta 20BM

## Electron beam lithography

E-beam lithography relies on the principle of a focused beam of accelerated electrons patterning an arbitrarily designed structure onto a substrate covered with suitable resist. Typically, the resist contains long polymer chains [111], which are broken up due to the electron bombardment at a certain critical dose. In the case of positive resist, these patterned areas can be dissolved and removed in a subsequent development step [112]. Compared to standard photo lithography with a pre-manufactured mask, e-beam lithography surpasses the limits in terms of lateral resolution and offers a higher pattern design flexibility.

During the course of this work, a new e-beam lithography system<sup>11</sup> has been set up at the WMI. Here, we give a summary of the relevant features, which enable reproducible Josephson junction fabrication. The system offers a large writing area of up to  $200 \times 200 \text{ mm}^2$  [113], which enables us to load multiple smaller samples at once. In order to pattern such a large area in a reasonable amount of time, the beam deflection coils are controlled by DACs with a 55 MHz rate with 20 bit resolution combined with a fast moving stage<sup>12</sup> [113]. Features of minor fabrication importance, but simplifying sample processing, are the multiple chuck system with a robotic loading arm and the scripting of lithographic sequences.

The most important aspect is the maximum accelerating voltage of  $V_e = 100 \text{ kV}$ . For low  $V_e$ , back scattering of the electrons occurs, which means that the electrons are scattered at molecules in the resist or at the substrate surface causing undesired secondary exposure of the resist known as the proximity effect [114, 115]. Hence, for a high accelerating voltage, this effect is drastically reduced by  $\sim 1/V_e^2$  [109, 116], since the electrons simply pass through the material on a straight trajectory. Monte-Carlo simulations in Ref. [109] and experimental analysis in Ref. [107] confirm this behavior. For the fabrication of Josephson junctions, however, a certain amount of proximity effect is necessary, in order to make the Dolan shadow evaporation work. In detail, the bottom resist has to be exposed without damaging the top resist. This can be achieved automatically by back scattered electrons when  $V_e$  is low enough<sup>13</sup>. When using high  $V_e$ , which offers a more precise beam, we artificially mimic the proximity effect by a second exposure step with a slightly larger ghost pattern exposed with a lower dose [cf. Fig. 2.11 (a)]. We choose the correct dose such that the top resist, which has a higher critical dose, is not affected, but the bottom resist is exposed. A dose ratio of 1:0.19 for the actual pattern and the ghost pattern gives reliable results for the before mentioned resist system.

According to the manufacturer, the nB5 system can focus the e-beam to a beam size

---

<sup>11</sup>NanoBeam nB5 system with 100 kV acceleration voltage

<sup>12</sup><100 ms for moving 0.5 mm.

<sup>13</sup>The former e-beam system Phillips SEM XL30sFEG with a RAITH stage has a maximum accelerating voltage of 30 kV.

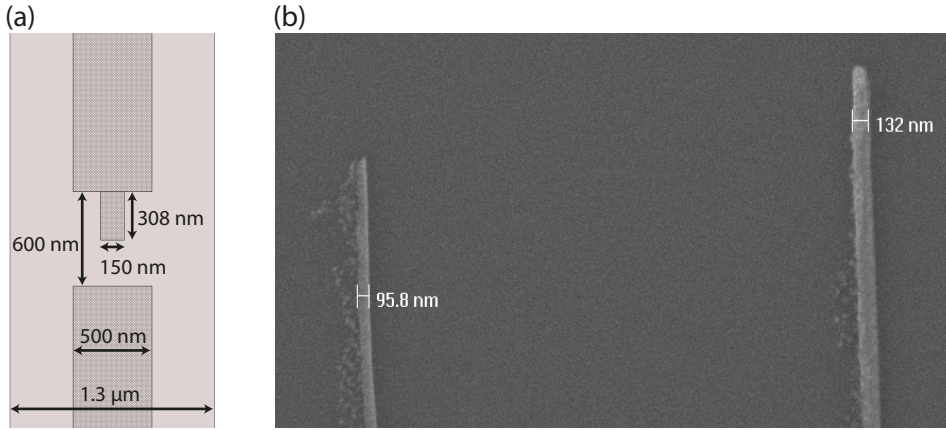


**Figure 2.11:** (a) Pattern used for Josephson junction with ghost exposure ( $1.3\ \mu\text{m}$ ) to create the necessary undercut in the bottom resist. The standard Josephson junction pattern (shaded) is overlaid with a wider ghost pattern (light brown). (b) Scanning electron micrograph of a test structure. The lines are designed to have a width of 50 nm and 100 nm, respectively.

of  $<6\ \text{nm}$  at 3 nA beam current [113] under optimal conditions. This value surpasses the resolution of the applied resist, which is 6 nm to 10 nm for the top resist PMMA 950K [111, 117]. In Fig. 2.11 (b) we show a performance test of structures with a designed width of 50 nm and 100 nm, respectively. After lift-off, the evaporated metal structures are slightly larger than expected. Nevertheless, by taking inaccuracies in resist development and beam focusing into account, we are able to safely fabricate structures with a resolution of approximately 100 nm, which is sufficient for our demands.

### Josephson junction critical current density

One important parameter of the Josephson junction is the critical current density  $j_c$ . It defines the Josephson energy  $E_J = j_c A_{JJ} \Phi_0 / 2\pi$  (where  $A_{JJ}$  is the overlap area of the Josephson junction) and, hence, the transition frequency of the transmon qubit according to Eq. (1.43). As pointed out in the previous section, the qubit transition frequency can be expressed via the transmon qubit criterion with a targeted ratio of  $E_J/E_C \sim 50$  as  $\omega_q = 19E_J/(50\hbar)$ . Therefore, we can write the critical current density as

$$j_c = \frac{2\pi}{\Phi_0} \frac{E_J}{A_{JJ}} = \frac{50\hbar}{19\Phi_0} \frac{2\pi\omega_q}{A_{JJ}}. \quad (2.6)$$

This equation enables us to check fabricated junctions by measuring the transmon qubit transition frequency, but more importantly, it gives a first estimation of the required  $j_c$  for a desired  $\omega_q$ . The critical current density usually is required to be much lower for transmon qubit junctions than for, e.g., flux qubit junctions. Taking into account the resolution of our NanoBeam nB5 e-beam lithography system and the resist resolution,

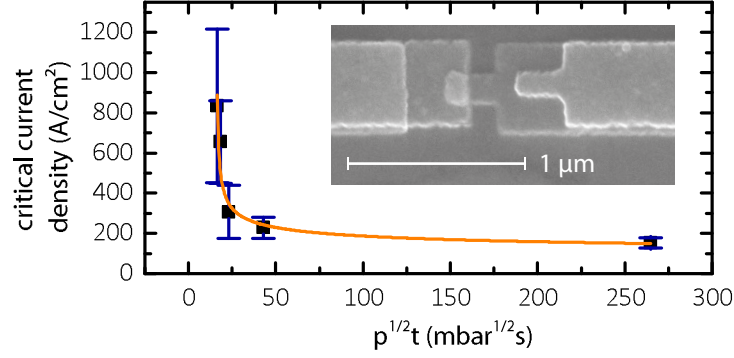


**Figure 2.12:** The  $p^{1/2}t$  law for determination of critical current densities. Inset: SEM micrograph of a Josephson junction.

we can reliably fabricate a junction with a minimal area of around  $100 \times 160 \text{ nm}^2$ . The latter value is determined by the angle used in the Dolan shadow evaporation process [108]. Using this value for the junction area, we obtain a required critical current density of  $j_c \simeq 32 \text{ A/cm}^2$  for a qubit transition frequency of  $\omega_q/2\pi = 6 \text{ GHz}$ . The critical current density is defined by the thickness of the oxide barrier of the Josephson junction. Thicker oxide barriers turn out to be more reproducible and follow the phenomenological  $p^{1/2}t$  law, which describes the oxidation in terms of oxygen pressure  $p$  and oxidation time  $t$ . This law is a result of the Carbera-Mott theory for the formation of thin oxide films [107, 118]. The critical current density can then be expressed as

$$j_c = \frac{a\kappa}{\sinh \left\{ 0.664\kappa [\ln(2p^{1/2}t + c)]^{2/3} \right\}} \quad (2.7)$$

where  $a$ ,  $\kappa$  and  $c$  are material constants. The units for pressure and time are  $[p] = \text{mbar}$  and  $[t] = \text{s}$ . We use these three parameters as fitting parameters and obtain the fit shown in Fig. 2.12. For our material system, the values of these parameters are summarized in Tab. 2.2. Due to the comparably low  $j_c$ , the oxidation of transmon qubit Josephson junctions is almost neither time nor pressure critical, which leads to stable fabrication conditions.

Fit parameter	Fit result
$a / 10^{-7} \text{ Acm}^{-1}$	$554.26 \pm 280.70$
$\kappa / \text{nm}^{-1}$	$0.77 \pm 0.69$
$c / \text{mbar}^{1/2}\text{s}$	$-31.08 \pm 1.62$

**Table 2.2:** Fitting parameters for the  $p^{1/2}t$  law using Eq. (2.7).

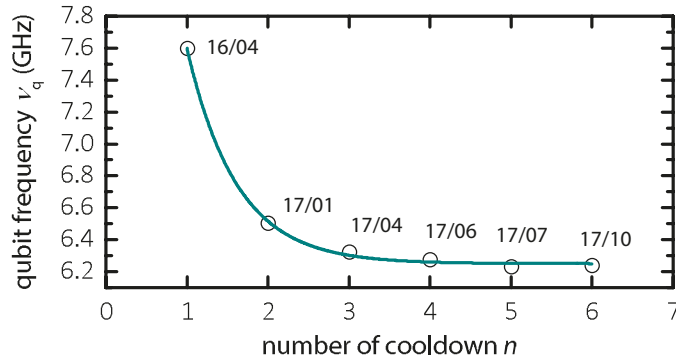


**Figure 2.13:** Aging of a transmon qubit Josephson junction. Before every cooldown, the sample (cf. sample QMv3 in Tab. B.2 in the appendix) is exposed to ambient conditions for several days. During the cooldown, the aging is stopped due to the sample being in an evacuated environment. The change of the qubit frequency clearly follows an exponential trend  $\nu_q(n) = \nu_{q,0} + A \exp(-n/N_0)$  (turquoise) with a base frequency of  $\nu_{q,0} = 6.25$  GHz, an amplitude  $A = 1.3$  GHz and a "decay time" of  $N_0 = 0.62$ . The numbers next to the data points are the year and month of the beginning of a cooldown.

### Effect of thermal cycling

Our Josephson junctions are defined by a 5 to 10 Å [110] thin oxide barrier sandwiched between two thin layers of superconducting aluminum. On top of the upper aluminum layer, a natural oxide forms when the structure is exposed to ambient conditions. Although the oxidation of an aluminum surface tends to stop naturally after a few nanometers, the effect of junction aging has been reported occasionally [119]. This implies, that the thickness of the oxide barrier increases, resulting in a lower critical current. For a transmon qubit, this means that the transition frequency decreases as  $\nu_q \sim \sqrt{I_c}$ . We report on the effect of thermal cycling of one sample, where the sample has been exposed several times to ambient conditions in between the cooldowns (cf. Fig. 2.13). We note that the frequency drop does not depend on the time between the cooldowns<sup>14</sup> or the duration of the cooldown, but only on the number of cycles. The drop in qubit frequency points to an increase of the insulating oxide barrier thickness  $d$  of the Josephson junction [ $\nu_q \sim \exp(-d)$ ] [110]. A possible explanation for this behavior could be a change in the boundary conditions for the oxide barrier, such as mechanical stress, during the cooldown or heatup procedure. To circumvent or at least reduce such changes in the qubit frequency, it is possible to post-oxidize the sample in a controlled manner after the deposition of the second metal layer [90].

<sup>14</sup>Between the cooldowns, the inner vacuum chamber of the cryostat is often not vented. However, if it is vented for changing samples or the cabling, which takes up to a few days, we restore the vacuum of the inner vacuum chamber immediately. Hence, the samples typically remain most of the time in evacuated conditions.

## 2.2 Qubit spectroscopy

In order to investigate the characteristics of a transmon qubit, it is necessary to cool it below  $T \ll E_q/k_B$  to prevent thermal excitations. We start by reviewing the cryogenic setup. Next, we describe the frequency domain measurements, and afterwards move on to the time domain.

### 2.2.1 Cryogenic setup

The apparatus for cooling qubit samples and other necessary microwave equipment to a few tens of millikelvin above absolute zero is complex.  $^3\text{He}$ - $^4\text{He}$  dilution cryostats are suitable for this task, because of their continuous operation, sufficient cooling power and sample space [cf. Fig. 2.14 (a)]. In a simplified picture, a dilution cryostat is based on the principle of creating a non-equilibrium state between an  $^3\text{He}$ -dilute and an  $^3\text{He}$ -rich phase by pumping away  $^3\text{He}$  from the dilute phase. Then,  $^3\text{He}$  from the  $^3\text{He}$ -rich phase needs to get dissolved into the  $^3\text{He}$ -dilute phase across the phase boundary. The enthalpy for this process provides the cooling power to remove heat from the surrounding. We use a home-made liquid  $^4\text{He}$  precooled dilution cryostat for our experiments, which is described in more detail in Ref. [120]. Typically, a cryostat has several temperature stages, where the components necessary for qubit experiments are located. To some of the stages, a radiation shield is mounted [cf. Fig. 2.14 (b)].

The RF input line is thermally anchored with attenuators at specific stages to protect the sample from thermal radiation via the cable inner or outer conductor. At the sample stage, which has a base temperature of approximately 30 mK, the input line is filtered with a low-pass filter<sup>15</sup> with a cutoff frequency of 12 GHz to limit the spectrum to the bandwidth of interest, and thereby keeping high-frequency noise away from the qubit. A second filter of the same kind is inserted in the output line. One qubit sample (cf. sample QMv4 in Tab. B.2 in the appendix) measured with and without these filters exhibits a shifted transition frequency. By inserting a filter in the input and output line, the qubit frequency rises from 5.284 GHz to 5.360 GHz. This is most probably a result of an increased critical current of the Josephson junction due to less high frequency noise [21, 121]. When taking into account the aging of the junction (cf. Sec. 2.1.3), which leads to a lower critical current, the real increase of  $I_c$  must be even larger. The changes are summarized in Tab. 2.3.

The sample itself is thermally anchored to the sample stage and has an heater and a thermometer attached for individual temperature control. Thermal anchoring of a bulk superconducting cavity proves to be more demanding than of a normal metal box, because a superconductor has a very low thermal conductivity [122]. We have tested three different methods, which are shown in Fig. 2.15, and come to the conclusion that

---

<sup>15</sup>K&L 6L-250-12000 tubular filters

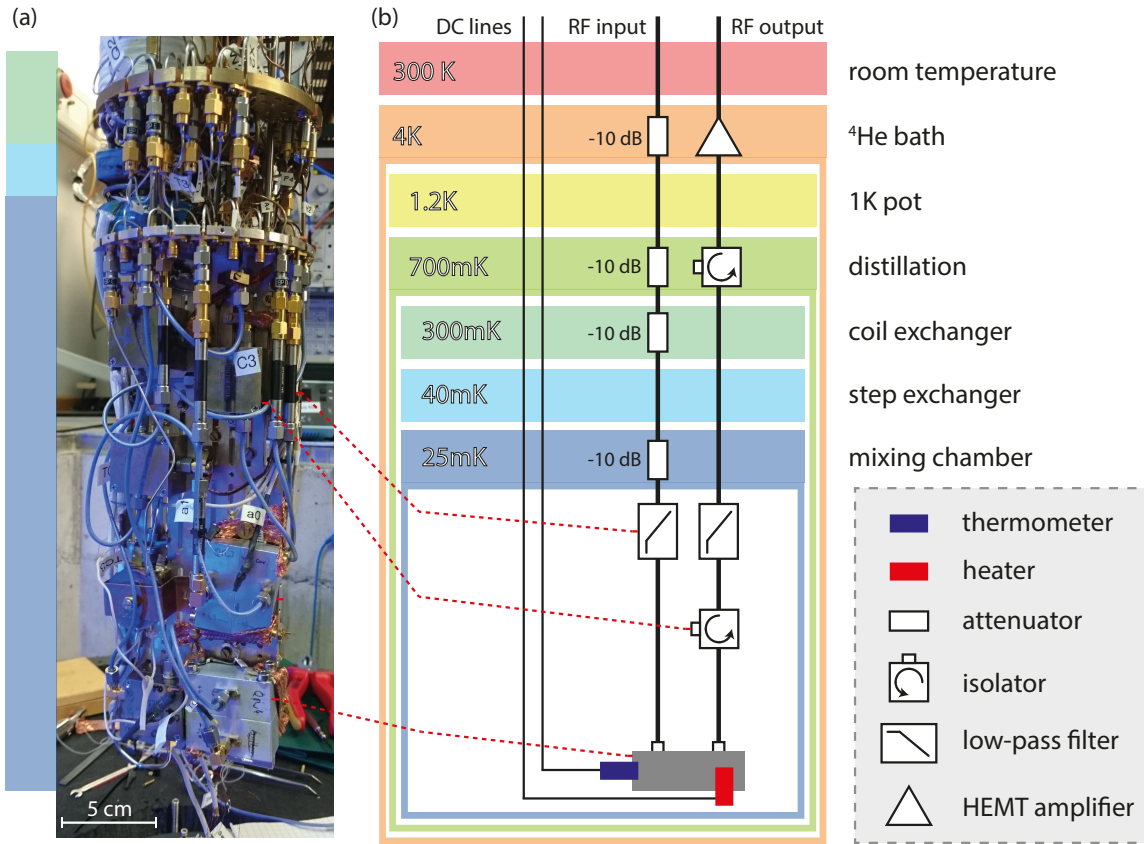


**Figure 2.14:** (a) Photograph of the cryostat sample stage before cooldown. (b) Cryostat setup scheme with all relevant microwave components. For simplicity, only one of several mounted cavities is shown.

		without filters	with filters
$\omega_q/2\pi$	(GHz)	5.284	5.360
$I_c$	(nA)	23.1	24.1
$C_\Sigma$	(fF)	63.7	64.6
$\alpha/h$	(MHz)	-304	-300

**Table 2.3:** Parameters of a transmon qubit with and without cryogenic K&L tubular low-pass filters.  $I_c$  and  $C_\Sigma$  are calculated using the transmon qubit formulas in Sec. 1.2.3. This sample has  $E_J/E_C \approx 40$ , hence the transmon qubit approximation is valid (cf. sample QMv4 in Tab. B.2 in the appendix).

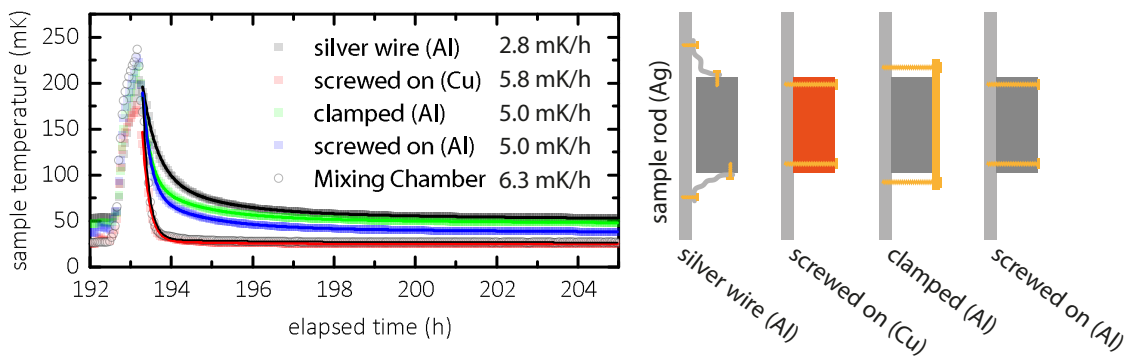


**Figure 2.15:** Different sample mounting techniques and the corresponding thermalization. The elapsed time of 192 h from the beginning of the cooldown ensures base temperature at all components. For a simultaneous and homogeneous heatup, the mixing cycle is stopped for approximately 30 min and then restarted again. The fitting function is a sum of three exponential decay functions in the form of  $\sum A_i \exp(-r_i t)$ , because, most probably, at least three different heat transfer channels contribute in total. We give the cooling rates  $r_i$  of the leading one, which is the one with the highest amplitude  $A_i$ .

screwing the 3D cavity directly to the sample rod with a large contact area works best. Second comes the clamping type thermalization, which has the same cooling rate, but gives a base temperatures higher by 10 mK. Silver wire thermalization may only be used in addition to the before mentioned methods, but on its own it does not let the sample reach its base temperature sufficiently fast due to the limited contact area.

For the RF output line, attenuators cannot be used for thermalization, because of the low-level measurement signal. Therefore, circulators are used, which break the time symmetry in such a way, that thermal radiation from higher temperature stages is dissipated in a cold  $50 \Omega$  termination, but the measurement signal from lower stages can pass through. They are also important for blocking the back action signal from the cryogenic amplifiers. The measurement signal is amplified by these amplifiers with a low noise temperature at 4 K, before it leaves the fridge for further analysis.

### 2.2.2 Single-tone transmission measurement

We first characterize the bare cavity transmission using a vector network analyzer (VNA)<sup>16</sup> (cf. Fig. 2.16). We measure a Lorentzian shaped magnitude response for the eigenmodes. The frequency-resolved transmission magnitude  $M(\nu)$  is expressed as

$$M(\nu) = \left( \frac{G}{1+G} \right)^2 \frac{1}{2} \frac{\Delta\nu/2}{(\nu - \nu_m)^2 + (\Delta\nu/2)^2} \quad (2.8)$$

<sup>16</sup>Models of different brands have been used throughout this work: Rohde & Schwarz ZVA8/ZVB8/ZVA24 and Agilent N5222A PNA

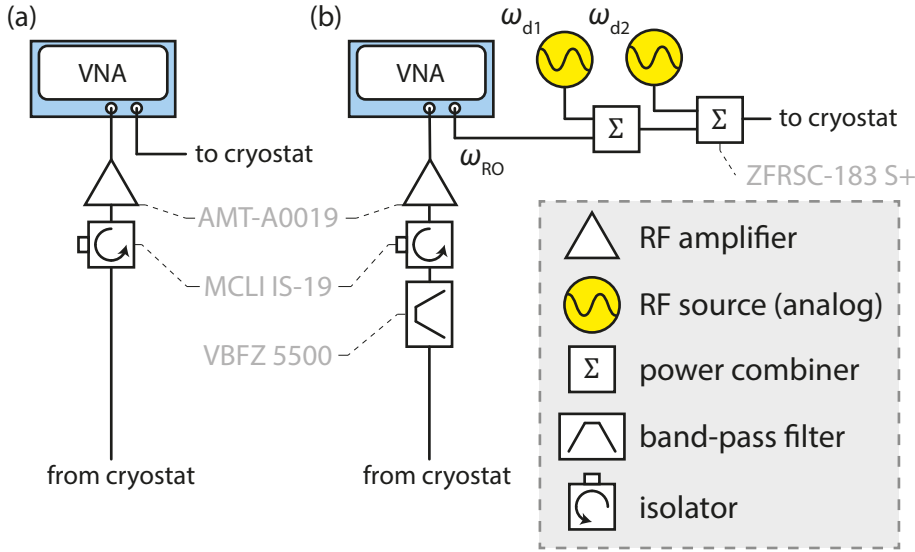


**Figure 2.16:** Transmission measurement scheme for (a) frequency sweeps and (b) continuous-wave dispersive readout at frequency  $\omega_{\text{RO}}$  with additional coherent drives at frequencies  $\omega_{\text{d1}}$  and  $\omega_{\text{d2}}$ .

where the center frequency of the Lorentzian is the mode frequency  $\nu_{\text{m}} = \omega_{\text{m}}/2\pi$ . The maximum height  $M(\nu_{\text{m}})$  gives information on the coupling coefficient  $G = \sqrt{M(\nu_{\text{m}})}/[1 - \sqrt{M(\nu_{\text{m}})}]$  [52] and the full width half maximum (FWHM =  $\Delta\nu = \kappa/4\pi^2$ ) is related to damping. The same information, except for the coupling, is contained in the phase response

$$\varphi(\nu) = -\tan^{-1}\left(\frac{2}{\Delta\nu}(\nu - \nu_{\text{m}})\right). \quad (2.9)$$

We plot both quantities in Fig. 2.17 and compare them with measured data. The measured resonator parameters are important for the resonator-assisted qubit readout explained in the next section. The full transmission spectrum is the sum of all modes which can form inside the cavity. Such a transmission spectrum is shown in Fig. 2.18 for a microwave 3D cavity at 50 mK with an off-center qubit chip (cf. sample QMv3 in Tab. B.2 in the appendix). The measured fundamental TE<sub>101</sub> mode is at 5.604 GHz. From a CST Microwave Studio [50] frequency solver simulation (cf. cavity model in Sec. C.1 in the appendix), we expect a slightly lower value of 5.591 GHz for this mode and also slightly shifted frequencies for the higher modes. We attribute this behavior partially to the shrinking of the material at low temperatures, which causes the frequencies to increase by several tens of megahertz [97]. The internal quality factor of particular modes, which have an antinode at the chip position (cf. Sec. 2.1.1), is significantly changed due to the dielectric properties of the chip. For the simulation, we assume  $\epsilon_{\text{r}} = 11.9$  for silicon, although this value is expected to be slightly lower at cryogenic temperatures, leading to less disturbance of the mode. To obtain the

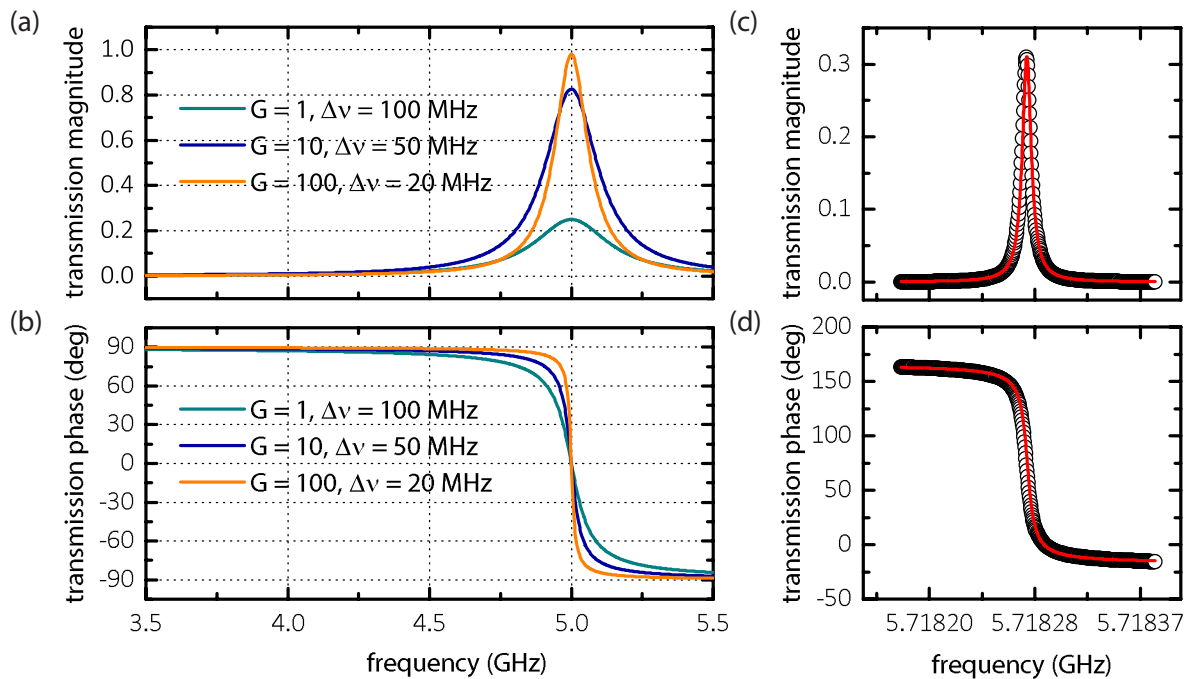


**Figure 2.17:** Theoretical (a) magnitude and (b) phase response function of a resonator measured in transmission. The resonance frequency is set to 5 GHz. (c) and (d) Calibrated measurement (dots) of the pure Al cavity (cf. Tab. B.1 in the appendix) at 50 mK. Both pins are retracted to  $-1.6$  mm and  $\kappa/2\pi \simeq 8.43$  kHz at  $\omega_{101}/2\pi \simeq 5.718279$  GHz. From the transmission amplitude, we calculate  $G \simeq 1.25$ . With  $Q_L \simeq 678000$  we obtain  $Q_0 \approx 2.25 \cdot Q_L \simeq 1.5 \cdot 10^6$  according to Eq. (1.13). The fits (line) are performed according to Eq. (2.8) and (2.9). The global phase offset in (d) is due to the measurement configuration.

frequencies of modes with low external coupling, we use the eigenmode solver and obtain the simulated frequencies of all cavity modes. In order to match the frequency results from the simulation to the ones measured for the cavity at cryogenic temperatures, we adjust the antenna pin penetration depths of the simulation model such that the frequency of the TE<sub>101</sub> mode is approximately matched. The simulation results are summarized in Tab. 2.5 up to 22 GHz.

### 2.2.3 Single-tone determination of the dispersive shift

For a coupled qubit 3D cavity system we investigate the cavity dispersive shift  $\chi$  by ramping up the power of the VNA probe tone [cf. Fig. 2.19 (b)]. Although the drive is off-resonant from the qubit frequency, at some point, the power at the qubit frequency is sufficient to saturate the qubit and to bring it into a mixed state with the expectation value  $\langle \sigma_z \rangle^2 = 0$ . According to Eq. (1.53), the resonator frequency shifts by an amount  $\chi'$  as compared to the qubit in  $|g\rangle$ . In the measurement, due to the high drive strength, also higher levels of the transmon qubit are populated and contribute to the total

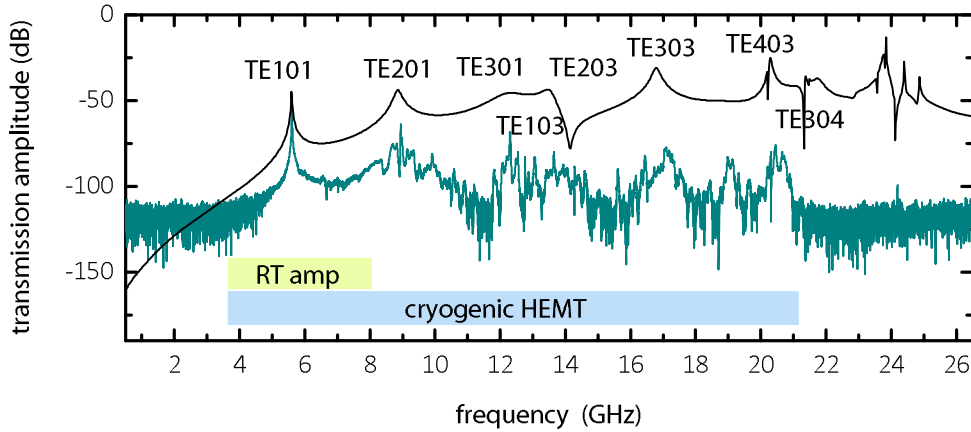


**Figure 2.18:** Frequency spectrum of a microwave 3D cavity with a single off-center qubit chip at 50 mK (turquoise) (cf. sample QMv3 2<sup>nd</sup> in Tab. B.2 in the appendix) and corresponding FEM simulation (black). Modes with a high coupling coefficient are well distinguishable and indicated. The cryogenic amplifier used in this measurement has a nominal bandwidth of 4 to 20 GHz and the amplifier at room temperature is limited to 4 to 8 GHz. Small features beside the major peaks result from higher order transitions involving the qubit or can be attributed to parasitic modes.

dispersive shift. Hence, we need to give consideration to the correction factor for the dispersive shift for the transmon qubit as given in Eq. (1.55). This correction takes into account the dispersive shift of the second excited level of the transmon qubit, which is typically sufficiently accurate.

## 2.2.4 Two-tone measurement and higher qubit levels

In order to reveal further important transmon qubit parameters, we use the dispersive readout scheme (cf. Fig. 2.19). In this scenario, the resonator is weakly probed at a fixed frequency  $\omega_{\text{RO}}$  close to the resonance frequency. If now the transmon qubit changes its state, the resonator peak shifts in frequency and, as a result, the transmission at  $\omega_{\text{RO}}$  changes accordingly. With an additional coherent drive at the qubit frequency, we excite the transmon qubit. In experiment, the frequency  $\omega_{\text{d}}$  of this additional tone is swept and the change in the probe tone amplitude or phase is measured, to obtain the transition frequency  $\omega_{\text{q}}$  of the transmon qubit (cf. Fig. 2.20). The probe tone itself has to be weak enough not to excite the qubit. However, it still causes a population of the readout resonator, leading to an AC Stark shift of the qubit frequency [cf. Eq. (1.57)], which has to be calibrated. With correctly determined values of the qubit frequency, the resonator frequency and the dispersive shift, we can calculate the detuning  $\Delta$  and the coupling  $g$  from Eq. (1.52). At high qubit drive power, we are able to excite higher levels of the transmon qubit in a process involving multiple photons. In Fig. 2.20 (a) we observe the higher levels of the transmon qubit at a sufficiently high drive power. This

Frequency (GHz)	Coupling to qubit (off-center)	Coupling to qubit (center)	Coupling to antennas	Mode $TE_{xyz}$
5.6050638	high	high	high	101
8.8500887	high	low	low	102
8.896803	low	low	high	201
11.388082	low	low	low	202
12.118731	high	high	high	301
12.773434	high	high	high	103
13.797072	high	low	low	302
14.219597	high	low	high	203
14.830305	high	low	high	203
16.363629	high	low	low	104
16.675641	high	low	high	401
17.338904	high	high	high	303
17.893519	low	low	low	402
18.01824	low	low	low	204
18.910263	high	high	high	*
20.164729	high	low	low	304
20.193551	low	low	high	403
20.212452	low	low	high	304
20.56252	high	low	low	*
20.658771	low	high	high	*

**Table 2.4:** Simulated modes of a microwave 3D cavity with a single off-center Si chip using the eigenmode solver (cf. Sec. C.1 in the appendix) and the coupling to the qubit chip and antennas. Some of the frequencies calculated by the eigenmode solver deviate from the frequency domain solver, because the antennas are neglected, however they are sufficiently accurate for a coarse estimation. The modes marked with a star do not follow the bare cavity modes  $TE_{xyz}$  numbering scheme, since they occur only due to the insertion of the chip and the antennas.

kind of measurement is necessary in order to calculate the anharmonicity  $\alpha$

$$\alpha = \hbar(\omega_{\text{gf}} - 2\omega_{\text{q}}) \approx -E_C \quad (2.10)$$

and obtain the value of the capacitance  $C_\Sigma = e^2/2E_C$ . When the anharmonicity of the qubit is known, a refinement of the coupling strength  $g$  can be done by using Eq. (1.55). In addition, we can draw conclusions on the size of  $E_J$  from  $E_C$  by using the relation in Eq. (1.39). In the end, by measuring the anharmonicity, we disclose the basic parameters of the transmon qubit, namely the total capacitance  $C_\Sigma$  and the critical current  $I_c$ . In App. A.1, we summarize the measurement strategy for characterizing a transmon qubit from scratch.

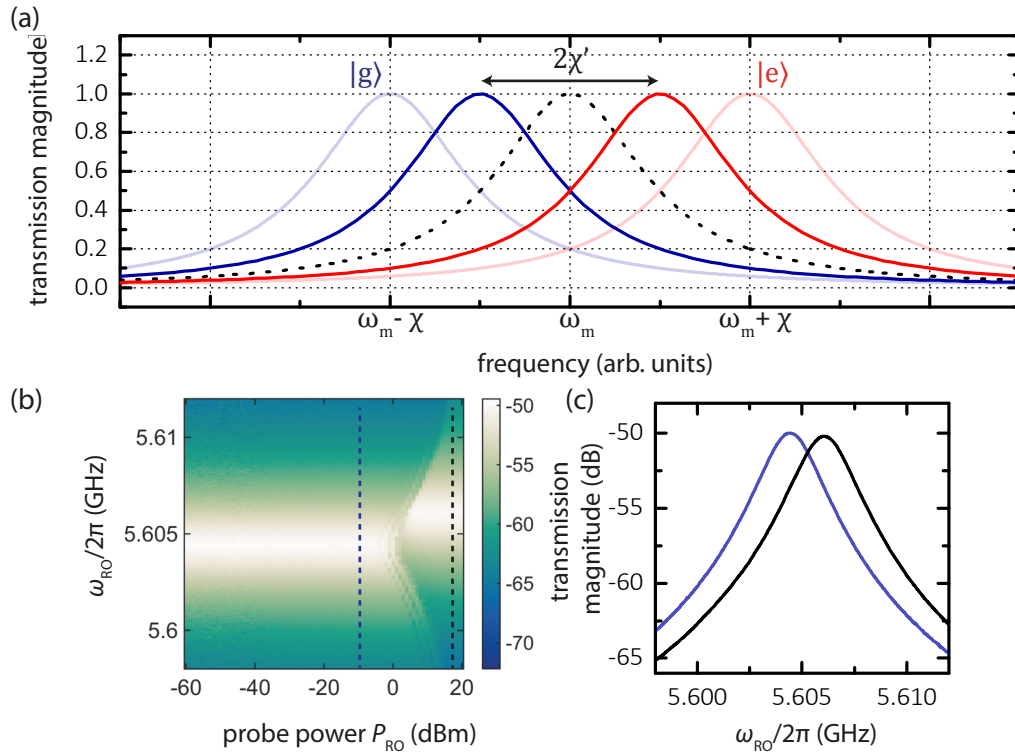


**Figure 2.19:** (a) Scheme for dispersive readout in the case of a negative  $\chi$ , which is valid for a qubit frequency higher than the cavity mode frequency  $\omega_m$ . The transmon qubit cavity pull  $\chi'$  is reduced compared to that of an ideal two-level system (light red and blue lines) according to Eq. (1.54). (b) Single-tone transmission measurement of the readout mode (cf. sample QMv3 1<sup>st</sup> in Tab. B.2 in the appendix). For low probe powers up to approximately 0 dBm at the VNA output, the qubit stays in  $|g\rangle$ . When moving to higher powers, the qubit is excited into a mixed state, which shifts the resonator frequency up by  $\chi'$ . The cuts discussed in (c) are marked by the vertical dashed lines. (c) Vertical cuts at  $-10$  dBm and  $18$  dBm. We can extract  $\chi' = -1.6$  MHz for this sample. Negligible deviations on the order of  $0.2$  dB in the height of the resonance peak come from the frequency-dependent gain of the amplification chain.

### 2.2.5 AC Stark shift and photon number calibration

The AC Stark shift of the qubit frequency described in Eq. (1.57) provides an elegant way to calibrate the input power with sub-single photon accuracy. This calibration is necessary, because for the dispersive readout, the readout power should stay below one photon on average in the cavity to enable a quantum non-destructive (QND) measurement [120]. Moreover, the bare qubit frequency is obtained from such a calibration. Figure 2.21 shows an experimental example<sup>17</sup>. We perform a dispersive readout for different readout powers and find a linear relation between the linearized

<sup>17</sup>This data is recorded for the same qubit QMv3 as in Fig. 2.20, however in a different cooldown without intermediate exposure of the sample to ambient conditions. Therefore,  $\nu_q$  has dropped slightly from  $7.6$  GHz to  $7.54$  GHz.

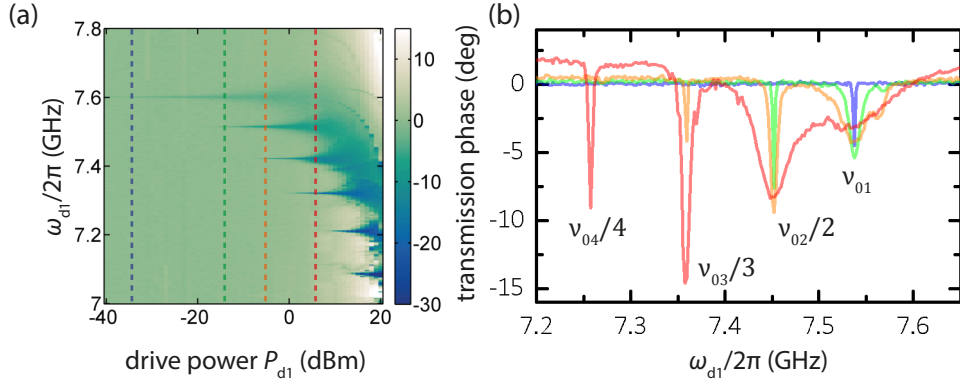


**Figure 2.20:** (a) Two-tone spectroscopy of higher qubit levels. We plot the transmission phase as a function of the qubit drive frequency  $\omega_{d1}$  and the qubit drive power  $P_{d1}$  (cf. sample QMv3 1<sup>st</sup> in Tab. B.2 in the appendix). (b) Vertical cuts at the positions indicated by the dashed lines in (a). At low drive power, only the lowest qubit transition is visible (blue). If the drive power is increased, the lower qubit transitions start to power broaden (green) and higher order processes occur, which lead to an excitation of the higher qubit levels (orange, red). Moreover, the dispersive readout is disturbed at high drive power due to extensive AC Stark shifts in the system, which is visible in the phase offset of the red curve.

readout power and the qubit frequency. By extrapolating the power to zero, we obtain the bare qubit frequency  $\omega_q$ . The average photon number can be calculated from the input power with Eq. (1.16) and the dispersive shift  $\chi'$  per photon [123].

Moreover, the qubit transition is affected by measurement induced dephasing. At higher probe powers, the transition dip becomes broader. Therefore, we can use this effect to estimate the qubit decoherence time  $T_2$  using [124]

$$\pi\Delta\nu = \sqrt{\left(\frac{1}{T_2}\right)^2 + n_p(2g)^2\frac{T_1}{T_2}}. \quad (2.11)$$

Here,  $n_p$  denotes the number of probe photons. If we extrapolate the FWHM in Fig. 2.21 (c) to zero power,  $\Delta\nu = \gamma/4\pi^2$  is a direct estimation of the decoherence time

$$T_2 = \frac{1}{\pi\Delta\nu}. \quad (2.12)$$

From this estimation, we get  $T_2^{\text{est}} \simeq 3.31 \mu\text{s}$ . With a Ramsey-type time domain measurement [cf. Fig. 2.21 (d)], we confirm the decoherence time to be  $T_2^{\text{q}} = 3.4 \mu\text{s}$  for this specific qubit (cf. sample QMv3 1<sup>st</sup> in Tab. B.2 in the appendix). Details on the time domain measurement setup can be found in Sec. 2.3. The small difference between these values can be accounted for by fit errors during the determination of the FWHM from the data and to errors of the linear fit. At a relatively high probe power, also other cavity modes are excited, which contribute to the frequency shift. This can be

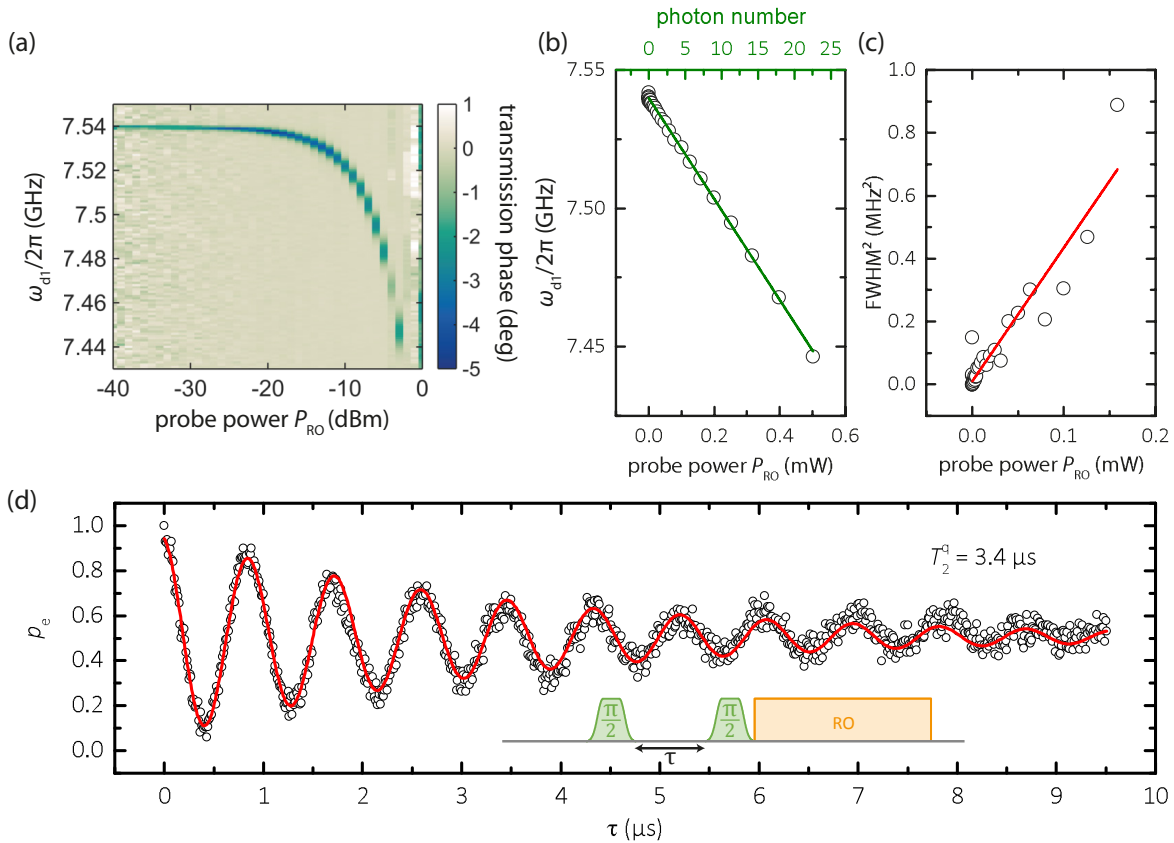


**Figure 2.21:** (a) Qubit frequency shift depending on probe power (cf. sample QMv3 1<sup>st</sup> in Tab. B.2 in the appendix). (b) Photon number calibration using the AC Stark shift. One photon on average is excited in the cavity at 22  $\mu$ W output power at the RF source. (c) Squared FWHM of the qubit transition against probe power. We limit the probe power range to lower values to increase the fit fidelity. (d) Time domain measurement for the determination of  $T_2^q$ . Red line: fit. Inset: Ramsey-type pulse sequence.

seen in Fig. 2.21 (a) near 0 dBm probe power. The qubit transition cannot be clearly distinguished anymore from other system excitations. To estimate this effect, we need to selectively excite the modes, which is discussed in the next paragraph.

## 2.2.6 Triple-tone measurement

The setup is extended with a second microwave source with drive frequency  $\omega_{d2}$  [cf. Fig. 2.16 (b)]. Together with the VNA, which supplies the continuous wave readout tone, three coherent microwave tones can be applied to study higher order effects or to selectively probe certain transitions.

### Qubit assisted measurement of higher qubit-cavity modes

With a triple-tone setup, we are able to quantitatively measure higher modes of the cavity-qubit system and their coupling to the qubit, even though they are beyond the bandwidth of the cryogenic amplifiers, which are typically limiting the frequency range for the experiment. To this end, we again readout dispersively with a low readout power at  $\omega_{\text{RO}}$  and sweep  $\omega_{\text{d1}}$  through the qubit transition frequency (or any other transition in which the qubit contributes to) to monitor AC Stark shifts of the qubit. The drive  $\omega_{\text{d2}}$  is an additional, selective mode populating drive, which we scan over a broad range. If now a mode with frequency  $\omega_m$  is populated, the qubit experiences an AC Stark shift, which is recorded as a frequency dip ( $\omega_q < \omega_m$ ) or peak ( $\omega_q > \omega_m$ ). In contrast to a two-tone measurement, where only one additional drive can be swept in frequency, since  $\omega_{\text{RO}}$  is fixed at a frequency close to the readout mode for dispersive readout of the qubit, here, we have two frequency tunable drives available. As a result, we can make use of the sensitivity of the qubit transition on the cavity photon population and make statements on the frequency-resolved parameters of the cavity modes.

In Fig. 2.22 we present such a triple-tone measurement on the blue sideband transition. We use a similar approach to Eq. (1.66), which we extend to multiple modes, to fit the curves. In detail, this means that we quantify the frequency shift with the AC Stark shift term  $\Omega_{\text{d2}}^2 \cdot 4g^2 / [(\omega_m - \omega_{\text{d2}})^2 (\omega_q - \omega_{\text{d2}})]$ . If we limit our investigation to 5 modes between 11.5 GHz to 13 GHz,  $m1$  to  $m5$ , the total frequency shift is the sum of the single shifts caused by each of the five modes, and we obtain

$$\omega'_q = \omega_q + \sum_{i=1}^5 \frac{\Omega_{\text{d2}}^2}{(\omega_{mi} - \omega_{\text{d2}})^2} \frac{4g_i^2}{\omega_q - \omega_{\text{d2}}} = \omega_q + \sum_{i=1}^5 \frac{\Omega_{\text{d2}}^2}{\tilde{\Delta}_{mi}^2} \frac{4g_i^2}{\tilde{\Delta}_q}, \quad (2.13)$$

where the index  $i$  enumerates the modes. Until now, the modes are assumed to be lossless, which is reflected in an infinitely sharp peak in frequency space. To describe our data correctly, we need to introduce a linewidth  $\Delta\omega_{mi}$  for each mode and obtain a fitting function

$$\omega'_q = \omega_q + \sum_{i=1}^5 \pi \frac{\Delta\omega_{mi}/2}{(\omega_{mi} - \omega_{\text{d2}})^2 + (\Delta\omega_{mi}/2)^2} \frac{8(\Omega_{\text{d2}}g_i)^2}{\pi\Delta\omega_{mi}(\omega_q - \omega_{\text{d2}})} \quad (2.14)$$

$$= \omega_q + \sum_{i=1}^5 \pi \frac{\Delta\omega_{mi}/2}{\tilde{\Delta}_{mi}^2 + (\Delta\omega_{mi}/2)^2} \frac{8(\Omega_{\text{d2}}g_i)^2}{\pi\Delta\omega_{mi}\tilde{\Delta}_q}, \quad (2.15)$$

which is a sum of Lorentzians, where the second term in the sum is the amplitude of the Lorentzian. The fitting function has fitting parameters  $\omega_{mi}$ ,  $\Delta\omega_{mi}$  and  $\Omega_{\text{d2}}g_i$ . As a result, the linewidth of a certain cavity mode can be seen in the width of the dips. The coupling of a mode to the drive antenna and to the qubit is reflected in the depth of the shift. In other words, the value of the frequency shift stands for the ability to create photon population, which interacts dispersively with the qubit.

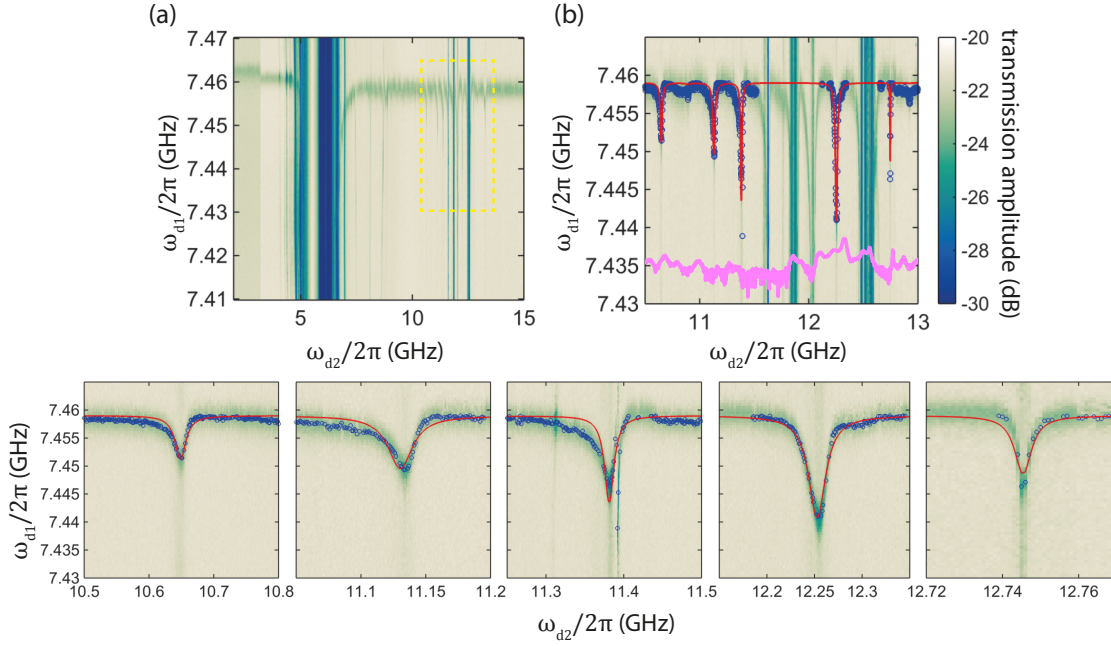


**Figure 2.22:** (a) AC Stark shifts of the BSB transition for a wide selective drive frequency range  $\omega_{d2}$  (cf. sample QMv3 1<sup>st</sup> in Tab.B.2 in the appendix). Yellow rectangle: closeup discussed in (b). The horizontal line at approximately 7.46 GHz is the BSB transition. At frequencies, where  $\omega_{d2}$  is swept over a cavity mode, this BSB transition frequency is shifted downward according to Eq. (2.15). The vertical dark lines indicate strongly driven transitions in first order, such as the cavity mode at 5.518 GHz or the first qubit transition at 6.234 GHz. (b) AC Stark shift contributions from higher cavity modes. The Lorentz dips give information about the mode bandwidths and coupling to the qubit. The fit (red line) is performed on extracted data points (blue dots). We limit the extracted data points to those modes, which have a negative dispersive shift. Pink line: Direct single tone transmission measurement of the cavity in dB as in Fig. 2.18. (c) Closeups of cavity modes fitted in (b).

For the fit, the drive amplitude  $\Omega_{d2}$  can be set to an arbitrary value. We only fit the modes, which have a dispersive shift towards the qubit. The other features, which are visible throughout the whole vertical range of  $\omega_{d1}$  are higher order transitions, such as other sidebands, or direct transitions, which are strongly driven. They are also detected by the dispersive readout. From the fit, we are able to extract the exact mode frequency  $\omega_{mi}$  and the mode linewidth  $\Delta\omega_{mi}$  (cf. Tab.2.5). By comparing these results to the single-tone transmission spectrum in this frequency range (cf. Fig. 2.18), the qubit assisted measurement of higher modes circumvents the limitations imposed by the VNA noise floor and the frequency range of the amplifiers. Hence, the individual modes can be resolved more accurately. In terms of the mode linewidths, however, one has to be careful to remain in a low drive power regime, where power broadening does not affect the linewidth. Therefore, the resulting  $Q$ -factors have to be taken as lower bounds. Another advantages of this type of measurement is that the impact of the modes on the

$\omega_m/2\pi$ (GHz)	$\Delta\omega_m/2\pi$ (MHz)	$Q_L$
10.648	20.2	525
11.113	22.9	486
11.138	14.6	781
12.253	21.7	564
12.745	5.3	2417

**Table 2.5:** Frequency, linewidth and quality factor of higher modes.

qubit is better resolved. This becomes important when dealing with transitions, where the AC Stark shift has to be taken into account.

If we examine the obtained frequencies  $\omega_{mi}$  of the qubit-cavity system and compare them with the simulated ones of the bare cavity system in Tab. 2.4, we observe that the measured modes are only present in a qubit-cavity system and non-existent in a bare cavity. In the frequency range from 10.5 GHz to 13 GHz, we obtain with the FEM simulation bare cavity modes at 11.39 GHz, 12.12 GHz and 12.77 GHz, whereas the triple-tone measurement reveals multiple modes in between these frequencies. Hence, the FEM simulation of a bare cavity is not sufficient to capture the full mode spectrum of a qubit-cavity system, but a triple-tone measurement is necessary. Due to the resulting qubit frequency shifts, it is crucial for the calibration of an experiment to take into account all relevant qubit-cavity modes. To this end, the triple-tone measurement is a useful tool to identify and quantify these modes.

### Sidebands

Another experiment based on the triple-tone setup is to investigate the red ( $\omega_r$ ) and the blue ( $\omega_b$ ) sideband in more detail according to the Hamiltonian given in Eq. (1.65). The first drive  $\omega_{RO}$  remains the resonator probe for dispersive readout, whereas the second and third drive,  $\omega_{d1}$  and  $\omega_{d2}$ , populate the qubit and the resonator mode. We fix one drive at a frequency close to the qubit frequency with a constant detuning  $\omega_{d1} = \omega_q \pm \delta_d$  of a few megahertz. This drive provides the qubit excitation. Typically, we sweep the other drive across the mode frequency to provide the mode excitation. If the requirement of  $\omega_{d1} + \omega_{d2} = \omega_b$  for the blue sideband is met, a transmission dip can be observed. For the drive close to the resonator frequency, this means  $\omega_{d2} = \omega_m \mp \delta_d$  has to be fulfilled. In the case of the red sideband, we have the difference frequency  $\omega_r = \omega_{d1} - \omega_{d2}$  and  $\omega_{d2} = \omega_m \pm \delta_d$  has to be satisfied. The detuning  $\delta_d$  has a practical reason, since without it, the sideband feature would coincide with either the qubit transition feature or the resonator peak, rendering it indistinguishable. The adjustment of the detuning is limited to a specific range, because the transition matrix element is proportional to  $1/\delta_d^2$  [81] and according to Fermi's golden rule, the transition rate is proportional to  $1/\delta_d^4$ .

The drive  $\omega_{d2}$  populates the mode with photons according to the Lorentzian cavity filter function. At a constant drive power, the closer the drive frequency comes to the resonance frequency, the higher is the excited population, leading to an increasingly divergent AC Stark shift of the qubit. To compensate for this, we adjust the drive power with the inverse of the cavity filter function to maintain a constant population in the resonator mode [cf. Fig. 2.23 (d)].

In Fig. 2.23 (a)-(c), we present measurements of the sidebands of the qubit and the TE101 mode and the TE201 mode, respectively [123]. The bare frequencies are  $\omega_q/2\pi \simeq 7.60$  GHz,  $\omega_{101}/2\pi \simeq 5.606$  GHz and  $\omega_{201}/2\pi \simeq 8.904$  GHz. The almost degenerate "twin" mode of the TE201 is at  $\omega_{102}/2\pi \simeq 8.944$  GHz. In Fig. 2.23 (a), we observe both the red and the blue sideband as diagonal lines in the graph, since they correspond to the difference and sum of the qubit and mode frequency, respectively [cf. Eq. (1.56)]. To calculate the frequency of the blue sideband, we add up the values of  $\omega_{d1}$  and  $\omega_{d2}$  at an arbitrary point on the diagonal line and obtain  $\omega'_b = 5.578$  GHz + 7.591 GHz = 13.169 GHz. We notice that this value is lower than the bare sum  $\omega_q + \omega_{101}$ . The reason for this difference is the AC Stark shift of the qubit, which we account to  $20 \times \chi'$ . In other words, the TE101 mode is populated with a constant amount of approximately 20 photons on average, and we obtain  $\omega_b = \omega_q + \omega_{101} + 20\chi'$ . In this calculation, we neglect the Kerr shift of the mode [cf. Eq. (1.59)], which is on the order of tens of kilohertz. For the red sideband, we can follow the same procedure and obtain  $\omega'_r = 1.960$  GHz.

The blue sideband of the qubit and the TE201 mode is shown in Fig. 2.23 (c). Here, the mode photon population is significantly lower, because the linewidth of this mode is about 30 times smaller than in the case of the TE101 mode. This makes it difficult to maintain a constant photon population due to the high power, which is necessary to populate the mode with photons [cf. Eq. (1.16)]. Furthermore, the degenerate mode with a large linewidth is close by and requires to be considered in the cavity filter function. Thus, the power adjustment function becomes more complex and the system becomes more susceptible to small drive fluctuations, which lead to shifted frequencies. As a workaround, it is easier to keep the drive power low and accept that the higher order sideband transitions are less visible. The red sideband is not visible in this scenario, because it needs an excitation already present in the system ( $|g1\rangle \Leftrightarrow |e0\rangle$ ), which is not fulfilled for such low drive powers. Close to the mode, the qubit frequency is inevitably AC Stark shifted as it can be seen in the data. Moreover, it is shifted for frequencies higher than  $\omega_{201}$  due to the presence of the TE102 mode. Nevertheless, we can observe the blue sideband of the qubit and the TE201 mode<sup>18</sup>.

<sup>18</sup>A sideband of the qubit with the TE102 mode is not observed, since the the qubit coupling to this mode is lower by one order of magnitude as compared to the TE201 or TE101 mode due to the position of the qubit chip.

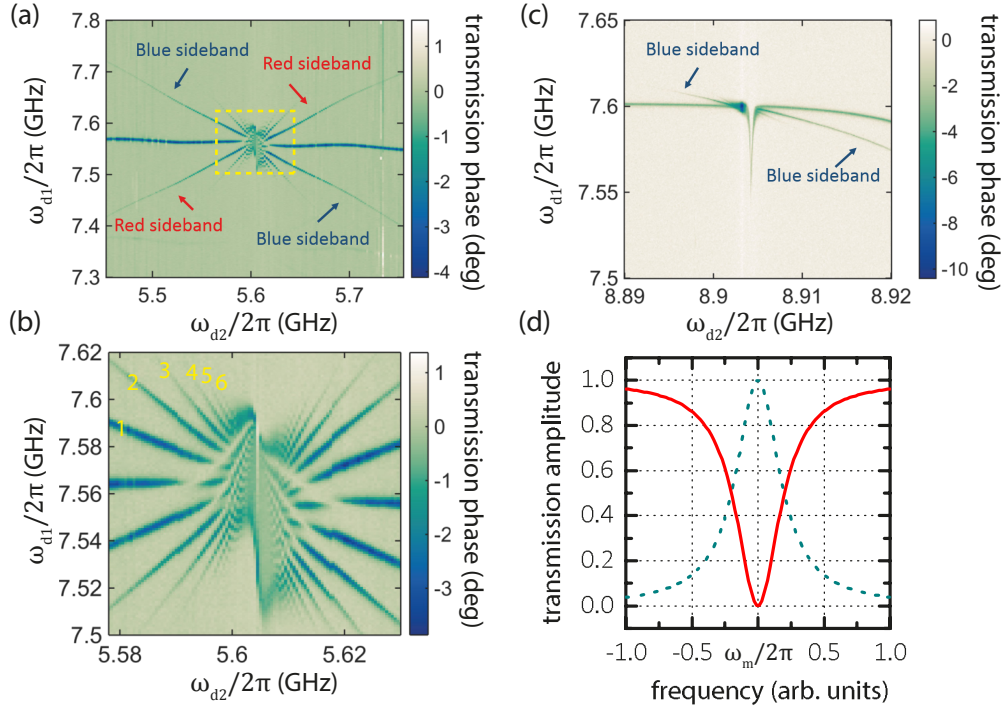


**Figure 2.23:** Triple-tone spectroscopy of sideband transitions for (a) TE101 mode and (c) TE201 mode (cf. sample QMv3 1<sup>st</sup> in Tab. B.2 in the appendix). On the vertical axis, we sweep the qubit drive frequency ( $\omega_{d1}$ ) to excite the qubit at the qubit transition frequency. On the horizontal axis, we sweep the mode drive frequency ( $\omega_{d2}$ ) across the corresponding mode frequency to populate the mode with photons. We record the transmission phase in a dispersive readout scheme. If the sum or the difference of both drives equals a sideband transition, we observe a dip in the transmission phase. (b) Blow-up of the TE101 mode spectroscopy as marked by the yellow rectangle in (a). Sidebands up to the 6th order are visible. (d) Power adjustment function (solid red), which is the inverse of the cavity filter function (dashed turquoise). To prevent additional AC Stark shifts, the drive power is adjusted to maintain the same amount of photons during the frequency sweeps over the resonance peaks.

## 2.3 Time domain measurements

The dynamics of a qubit can only be revealed with a time resolved measurement setup [16, 120]. Based on Sec. 1.4, one has to be able to rotate the qubit on the Bloch sphere in a controlled manner. After that, a readout has to be performed, which is similar to taking a snapshot of the system right after preparation. Both the preparation and the readout require pulsed microwave signals with nanosecond accuracy. In the following, we introduce the pulse generation setup and basic pulse protocols for qubit measurements. Then, we discuss pulse shaping techniques and the effect of spectrally broad pulses on a transmon qubit. We also include qubit phase control with  $I$  and  $Q$  quadratures.

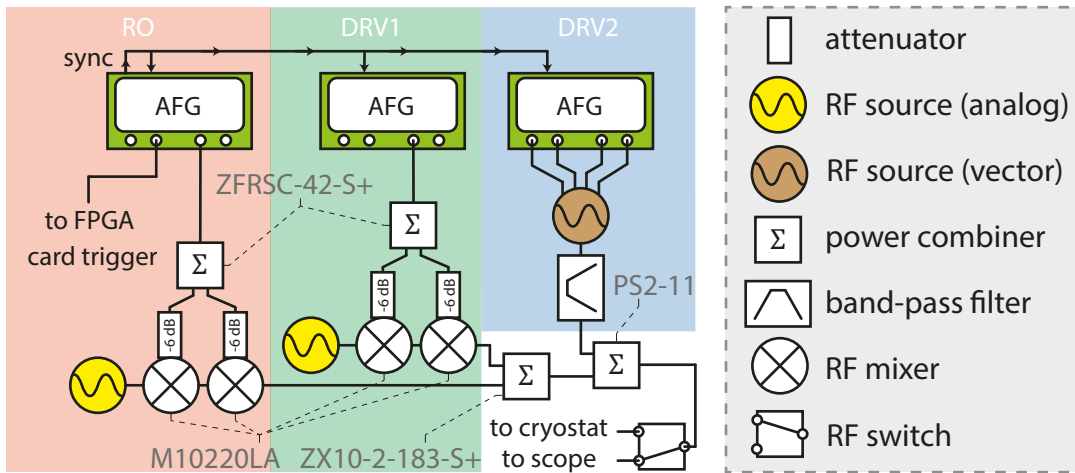


**Figure 2.24:** Pulse generation setup for time domain measurements. This setup has the flexibility of using a standard analog RF source or a vector modulated RF source for  $IQ$  drive pulse control. The band-pass filter in front of the RF vector source is interchangeable depending on the drive frequency requirements. An RF switch is implemented for quick validation of the pulse generation on the oscilloscope.

### 2.3.1 Pulse generation setup

The pulse envelope is generated by an arbitrary function generator (AFG)<sup>19</sup> with a sampling rate of 2.5 GSa/s, 14bit vertical resolution and a 500 MHz bandwidth. A continuous microwave signal at the desired gigahertz frequency is sent from an analog microwave source to a chain of two RF mixers, which are connected to the AFG and, hence, modulate the pulse envelope onto the microwave signal (cf. Fig. 2.24). Two RF mixers in series are necessary to provide a sufficient on/off ratio. This scheme is scalable to multiple pulsed microwave drives, which are then combined with power combiners<sup>20</sup>. The minimum setup consists of a pulsed readout at the cavity frequency  $\omega_{RO}$  and one pulsed drive at the qubit transition frequency  $\omega_q$ . We extend this setup with a vector modulated source<sup>21</sup> for qubit phase control. In this case, the two channels of the AFG are directly connected to the differential wideband  $IQ$  inputs of the vector source, which takes care of the pulse modulation.

The recording of the measurement signal is only briefly discussed here, because it is the same setup used in Ref. [120]. We use a field programmable gate array (FPGA) card<sup>22</sup> with a sampling rate of 250 MHz for digitizing the measurement signals. Since the readout signal oscillates at a gigahertz frequency, it is downconverted with an  $IQ$  mixer to 62.5 MHz in order to fit the sampling rate of the FPGA card. This intermediate

<sup>19</sup>Agilent/Keysight 81160A

<sup>20</sup>Minicircuit ZX10-2-183-S+ and MCLI PS2-11

<sup>21</sup>Agilent E8267D PSG with differential wideband  $IQ$  option (016)

<sup>22</sup>X5-RX from Innovative Integration

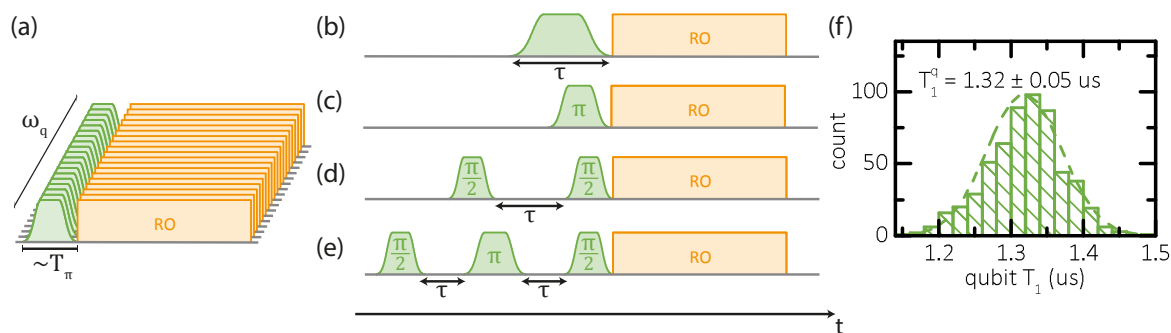


**Figure 2.25:** Basic pulse protocols: (a) Pulsed spectroscopy with sweep of qubit drive frequency  $\omega_q$ . (b) Driven Rabi oscillations. (c) Direct  $T_1$  measurement. (d) Ramsey  $T_2$  measurement. (e) Spin echo  $T_2$  measurement. The qubit preparation pulse is colored in green, the resonator readout pulse in orange. (f) Histogram of qubit  $T_1$  measured by performing the  $5 \cdot 10^5$  times averaged protocol of (c) approximately 1000 times in a row (cf. sample QMv3 2<sup>nd</sup> in Tab. B.2 in the appendix).

frequency (IF) is chosen to fulfill the Nyquist-Shannon sampling theorem [125, 126]. To synchronize the microwave drive pulses and the data acquisition, the FPGA card is triggered by one of the AFGs. Each measurement is repeated  $5 \cdot 10^5$  times and the recorded IF signal is streamed from the FPGA card to the computer. A post processing step is performed on the computer using LabView, where the data is averaged and another demodulation to DC is applied.

### 2.3.2 Basic pulse protocols and automatic tune-up

With a time resolved measurement setup, one is able to perform all the measurements, which can be done with the VNA, however, in a pulsed manner. The temporal separation of the preparation and the readout has the advantage, that the probe signal does not disturb the qubit by, e.g., AC Stark shifting it. In Fig. 2.25 (a), the protocol for such a pulsed spectroscopy is shown. The drive pulse shape is fixed and the frequency of the drive carrier is swept. In practice, the preparation pulse only needs to be close to a  $\pi$ -pulse in order to excite the qubit and give a measurable response different from the ground state.

By resonantly driving the qubit, one can induce Rabi oscillations as described in Eq. (1.63). To this end, the length  $\tau$  of the drive pulse is increased for each sweep [cf. Fig. 2.25 (b)]. With this method, we determine the  $\pi$ -pulse length  $T_\pi$ . Depending on the drive power  $P_d$ , the  $\pi$ -pulse length can be longer for low  $P_d$  or shorter for high  $P_d$ .

The knowledge of  $T_\pi$  paves the way to perform energy relaxation measurements by pulsing the qubit to  $|e\rangle$  and record the decay directly during the readout pulse [cf. Fig. 2.25 (c)]. This decay constant describes the energy relaxation time  $T_1$ . Since energy

relaxation is a statistical process, we typically perform statistics on this parameter. An exemplary histogram of the normal distributed qubit decay time is shown in Fig. 2.25 (f).

The qubit decoherence time  $T_2$  is typically measured with either a Ramsey or a spin echo sequence [cf. Fig. 2.25 (d) and Fig. 2.25 (e)]. Both are based on letting the qubit rotate freely in the equatorial plane, however, the spin echo sequence contains an intermediate refocusing  $\pi$ -pulse to mask out low frequency noise [53]. For the Ramsey sequence, the qubit is pulsed with a  $\pi/2$ -pulse into the equatorial plane for free precession around the  $z$ -axis for a waiting time  $\tau$ . In the end, the qubit is rotated back onto the  $z$ -axis with a second  $\pi/2$ -pulse and the readout is performed.

All above mentioned protocols are based on a clean preparation of the qubit via a  $\pi$ - or  $\pi/2$ -pulse<sup>23</sup>. During the course of this work, an automated fitting procedure for finding the optimal  $T_\pi$  has been implemented as a pre-processing step in the LabView measurement program (cf. Fig. 2.26). Based on initial estimations of  $\omega_q$  and  $T_\pi$ , the software is able to find the correct qubit frequency and  $\pi$ -pulse length for a given drive power. By doing pulsed spectroscopy and taking the transmission minimum, we get the qubit frequency. For the  $\pi$ -pulse length, a Rabi oscillation measurement is performed and the data is fitted with a damped sine fitting function. The first oscillation peak or dip then is the correct  $T_\pi$ . This tune-up procedure can be performed before each measurement and enhances the subsequent qubit preparation precision.

If the specific goal is to obtain two consecutive  $\pi$ -pulses at different transition frequencies, we begin with calibrating the  $\pi$ -pulse for the first transition. Then, the same pre-measurements are repeated for the second transition, however with the first optimized  $\pi$ -pulse preceding.

### 2.3.3 Pulse shaping

The shape of the pulse envelopes is of substantial importance for the fidelity of the qubit preparation. We can understand this, if we Fourier transform (FT) the pulse shape  $s(t)$  from time domain to frequency domain [127].

$$S(\omega) = \int_{-\infty}^{+\infty} s(t)e^{-i\omega t} dt = \mathcal{F}\{s(t)\} \quad (2.16)$$

$$s(t) = \frac{1}{2\pi} \int_{-\infty}^{+\infty} S(\omega)e^{-i\omega t} d\omega = \mathcal{F}^{-1}\{S(\omega)\} \quad (2.17)$$

The Fourier transformation is equal to expressing the shape  $s(t)$  with an infinite series of cosine and sine functions of certain frequencies. Taking a rectangular sharp pulse

<sup>23</sup>For calibrating the  $\pi/2$ -pulse, it is convenient to use two equal pulses in series and sweep the length of both pulses simultaneously. At a certain pulse length, where the qubit is prepared in  $|e\rangle$ , both pulses have contributed a  $\pi/2$  rotation. Especially, when using non-rectangular pulse shapes, this method is far more accurate than estimating the  $\pi/2$ -pulse length from the first quarter period of a Rabi oscillation pattern.

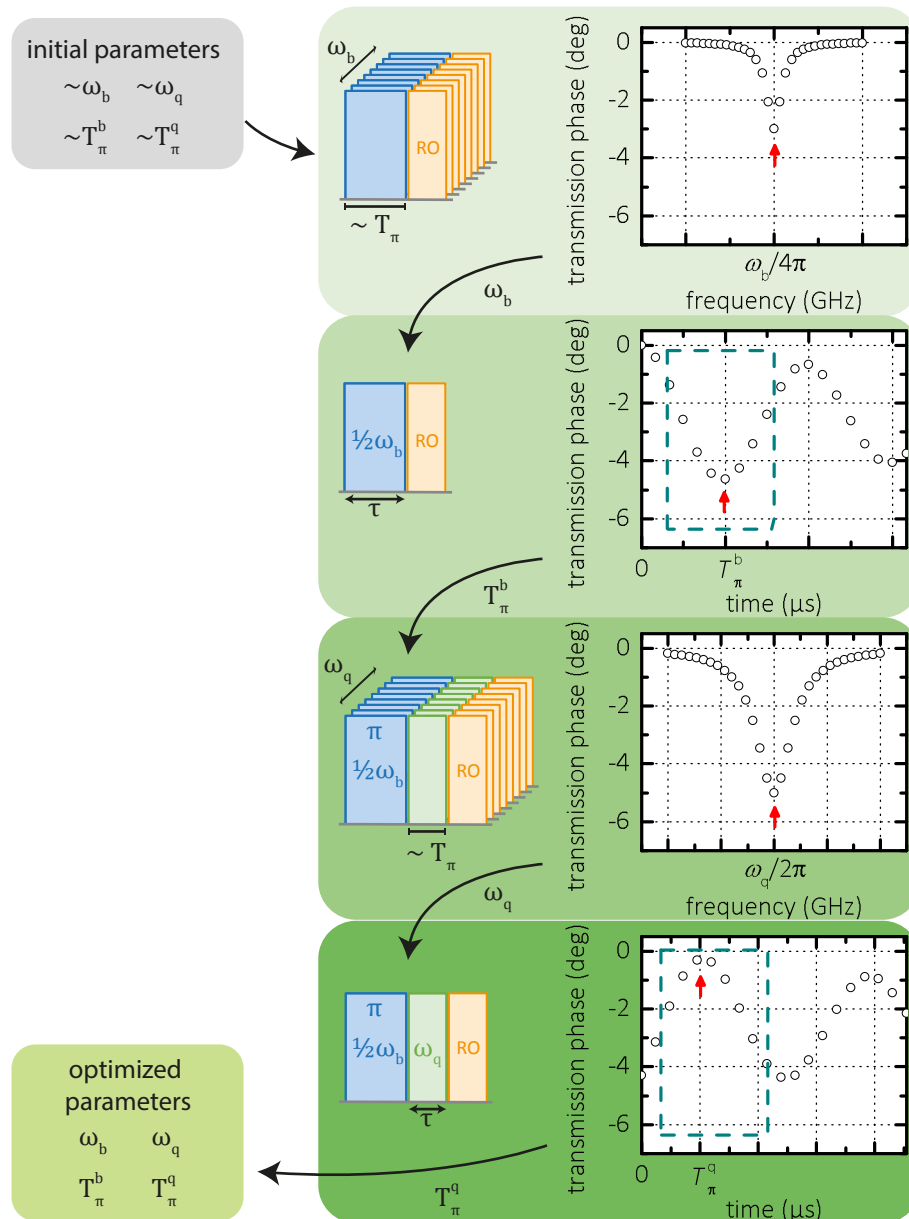


**Figure 2.26:** Tune-up procedure for  $\pi$ -pulse optimization. The pulse scheme and the schematic measurement outcome are shown in each panel. Red arrows mark the local extrema found by the optimization routine. For finding the optimized  $T_\pi$ , the extremum search range is limited to the first oscillation period (cyan dashed rectangle). In this scenario, we optimize a  $\pi$ -pulse at the transition frequency  $\omega_b$  and another  $\pi$ -pulse at the transition frequency  $\omega_q$ . The final measurement sequence (cf. Sec. 3.1.2) requires these two  $\pi$ -pulses to be consecutive with the  $\pi$ -pulse at  $\omega_b$  in front. Hence, we first optimize the  $\pi$ -pulse at  $\omega_b$  and then the one at  $\omega_q$ .

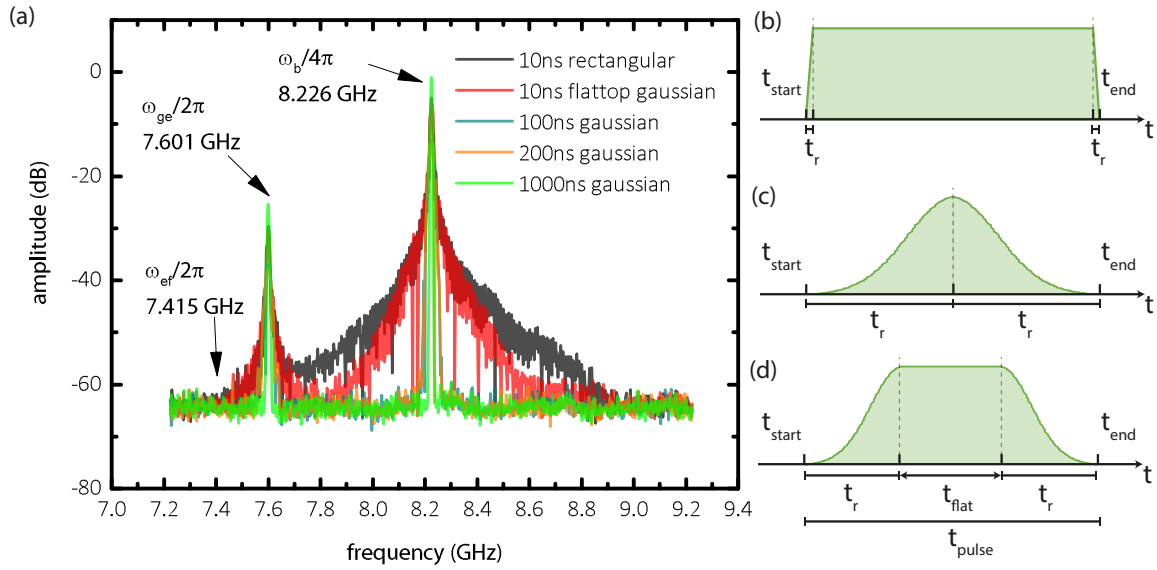


**Figure 2.27:** (a) Spectrum analysis of typical pulse shapes used in the experiment. The pulse shapes differ in their ramp up time  $t_r$ . We apply one pulse at the frequency  $\omega_b/4\pi$  and one at  $\omega_q/2\pi$  with different drive power. The frequencies are matched to sample QMv3 1<sup>st</sup> in Tab. B.2 in the appendix. Strong parasitic driving of the first and second qubit transition is visible for 10 ns pulses. (b) Rectangular pulse shape. (c) Gaussian pulse shape. (d) Gaussian flattop pulse shape as a hybrid of the former two. The temporal resolution of the AFG is 2.5 GSa/s and hence, the minimal rise time is about 1 ns.

in time domain, an infinite number of different frequency components is necessary to model the sharp edge. Hence, the frequency spectrum of the pulse envelope is very broad. Especially when working with a transmon qubit with limited anharmonicity, the spectral width of the pulses has to be considered. Therefore, we analyze different pulse shapes with a spectrum analyzer<sup>24</sup>. A spectrum analyzer performs a discrete FT of the measured  $s(t)$ .

One important pulse shape is a Gaussian shaped pulse  $g(t)$ , which maintains its functional form when Fourier transformed.

$$g(t) = \exp\left(-\frac{t^2}{2\sigma^2}\right) \quad (2.18)$$

$$G(\omega) = \mathcal{F}\{g(t)\} = \frac{1}{\sigma\sqrt{2\pi}} \exp\left(-\frac{\sigma^2\omega^2}{2}\right) \quad (2.19)$$

Hence, it is convenient to use such kind of pulses. With regard to the pulse protocols, however, the drive amplitude is proportional to the area under the pulse and defines how far the qubit is rotated on the Bloch sphere. When using rectangular shaped pulses [cf. Fig. 2.27 (b)], the area has a favorable linear dependence on the pulse length. When using a Gaussian shaped pulse [cf. Fig. 2.27 (c)], the area does not increase linearly

<sup>24</sup>Rohde & Schwarz FSP7

when the length of the pulse is adjusted. Moreover, the spectral width of the pulse changes as well. In order to circumvent this problem, we use flattop Gaussian pulses  $g_f(t)$  with a fixed Gaussian edge, but a flat top [cf. Fig. 2.27 (d)]. The pulse shape is piecewise defined as

$$g_f(t) = \begin{cases} 0 & 0 \leq t < t_{\text{start}} \\ \exp\left(-\frac{(t/t_r-1)^2}{2\sigma^2}\right) & t_{\text{start}} \leq t < t_{\text{start}} + t_r \\ 1 & t_{\text{start}} + t_r \leq t < t_{\text{start}} + t_r + t_{\text{flat}} \\ \exp\left(-\frac{(t/t_r)^2}{2\sigma^2}\right) & t_{\text{start}} + t_r + t_{\text{flat}} \leq t < t_{\text{start}} + t_r + t_{\text{flat}} + t_r \\ 0 & t_{\text{start}} + t_r + t_{\text{flat}} + t_r \leq t < t_{\text{end}}. \end{cases}$$

As a result, the area can be scaled linearly with the pulse length with a slight offset due to the Gaussian edges. Furthermore, the spectral width is independent from the pulse length.

### 2.3.4 Qubit phase control

A microwave signal with amplitude  $A$  and phase  $\varphi$  can be expressed in terms of the in-phase and quadrature components  $I$  and  $Q$

$$I = A \cos(\varphi) \quad (2.20)$$

$$Q = A \sin(\varphi). \quad (2.21)$$

Typically, they are represented in a 2D plot, the  $IQ$  plane [cf. Fig. 2.28 (a)]. We can use  $I$  and  $Q$  to modulate our microwave drives in phase or amplitude [128]. According to Eq. (1.63), the phase  $\varphi_d$  of our drive signal translates into the phase angle  $\varphi$  of the qubit vector. By setting a certain relative phase<sup>25</sup>, we are able to rotate the qubit about different axes on the Bloch sphere. The phase and the amplitude are given as

$$A = \sqrt{I^2 + Q^2} \quad (2.22)$$

$$\varphi = \arctan\left(\frac{Q}{I}\right). \quad (2.23)$$

Using an  $IQ$  mixer, where the carrier of the drive is supplied at the local oscillator port, we can modulate the drive with pulsed signals at the  $I$  and the  $Q$  port<sup>26</sup> [cf. Fig. 2.28 (b)]. By adjusting the ratio, while keeping the amplitude  $A$  constant, we are able to change the phase of the drive during the pulse. We plot several pulse sequence

<sup>25</sup>We note that  $\varphi_d$  refers to the relative phase between different pulses in the same pulse sequence generated by a single RF source. The global phase is of minor relevance in this context.

<sup>26</sup>Typically, we add a second RF mixer behind the  $IQ$  mixer for gating the  $IQ$ -modulated pulses. This increases the on/off ratio for the drive and reduces unwanted population during the off-time.

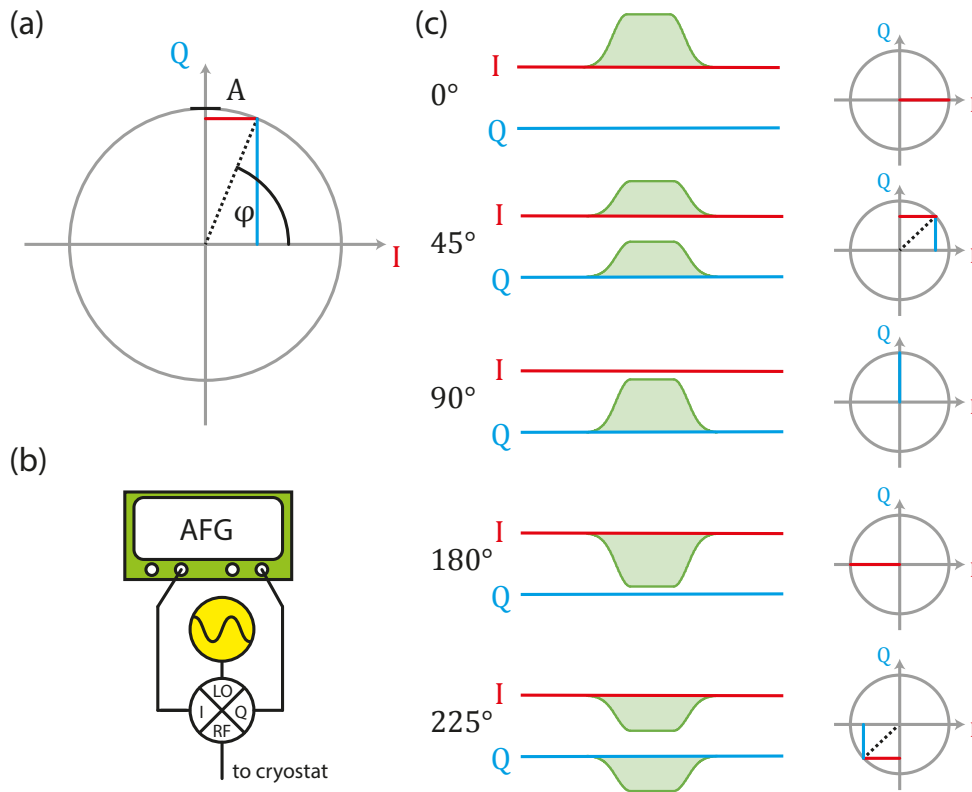


**Figure 2.28:** (a)  $IQ$  plane with amplitude  $A$ , phase  $\varphi$  and  $I$  and  $Q$ . (b) Setup scheme for phase controlled pulses with an external  $IQ$  mixer. The two channels of the AFG have to be set to coupling mode in order to properly synchronize the pulses. (c) Exemplary pulse sequences for setting phase angles during a pulse.

examples for different phase angles in Fig. 2.28 (c).

With this type of qubit control, we are able to perform measurements not only on the naturally given  $z$ -axis, but can also obtain information about  $\langle \hat{\sigma}_x \rangle$  and  $\langle \hat{\sigma}_y \rangle$  by rotating the qubit onto our preferred measurement axis with  $\pi/2$ -pulses and a corresponding phase of  $0^\circ$  or  $90^\circ$ . This opens up the possibility to perform quantum state tomography [129], and as a subsequent step, quantum process tomography [73].

### 2.3.5 IQ-mixer calibration

For qubit experiments with phase control, it is important to keep the amplitude of the signal constant over a wide range of given phases according to Eq. (2.23). This means, the imperfections of a commercial  $IQ$  mixer have to be calibrated. Typically a slight imbalance of the  $I$  and the  $Q$  channel causes the amplitude to vary for certain phase angles. The solution is either to use a calibrated, but expensive, vector modulated

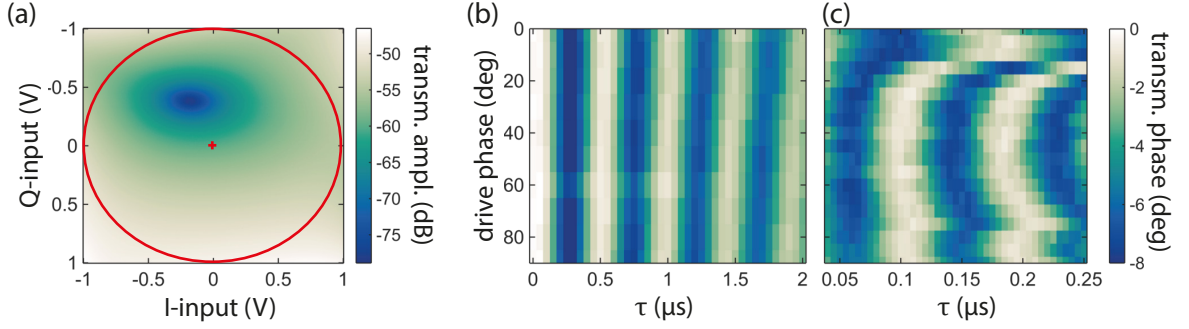


**Figure 2.29:** (a) Data for calibrating the  $IQ$  mixer at  $\omega_d/2\pi = 6.2155$  GHz. The red circle is a contour of  $I$  and  $Q$  pairs with constant amplitude  $A$  in the ideal case. The origin at  $I, Q = 0$  is marked with a red cross. (b) and (c) Driven qubit Rabi oscillations at  $\omega_d/2\pi = 6.234$  GHz (cf. sample QMv3 2<sup>nd</sup> in Tab. B.2 in the appendix) for a drive phase  $\varphi_d$  from  $0^\circ$  to  $90^\circ$  using (b) a PSG vector RF source and (c) an uncalibrated  $IQ$  mixer connected to an analog RF source.

microwave source<sup>27</sup> or to calibrate an external  $IQ$  mixer<sup>28</sup> and use it together with an analog microwave source.

For calibration, the  $IQ$  mixer is connected to the AFG as depicted in Fig. 2.28 (b). The signal from the RF port of the  $IQ$  mixer is directly routed to the receiver port of the VNA, without passing through the cryostat. Due to the fact that the  $I$  and  $Q$  channel of the  $IQ$  mixer are not independent, we have to perform a 2D calibration [130] [cf. Fig. 2.29 (a)]. Using two channels of the AFG, we modulate  $I$  and  $Q$  from  $-1$  V to  $1$  V onto a carrier RF signal with  $\omega_d$  and measure the RF signal level with the VNA. The AFG sets a constant DC voltage signal at the  $I$  and  $Q$  channel in the limit of the allowed input voltages. For each voltage value at the  $I$  input, the voltage at the  $Q$  input is swept. We note that this calibration procedure sets the phase and amplitude relations only for a single frequency. Nevertheless, in the case of fixed-frequency qubits as used in this thesis, a single calibration per sample is sufficient.

The inversion of this 2D plane is nontrivial, because monotony is not given for the whole calibration range. As workaround, one can shift the global minimum of the calibration data to the origin of the  $IQ$ -plane by applying constant offset voltages on the  $I$ - and  $Q$ -channel. Then, we can correct analytically for the remaining ellipticity to match the ideal  $IQ$ -plane circle. However, for most applications, only a set of discrete phase angles is necessary, which is easy to calibrate. For benchmarking our calibration, we have the option to use Rabi oscillations of a qubit, which acts as a very sensitive power detector according to Eq. (1.63). We perform the same Rabi oscillation pulse sequence for various phase angles. In case of a successful calibration, the Rabi frequency stays the same for all phase angles.

<sup>27</sup>Agilent E8267D PSG with differential wideband  $IQ$  option (016)

<sup>28</sup>Marki MLIQ-0416 Microlithic Double-Balanced I/Q Mixer

Qubit Rabi oscillations using an uncalibrated  $IQ$  mixer are shown in Fig. 2.29 (c). The imbalance between  $I$  and  $Q$  is clearly visible due to a significant change in the Rabi frequency. This demonstrates a non-constant drive amplitude over the range of drive phases. In Fig. 2.29 (b) we show data for a calibrated PSG vector RF source. After the first oscillation period, we notice a slight deviation in Rabi frequency due to a slightly imperfect internal power calibration of the PSG. However, for typical qubit experiments, only a pulse length smaller than  $T_\pi$  is required. For the following tomography experiments, we conveniently use the calibrated PSG vector RF source.

### 2.3.6 Quantum state tomography

In order to fully characterize a quantum state, one has to know the density matrix  $\hat{\rho}$  [cf. Eq. (1.32)]. For a single qubit, this means that all three components of the Bloch vector are known. By using the dispersive readout scheme, we only weakly measure the  $z$ -component  $\langle \hat{\sigma}_z \rangle^2$  and the other two components remain unknown. In the picture of the Bloch sphere, it is easy to understand that we need to rotate the qubit vector by a set of certain rotations to gain knowledge of the other two components. This procedure is called quantum state tomography (QST), because, in an intuitive picture, the quantum state has to be prepared multiple times and snapshots from different perspectives have to be taken to obtain the full state. The  $x$ - and  $y$ -components are measured by rotating the prepared state  $|\Psi\rangle$  with the following rotation matrices [131].

$$\begin{aligned}
 R_x(\theta) &\equiv e^{-i\hat{\sigma}_x\theta/2} = \cos\left(\frac{\theta}{2}\right) \mathbb{1} - i \sin\left(\frac{\theta}{2}\right) \hat{\sigma}_x = \begin{pmatrix} \cos(\theta/2) & -i \sin(\theta/2) \\ -i \sin(\theta/2) & \cos(\theta/2) \end{pmatrix} \\
 R_y(\theta) &\equiv e^{-i\hat{\sigma}_y\theta/2} = \cos\left(\frac{\theta}{2}\right) \mathbb{1} - i \sin\left(\frac{\theta}{2}\right) \hat{\sigma}_y = \begin{pmatrix} \cos(\theta/2) & -\sin(\theta/2) \\ \sin(\theta/2) & \cos(\theta/2) \end{pmatrix} \\
 R_z(\theta) &\equiv e^{-i\hat{\sigma}_z\theta/2} = \cos\left(\frac{\theta}{2}\right) \mathbb{1} - i \sin\left(\frac{\theta}{2}\right) \hat{\sigma}_z = \begin{pmatrix} \exp(-i\theta/2) & 0 \\ 0 & \exp(i\theta/2) \end{pmatrix}
 \end{aligned}$$

The  $z$ -axis is the natural quantization and measurement axis. To project the  $x$ -component onto the  $z$ -axis for measurement, we have to apply  $R_y(\pi/2)$ . The same is valid for the  $y$ -component with  $R_x(\pi/2)$ . In experiment, these operations are performed by applying a  $\pi/2$ -pulse with  $\varphi_d = 0^\circ$  or  $90^\circ$ , respectively. This drive phase is adjusted by choosing the  $I$ - and  $Q$ -component of the pulse envelope in a suitable manner [cf. Fig. 2.28 (c)]. The pulse sequences for projective measurements of an arbitrary state  $|\Psi\rangle$  are shown in Fig. 2.30.

For calculating the density matrix, we assume in the following that the dispersive readout is based on a linear relation between the measured dispersive readout mode phase shift  $\varphi$  and the probability of the qubit being in the  $|e\rangle$ -state [64]. Then, we can

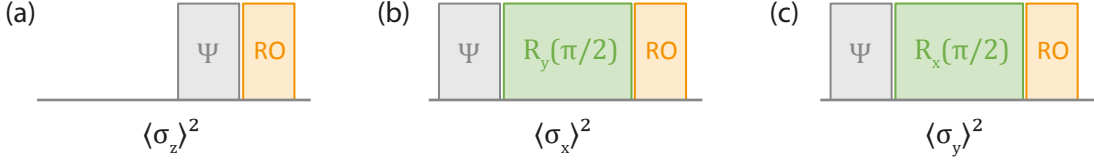


**Figure 2.30:** Schematic pulse protocols for QST. A state  $|\Psi\rangle$  is prepared and then measured in the  $z$ -,  $x$ - and  $y$ -direction of the Bloch sphere to obtain  $\langle\hat{\sigma}_z\rangle^2$ ,  $\langle\hat{\sigma}_x\rangle^2$  and  $\langle\hat{\sigma}_y\rangle^2$ . For this kind of measurement, an  $IQ$ -modulated setup (cf. Fig. 2.24) is necessary in order to control the qubit phase.

express the populations of the qubit as

$$p_g = \frac{\varphi_g - \varphi_{\text{RO}}}{\varphi_g - \varphi_e}, \quad p_e = \frac{\varphi_{\text{RO}} - \varphi_e}{\varphi_g - \varphi_e} \quad (2.24)$$

where  $\varphi_g$  and  $\varphi_e$  are the readout phase for the ground state and the excited state, respectively, and  $\varphi_{\text{RO}}$  is the measured phase with  $\varphi_e \leq \varphi_{\text{RO}} \leq \varphi_g$ . Here, we assume that  $\varphi_e < \varphi_g$ , which eventually depends on the sign of the dispersive shift and the selected readout frequency (cf. Fig. 2.19). In experiment, we choose  $\varphi_g = 0$  and calibrate  $\varphi_e$  with a  $\pi$ -pulse. Typically, we neglect decoherence effects during  $T_\pi$ , since the effects on the final QST fidelity are on the order of  $<1\%$  for typical  $\pi$ -pulse times and  $T_q \simeq 1.3 \mu\text{s}$ . Depending on the direction of the projective measurement, the measured  $\varphi_{\text{RO}}$  is either  $\varphi_z$ ,  $\varphi_y$  or  $\varphi_x$ . Finally, we reconstruct the density matrix as

$$\hat{\rho} = \frac{1}{\varphi_g - \varphi_e} \begin{pmatrix} \varphi_z - \varphi_e & \bar{\varphi} - \varphi_x - i(\bar{\varphi} - \varphi_y) \\ \bar{\varphi} - \varphi_x + i(\bar{\varphi} - \varphi_y) & \varphi_g - \varphi_z \end{pmatrix}. \quad (2.25)$$

where  $\bar{\varphi} = (\varphi_g + \varphi_e)/2$  is the mean phase. Typically, the measured phases  $\varphi_x$ ,  $\varphi_y$  and  $\varphi_z$  are average values from a large set of equal measurements. In case of an unphysical reconstructed density matrix, e.g.  $\text{Tr}\hat{\rho}^2 > 1$ , one has to apply a maximum likelihood estimation (MLE) in order to obtain the physical  $\hat{\rho}$  (cf. App. D). In Fig. 2.31, we present reconstructed density matrices for three distinct qubit states  $|e\rangle$ ,  $|+\rangle$  and  $|-\rangle$ . Here,  $|+\rangle$  and  $|-\rangle$  denote the superpositions in  $x$ - and  $y$ -direction, respectively,

$$|+\rangle = \frac{1}{\sqrt{2}}(|g\rangle + |e\rangle) \quad |-\rangle = \frac{1}{\sqrt{2}}(|g\rangle + i|e\rangle). \quad (2.26)$$

Each density matrix consists of 50 separate measurements of  $\varphi_z$ ,  $\varphi_y$  or  $\varphi_x$ , which are performed in a cyclical sequence. To determine the deviation of the experimental results from the ideal theoretical results, the fidelity  $F$  is used, which is defined as  $F(\hat{\rho}_t, \hat{\rho}) = \text{Tr} \sqrt{\sqrt{\hat{\rho}} \hat{\rho}_t \sqrt{\hat{\rho}}}$ . For all three states, we achieve fidelities close to 1.

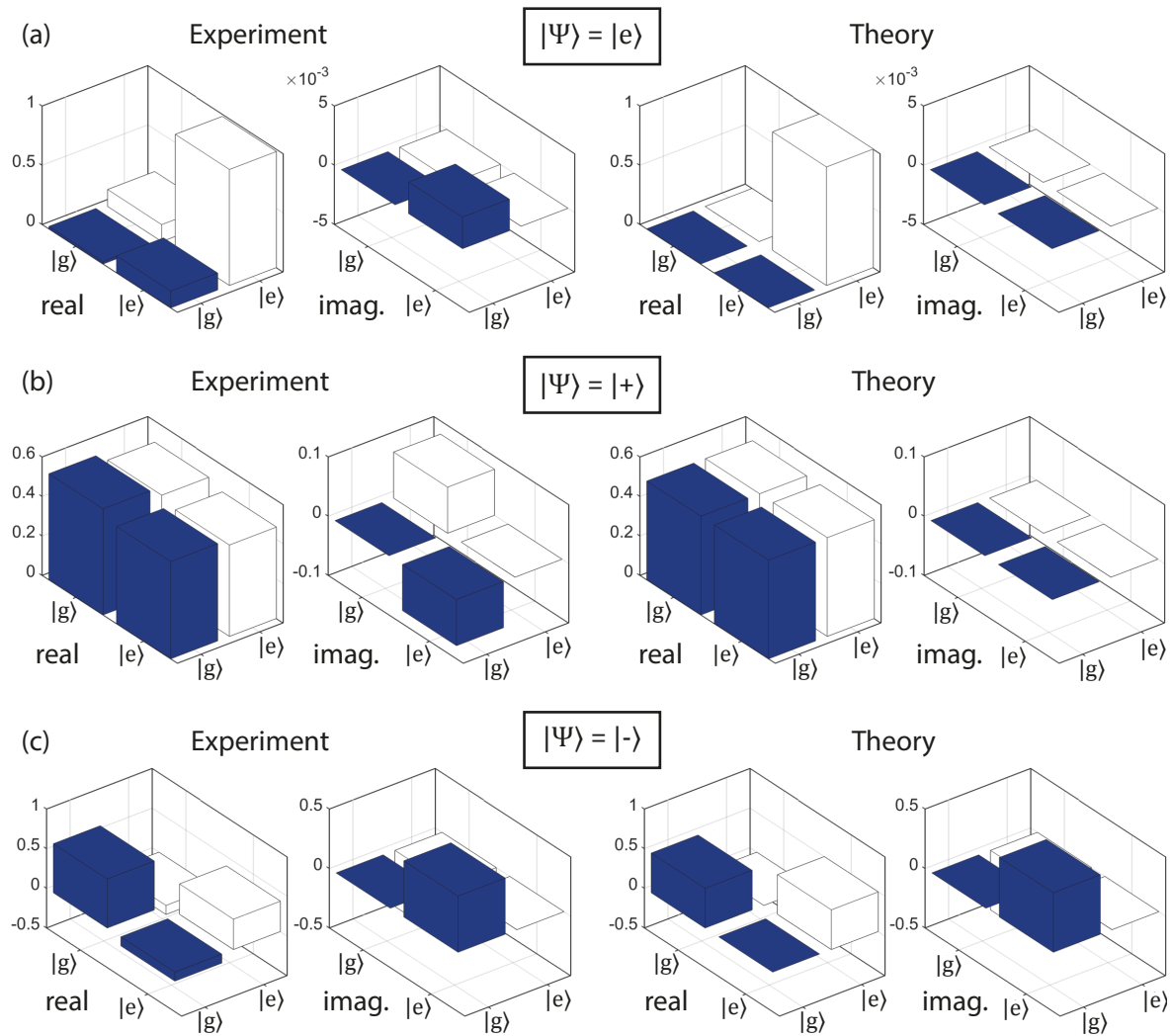


**Figure 2.31:** Measured QST for three distinct qubit states (cf. sample QMv3 2<sup>nd</sup> in Tab. B.2 in the appendix). We compare the density matrix from experimental data with the theoretically expected density matrix. The color code is for better visibility of the single matrix elements. The QST fidelities are  $F_{|e\rangle} = 98.21\%$ ,  $F_{|+\rangle} = 99.62\%$  and  $F_{|-\rangle} = 99.16\%$ .

### 2.3.7 Quantum process tomography

We give a short introduction to quantum process tomography (QPT), which is a useful tool to quantify the fidelity of quantum operations. Here, we will first derive the quantum process matrix  $\hat{\chi}$  for a Hilbert space of dimension  $d$  and, then, limit the discussion to  $d = 2$  for the single qubit case. A more general review on QPT can be found in Refs. [73, 132].

The aim of QPT is to determine the effect of an arbitrary quantum process  $\mathcal{E}$  which can be regarded as a transition from an initial state  $\hat{\rho}$  to the final state  $\hat{\rho}'$ :

$$\mathcal{E}(\hat{\rho}) = \hat{\rho}' \quad (2.27)$$

If  $\mathcal{E}$  represents a physically valid process, a Kraus representation [133] for the quantum process can be found, which means that there are trace-preserving operators  $\hat{E}_i$  such that the process can be decomposed into an operator sum [132]

$$\mathcal{E}(\hat{\rho}) = \sum_i \hat{E}_i \hat{\rho} \hat{E}_i^\dagger. \quad (2.28)$$

Typically, for an arbitrary process, we lack detailed information about the Kraus operators  $\hat{E}_i$ . Nevertheless, we can choose a fixed operator basis  $\{\hat{B}_m\}$  and rewrite  $\mathcal{E}(\hat{\rho})$  into

$$\mathcal{E}(\hat{\rho}) = \sum_{m,n} \hat{B}_m \hat{\rho} \hat{B}_n^\dagger \chi_{mn} \quad (2.29)$$

with the positive and Hermitian quantum process matrix  $\hat{\chi}$ , which we obtain by reshaping the evolution coefficients  $\chi_{mn}$  into a  $(d^2 \times d^2)$  matrix. In other words, the superoperator  $\mathcal{E}$ , which acts on the initial density matrix  $\hat{\rho}$  to obtain the final  $\mathcal{E}(\hat{\rho})$ , is encoded in the process matrix  $\hat{\chi}$ . Consequently, the goal of QPT is achieved if an expression for the  $\hat{\chi}$ -matrix in terms of experimentally available data can be found. To do so, we need to apply the quantum process, whose fidelity we want to analyze, to  $d^2$  independent quantum states  $\hat{\rho}_i$  of the system. The  $\hat{\rho}_i$  then form a basis for the space of the complex Hermitian matrices of dimension  $(d \times d)$ . By applying the quantum operation  $\mathcal{E}$  to the chosen input states  $\hat{\rho}_i$ , we obtain  $\mathcal{E}(\hat{\rho}_i)$ , which can be decomposed in the  $\hat{\rho}_i$ -basis:

$$\mathcal{E}(\hat{\rho}_i) = \sum_j \lambda_{ij} \hat{\rho}_j \quad (2.30)$$

To switch to the basis of the experiment  $\{\hat{B}_m\}$ , we can find coefficients  $\beta_{ji}^{mn}$  such that

$$\hat{B}_m \hat{\rho}_i \hat{B}_n^\dagger = \sum_j \beta_{ji}^{mn} \hat{\rho}_j. \quad (2.31)$$

If the  $(d^2 \times d^2)$  matrix  $\hat{\chi}$  is reshaped into a column vector  $\boldsymbol{\chi}$  and the  $d^2$  values  $\lambda_{ij}$  are reordered in a column vector  $\boldsymbol{\lambda}$ , the  $\beta_{ji}^{mn}$  can be interpreted as the entries of a matrix

$B$  with  $B_{ji, mn} = \beta_{ji}^{mn}$  and the problem can be rewritten as

$$\boldsymbol{\lambda} = B \cdot \boldsymbol{\chi}. \quad (2.32)$$

This means that  $\hat{\chi}$  can be obtained by multiplying  $\boldsymbol{\lambda}$  with the (pseudo-)inverse of  $B$  and reshaping  $\boldsymbol{\chi}$ . After that,  $\hat{\chi}$  can be diagonalized

$$\hat{\chi} = UDU^\dagger \quad (2.33)$$

with  $D = \text{diag}(q_1, \dots, q_{d^2})$  and the Kraus-operators  $\hat{E}_i$  can be found by using  $\hat{E}_i = \sqrt{q_i} \sum_m U_{mi} B_m$ , where  $q_i$  are the eigenvalues of the diagonal matrix  $D$ . If  $\hat{\chi}$  represents a physical process matrix, it must be positive Hermitian, which implies that there are no negative eigenvalues:  $q_i \geq 0$ . Additionally,  $\hat{\chi}$  should be trace-preserving ( $\sum_{m,n} B_m \hat{\chi}_{mn} B_n^\dagger = I$ ). This attribute is inherited from the Kraus representation. For better practical implementation, a vector quantity that contains all basis matrices is defined  $\mathbf{B} \equiv (B_1^\dagger, \dots, B_{d^2}^\dagger)$ . In experiments with a single qubit, we have  $d^2 = 4$ . For this case, we choose the  $\mathbf{B}$ -vector as

$$\mathbf{B} = (I, X, iY, Z), \quad (2.34)$$

where  $I$  is the 2x2 identity matrix,  $X \equiv \hat{\sigma}_x$ ,  $Y \equiv \hat{\sigma}_y$  and  $Z \equiv \hat{\sigma}_z$  [cf. Eq. (1.29)]. For the independent initial states  $\{\Psi_i\}$ , we choose  $|g\rangle$ ,  $|e\rangle$ ,  $|+\rangle$  and  $|-\rangle$  [44]. The quantum process  $\mathcal{E}$  is applied to each of these states. Both the initial states and the resulting states  $\mathcal{E}(|g\rangle\langle g|)$ ,  $\mathcal{E}(|e\rangle\langle e|)$ ,  $\mathcal{E}(|+\rangle\langle +|)$  and  $\mathcal{E}(|-\rangle\langle -|)$  are reconstructed using QST (cf. Fig. 2.32).

In order to simplify the reconstruction of  $\hat{\chi}$  and transform it into a block matrix, we switch to the following basis of auxiliary density matrices [73].

$$\hat{\rho}_1 = \begin{pmatrix} 1 & 0 \\ 0 & 0 \end{pmatrix} \quad \hat{\rho}_2 = \begin{pmatrix} 0 & 1 \\ 0 & 0 \end{pmatrix} \quad \hat{\rho}_3 = \begin{pmatrix} 0 & 0 \\ 1 & 0 \end{pmatrix} \quad \hat{\rho}_4 = \begin{pmatrix} 0 & 0 \\ 0 & 1 \end{pmatrix} \quad (2.35)$$

In this new basis, the resulting states  $\hat{\rho}'$  are linear combinations of the actually measured outcome  $\mathcal{E}(\Psi_i)$ .

$$\hat{\rho}'_1 = \mathcal{E}(|g\rangle\langle g|) \quad (2.36)$$

$$\hat{\rho}'_2 = \mathcal{E}(|+\rangle\langle +|) + i\mathcal{E}(|-\rangle\langle -|) - \frac{(1+i)}{2} [\mathcal{E}(|g\rangle\langle g|) + \mathcal{E}(|e\rangle\langle e|)] \quad (2.37)$$

$$\hat{\rho}'_3 = \mathcal{E}(|+\rangle\langle +|) - i\mathcal{E}(|-\rangle\langle -|) - \frac{(1-i)}{2} [\mathcal{E}(|g\rangle\langle g|) + \mathcal{E}(|e\rangle\langle e|)] \quad (2.38)$$

$$\hat{\rho}'_4 = \mathcal{E}(|e\rangle\langle e|) \quad (2.39)$$

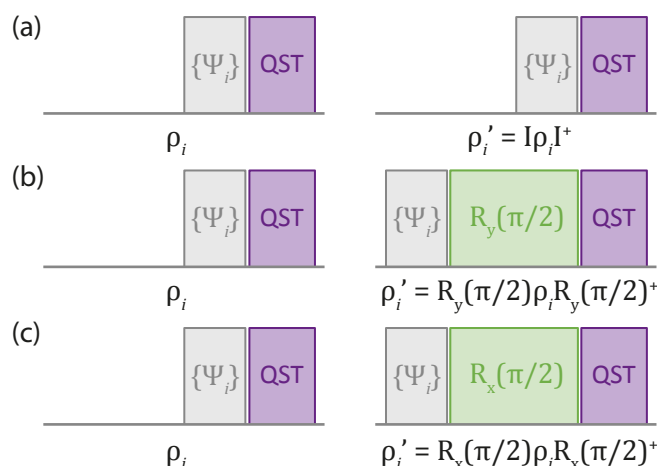


**Figure 2.32:** Schematic pulse protocols for QPT. In the first step, QST is performed on a set of independent states  $\{\Psi_i\}$ . Afterwards, QST is performed on the same set of states, to which a quantum operator is applied. This can be (a) the identity operator, (b) a rotation of  $\pi/2$  about the  $y$ -axis and (c) a rotation of  $\pi/2$  about the  $x$ -axis. For this kind of measurement, an  $IQ$ -modulated setup (cf. Fig. 2.24) is necessary in order to control the qubit phase.

Finally, we can express the process matrix as

$$\hat{\chi} = \Lambda \cdot \begin{pmatrix} \hat{\rho}'_1 & \hat{\rho}'_2 \\ \hat{\rho}'_3 & \hat{\rho}'_4 \end{pmatrix} \cdot \Lambda \quad (2.40)$$

where  $\Lambda$  includes the auxiliary transformation<sup>29</sup> and is also a block matrix consisting of  $I$  and  $X$ .

$$\Lambda = \frac{1}{2} \begin{pmatrix} I & X \\ X & -I \end{pmatrix} \quad (2.41)$$

We apply QPT in experiment on a single qubit and determine the  $\hat{\chi}$ -matrix for the identity operation, for a rotation of  $\pi/2$  with respect to the  $y$ -axis and for a rotation with respect to the  $x$ -axis. The minimum number of different measurements for a single process matrix can be calculated from the number of measurements for QST  $n_{\text{QST}}$  and the number of the basis states  $n_{\Psi} = |\{\Psi_i\}|$ . Since QST is performed once without and a second time with the quantum operation (cf. Fig. 2.30), we have to account for a factor of 2. In total, we obtain  $2 \cdot n_{\Psi} \cdot n_{\text{QST}} = 2 \cdot 4 \cdot 3 = 24$ .

The results from QPT are depicted in Fig. 2.33. The fidelity is determined in the same manner as in the QST case. In our measurement (cf. sample QMv3 2<sup>nd</sup> in Tab. B.2 in the appendix) and for the identity operation, the fidelity of the QPT is  $F_1 = 97.37\%$ . This value is almost identical to the bare QST fidelities, since no actual operation takes

<sup>29</sup>It can be shown that for the chosen auxiliary basis, there is a closed expression for  $B$ , which is related to  $\Lambda$  as  $B = \Lambda \otimes \Lambda$

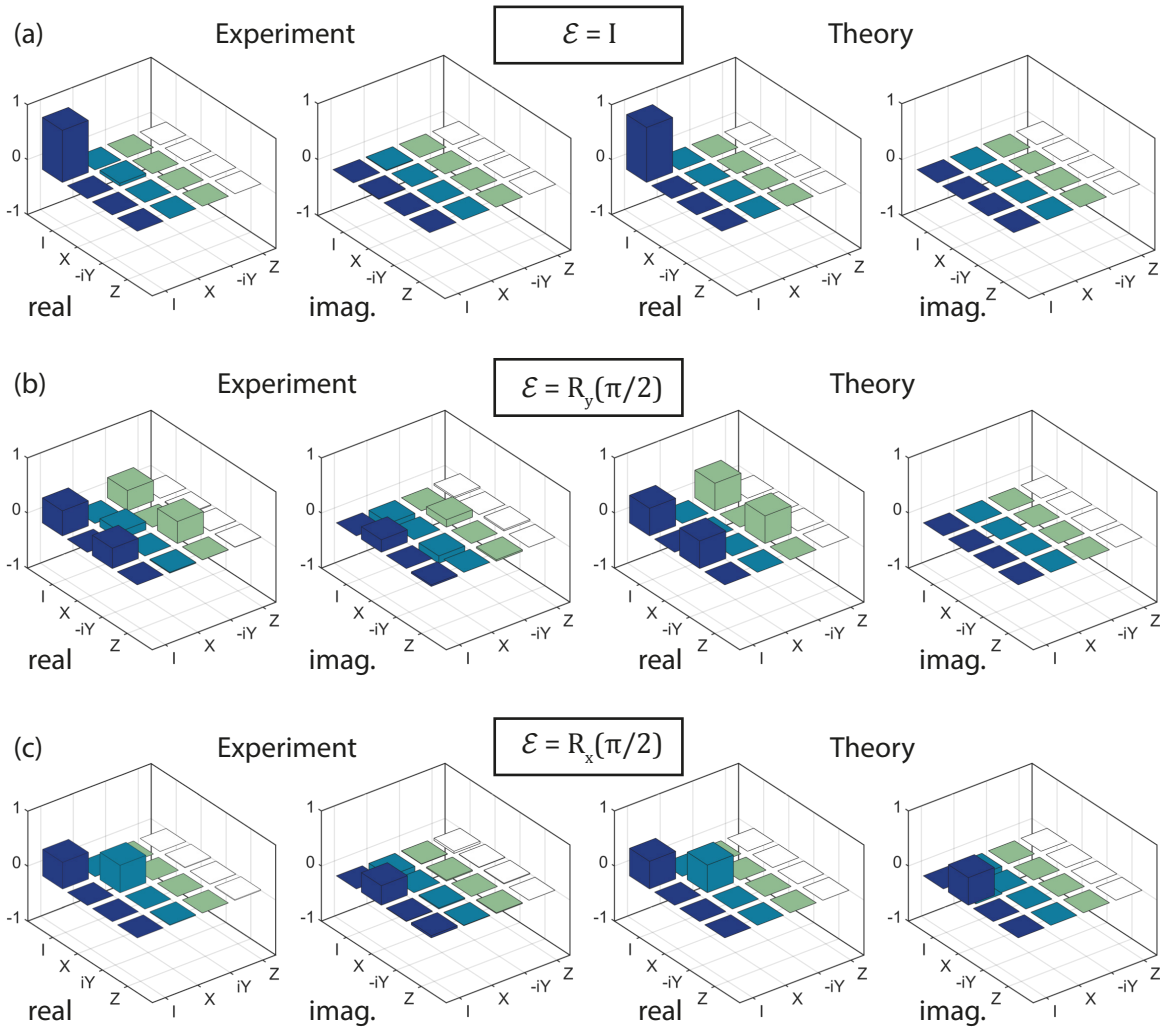


**Figure 2.33:** Measured QPT for three distinct quantum operations on a single qubit (cf. sample QMv3 2<sup>nd</sup> in Tab. B.2 in the appendix). We compare the process matrix from experimental data with the theoretically expected process matrix. The color code is for better visibility of the single matrix elements. The resulting fidelities are  $F_I = 97.37\%$ ,  $F_{R_y(\pi/2)} = 89.03\%$  and  $F_{R_x(\pi/2)} = 90.85\%$ .

place. For a rotation about the  $y$ -axis, the fidelity drops and we get  $F_{R_y(\pi/2)} = 89.03\%$ . The reconstruction fidelity of a rotation about the  $x$ -axis  $F_{R_x(\pi/2)} = 90.85\%$  has a similar value as compared to a rotation about the  $y$ -axis. This result shows, that the qubit phase control in the experiment is reliable, since the rotation around the  $y$ -axis is the natural operation, whereas for the rotation about the  $x$ -axis, we need to specify a drive phase  $\varphi_d = 90^\circ$ . From estimations (cf. Sec. 3.4.2), we can identify qubit decay and state leakage as the main sources for fidelity limitations in this experiment.

### 2.3.8 Suppression of state leakage

The approach to use (flattop) Gaussian pulses is limited when aiming for very short pulses, where the length of the pulse mainly determines the spectral width. A 10 ns long pulse physically has a minimum spectral width of 100 MHz. In the case of a weakly anharmonic transmon qubit, where the anharmonicity is similar to the spectral width of the pulse, the pulse causes higher level excitations. We refer to this phenomenon as state leakage. In other words, the qubit population leaves the computational space spanned by  $|g\rangle$  and  $|e\rangle$ . To avoid these scenarios, a special pulse shape has been developed, which is the derivative removal by adiabatic gate (DRAG) method [76, 134–136]. The necessary control pulses are shown in Fig. 2.34 (a) and are described as

$$I(t) = \Omega_\pi \quad (2.42)$$

$$Q(t) = -\frac{\dot{\Omega}_\pi}{\alpha/\hbar} \quad (2.43)$$

where  $\Omega_\pi$  is a Gaussian pulse, which creates a  $\pi$ -flip in the computational space. We note, that the quadrature component is the time derivative of the in-phase component scaled with the inverse of the anharmonicity. These pulse envelopes can be derived from an effective Hamiltonian as first order solutions with minimal state leakage. The leakage is eliminated to order  $\Omega_\pi^4/(\alpha/\hbar)^3$  as compared to a pure Gaussian pulse [cf. Fig. 2.34 (b)]. For typical values ( $\Omega_\pi/2\pi = 60$  MHz and  $\alpha/h = -92$  MHz), we obtain an attenuation of approximately 10 dB in the spectrum of the pulse at the unwanted frequency.

The gate fidelity is increased, as it can be seen in Fig. 2.34 (c) in the Bloch sphere representation. In this simple picture, the difference between DRAG and non-DRAG pulses is that the drive phase is controlled during the pulse in such a way, that the qubit trajectory ends closer to the desired final state. When looking at the spectral distribution of the DRAG pulse shape [cf. Fig. 2.34 (d)], we see that the frequency at  $-2\alpha/h$  is eliminated to a certain degree. Hence, in the energy level scheme, the transition from the ground state to the second qubit level as a two-photon process is avoided.

In experiment, the population of higher qubit levels leads to an unwanted additional dispersive shift, which spoils the dispersive readout. This can be seen in Fig. 2.35 (a). For sharp rectangular pulses with 1 ns rise time, the readout resonator signal does not follow the typical Rabi oscillation pattern, but additional dispersive shifts [cf. Eq. (1.54)] are measurable. This problem can be overcome by using the DRAG method. Then, the oscillations are exactly centered with respect to the mixed state with  $\langle\sigma_z\rangle^2 = 0$ . We note that the Rabi oscillations are recorded versus the drive amplitude and, hence, should not exhibit any temporal decay. However, the data shows a decreasing amplitude of the oscillations, when using DRAG. In an intuitive way, this behavior can be explained by

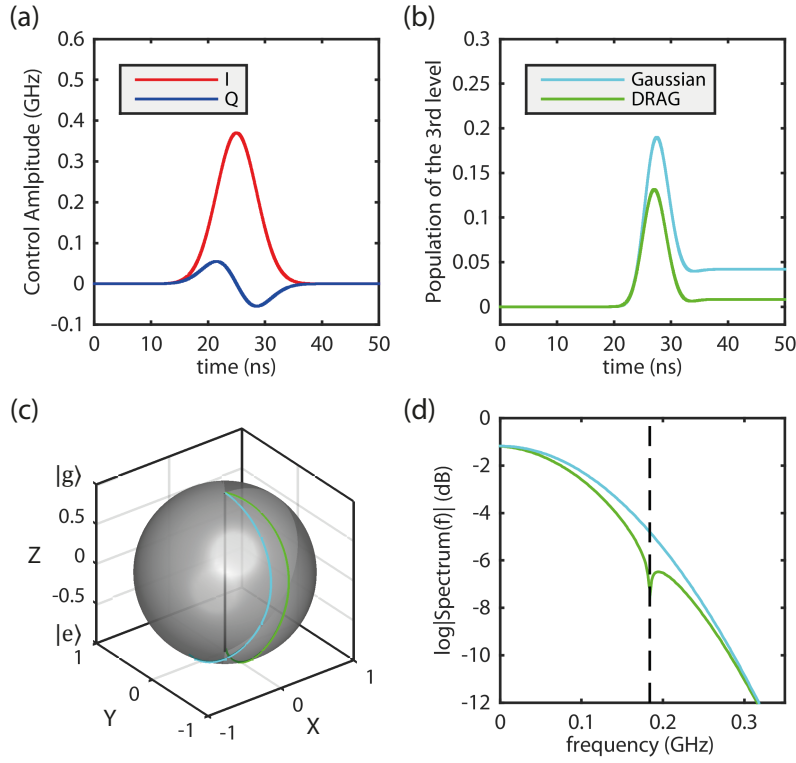


**Figure 2.34:** (a) Pulse envelopes of typical DRAG pulse for  $I$  and  $Q$  matched to a qubit with  $\omega_q/2\pi = 3.87$  GHz and  $\alpha/h = -92$  MHz (cf. sample B in Tab. B.2 in the appendix). The pulse length and control amplitude are chosen to create a  $\pi$ -flip. (b) Calculated leakage population for a Gaussian pulse (cyan) compared to a DRAG pulse (green). A significant suppression in leakage population is clearly seen. (c) Bloch sphere representation of qubit dynamics during the pulse shown in (a). Due to the adiabatic changes in the DRAG protocol, the final state is closer to the ideal  $|e\rangle$  state when using DRAG. According to simulations, we obtain a state preparation of 99.554 % for the DRAG  $\pi$ -pulse shown in (a) and a fidelity of 94.978 % for a pure Gaussian  $\pi$ -pulse. The infidelity ( $1 - F$ ) can also be seen in (c) at the end of the pulse at 50 ns. (d) Calculated frequency spectrum of the DRAG pulse (green) shown in (a) compared to a pure Gaussian pulse (cyan). The suppressed frequency of  $-2\alpha/h$  is indicated by the dashed line.

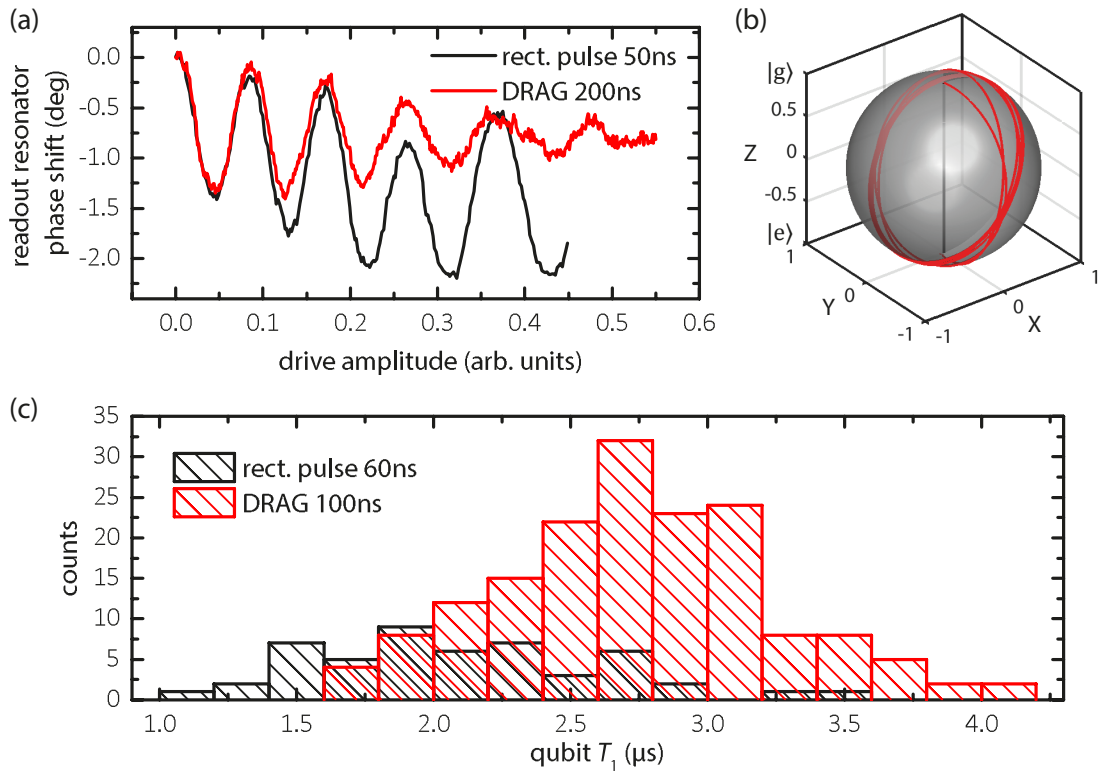


**Figure 2.35:** (a) Qubit Rabi oscillations with rectangular pulse shape (50 ns) and DRAG pulse shape (200 ns). The pulse envelope is kept fixed to maintain a constant spectral width of the pulse. We choose the length of the pulses, such that the area enclosed by the pulse envelope is equal. This leads to the same oscillation frequency, when the drive amplitude of the carrier tone is swept. In the case of DRAG, the Rabi oscillations are centered around the mixed state, whereas for the spectrally wide rectangular pulse, the Rabi oscillations are skewed. The qubit used in this measurement has  $\omega_q/2\pi = 3.87$  GHz and  $\alpha/h = -92$  MHz (cf. sample B in Tab. B.2 in the appendix). (b) Qubit trajectory on the Bloch sphere after applying a DRAG pulse with high amplitude. The qubit state vector is rotated multiple times about the  $x$ -axis. The rotational plane gets tilted due to the DRAG pulse. Hence, a nominal  $3\pi$ -pulse does not bring the qubit into the excited state with a high fidelity. (c) Qubit  $T_1$  statistics. The excited state is prepared with a DRAG (165 times) or rectangular (50 times)  $\pi$ -pulse. We note that the pulse envelopes differ from those used in (a).

the fact, that the DRAG pulse, in contrast to the rectangular pulse, does not induce a rotation about the  $x$ -axis, which is parallel to the  $zy$ -plane, but which has a curvature [cf. Fig. 2.35 (b)]. If we increase the drive amplitude, we let the state vector rotate more often on the Bloch sphere. In each round, the rotational plane acquires an additional tilt by a certain angle, leading to a diminished contrast on the measurement  $z$ -axis for high drive amplitudes. In order to accurately prepare an excited qubit state with the DRAG technique, such high drive amplitudes are not necessary, since only a  $\pi$ -pulse with comparably low amplitude is applied.

We can make use of a qubit  $T_1$  measurement to quantify the accuracy of the prepared excited state, since the leakage population can be the cause for a wrong assessment of the qubit  $T_1$  time. In general, the qubit  $T_1$  time is a measure for the energy relaxation from  $|e\rangle$  to  $|g\rangle$ . However, leakage population with a higher decay rate is measured together with the actual decay rate. For the qubit described in this paragraph, we find with rectangular pulses  $T_1^{\text{rec}} = 2.09 \pm 0.53 \mu\text{s}$ , and with DRAG  $T_1^{\text{DR}} = 2.75 \pm 0.50 \mu\text{s}$  [cf. Fig. 2.35 (c)]. The latter is a better description of the real qubit  $T_1$ , because it is strictly limited to the computational space. We can estimate the impact of the leakage population  $p_L$  with a simple rate equation, if we assume the decay time of the leakage population to be  $T_1^L = T_1/\sqrt{2}$ , since the  $i$ th higher level coupling also follows a  $1/\sqrt{i}$  law. The total rate equation for the relevant decay times reads

$$\frac{1}{T_1^{\text{rec}}} = p_e \frac{1}{T_1^{\text{DR}}} + p_L \frac{1}{T_1^L}. \quad (2.44)$$

Here, the total population is normalized to  $p_L + p_e = 1$ . The ground state population does not need to be considered in this rate equation, since no decay occurs from the ground state. In other words, we only distinguish between population in the computational space with a decay time of  $T_1^{\text{DR}}$  and population in all other transmon qubit levels with a decay time of  $T_1^L$ . For the measured  $T_1$  values, we evaluate the leakage population to be  $p_L = 0.76$ , if we presume  $T_1^{\text{DR}}$  to coincide with the actual qubit  $T_1$ . This value appears to be reasonable, if we bear in mind that the dispersive shift is also altered by a factor of 1.5 for certain drive powers [cf. Fig. 2.35 (a)], indicating a similar population of the computational space and higher levels.

Using the DRAG technique in experiment is typically advantageous in terms of state preparation fidelities. Nevertheless, we would like to point out that the example shown here is a qubit with a particular low anharmonicity, which makes the use DRAG pulses very effective. For transmon qubits with a higher anharmonicity, the effect of applying DRAG pulses decreases. If we assume a qubit with  $\alpha/h = -185 \text{ MHz}$  and a 50 ns  $\pi$ -pulse, then the state preparation fidelity for a DRAG  $\pi$ -pulse is 99.998% versus 99.177% for a pure Gaussian  $\pi$ -pulse according to simulations. At some point, owing the complexity of this technique, it is often more robust to use flat-top Gaussian pulses.

# Chapter 3

## Results

This chapter<sup>1</sup> begins with a description of the quantum memory sample. The technical optimization of the storage mode is shown and the resulting improvement is discussed. Based on qubit manipulation pulses, we explain the memory pulse sequence. By executing single steps of the sequence, we can present data on coherent population transfer to and from different intermediate states. With the full protocol implemented, we are able to measure a significant enhancement in storage time for arbitrary initial states. On the sidelines of these investigations, we present data on higher cavity modes, which may also serve as potential memory modes. Finally, we discuss the fidelity of the protocol and estimate the limitations.

### 3.1 Quantum memory protocol

In circuit QED architectures, long storage times and fast readout are conflicting requirements, asking for slow and fast cavity decay, respectively. A possible solution is to physically separate the storage and the readout resonators [32, 33, 137–139]. However, regarding scalability and reduction of footprint, this approach is not optimal. By combining the high  $Q$ -factors of 3D cavities with the fast readout capabilities and compactness of 2D resonators, the system dimensions can be reduced [37]. Another promising approach is to use the multimode structure of 2D resonators [43]. In this case, the system turns out to be even more compact and scalable, however, this is achieved at the expense of a rather low storage time of only 1.45  $\mu\text{s}$ . To combine the benefits from both approaches, the multimode structure of a single 3D cavity can be employed [140, 141]. On the one hand, we take advantage of high- $Q$  3D cavities and, on the other hand, we entirely get rid of a separate readout resonator without losing the fast readout capability.

---

<sup>1</sup>Most parts of this chapter are based on the publication "Compact 3D quantum memory", Applied Physics Letters, **112**, 202601 (2018).

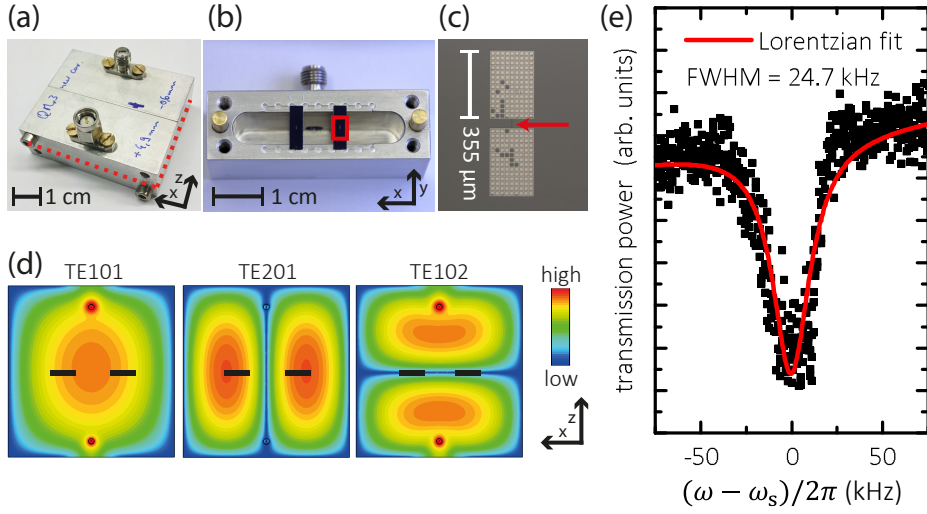


**Figure 3.1:** (a) Photograph of the aluminum 3D cavity. The red dashed line indicates the equatorial plane of the cavity. (b) Open cavity with two qubit chips. The red rectangle marks the position of the transmon qubit. The chips are fixed with small pieces of indium. (c) Optical micrograph of the superconducting transmon qubit. The two metallic capacitors are connected via a submicron Josephson junction indicated by the red arrow. (d) Simulated  $y$ -component of the electric field distribution in the cavity equatorial plane for the lowest three modes. Antenna pins are depicted as circles. The chip positions are marked with black rectangles. Their center positions are placed off the cavity center by 6.2 mm. (e) Transmission measurement of the storage mode (dots) with Lorentzian fit (line).

### 3.1.1 Optimized storage and readout mode

The cavity is made of aluminum (Al 99.5 %) with two antennas for external coupling [cf. Fig. 3.1 (a)]. It is mounted inside a dilution refrigerator with approximately 30 mK base temperature. From an FEM simulation [50] of the cavity transverse electric (TE) modes [cf. Fig. 3.1 (c)], we observe that the TE101 mode can be overcoupled while maintaining an undercoupled TE201 mode by properly placing the coupling antennas. In this way, the completely decoupled, highly coherent TE201 mode can be used for information storage and the well-coupled TE101 mode for dispersive readout at a megahertz rate [22]. In our configuration, the fundamental TE101 readout mode  $\omega_{\text{RO}}/2\pi = 5.518$  GHz is overcoupled and has a decay rate  $\kappa_{\text{RO}}/2\pi = 25$  MHz, whereas the first harmonic TE201 storage mode<sup>2</sup>  $\omega_{\text{s}}/2\pi = 8.707546$  GHz has a decay rate  $\kappa_{\text{s}}/2\pi = 155$  kHz [cf. Fig. 3.1 (d)]. From a bare cavity measurement (cf. Sec. 2.1.1), we estimate the internal  $Q$ -factors  $Q_0^{\text{RO}} \simeq 1.5 \cdot 10^6$  and  $Q_0^{\text{s}} \simeq 6 \cdot 10^5$ .

<sup>2</sup>Due to the small decay rate on the order of tens of kilohertz, we give the value of  $\omega_{\text{s}}$  with a kilohertz precision.

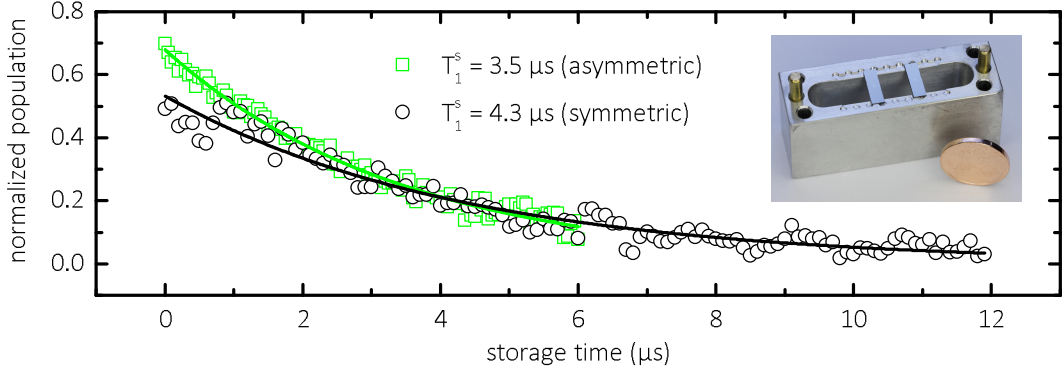


**Figure 3.2:** Comparison of storage mode single photon Fock state decay for two different chip configurations (cf. sample QMv3 1<sup>st</sup> and QMv4 3<sup>rd</sup> in Tab. B.2 in the appendix). Inset: Symmetric chip configuration. In the case of the asymmetric chip configuration, one of the chips is missing. The cavities from both measurements are made of the same material (Al 99.5 %) and are without subsequent surface treatment. The single photon Fock state is prepared as described in Fig. 3.4. The reason for the population loss at zero storage time is found in state leakage (cf. Sec. 3.2).

### Mode symmetry and qubit coupling

For the TE201 mode to be symmetric with regard to the antennas [cf. Fig. 3.1 (b)], we insert two  $3 \times 10 \text{ mm}^2$  large silicon chips centered near the electric field antinodes. In Fig. 3.2 we compare the decay times of a Fock state in the storage mode for the symmetric (two chips) and the asymmetric (one chip) sample configuration (cf. sample QMv3 1<sup>st</sup> and QMv4 3<sup>rd</sup> in Tab. B.2 in the appendix). We observe a  $T_1^s$  improvement of approximately 20 % with the symmetric configuration.

On one of the chips, we fabricate the single-junction transmon qubit using aluminum technology and double-angle shadow evaporation. Due to its off-center placement inside the cavity, it couples to both the TE101 and the TE201 mode simultaneously with an equal coupling strength  $g/2\pi \simeq 53 \text{ MHz}$ . In addition, there is a small residual coupling  $g_{102}/2\pi \simeq 8 \text{ MHz}$  to the TE102 mode [80]. The qubit transition frequency  $\omega_q/2\pi = 6.234 \text{ GHz}$  is designed to fall in between  $\omega_s$  and  $\omega_{RO}$  resulting in dispersive shifts of  $\chi'_{RO}/2\pi = 3.6 \text{ MHz}$  and  $\chi'_s/2\pi = -1.1 \text{ MHz}$  for the readout and storage mode, respectively. We measure an average qubit energy decay time  $T_1^q = 1.32 \pm 0.05 \mu\text{s}$  and a decoherence time  $T_2^q = 2.49 \mu\text{s}$ , which is obtained via a Ramsey-type experiment [cf. Fig. 2.25 (d)]. The qubit has an anharmonicity  $\alpha/h = (\omega_{ef} - \omega_q)/2\pi \simeq -185 \text{ MHz}$ . Due to the large detuning between qubit and readout mode, the qubit lifetime is not Purcell limited, even though the readout mode is designed to have a fast decay. For our sample, the Purcell limit for the qubit lifetime is calculated to be  $20 \mu\text{s}$ .

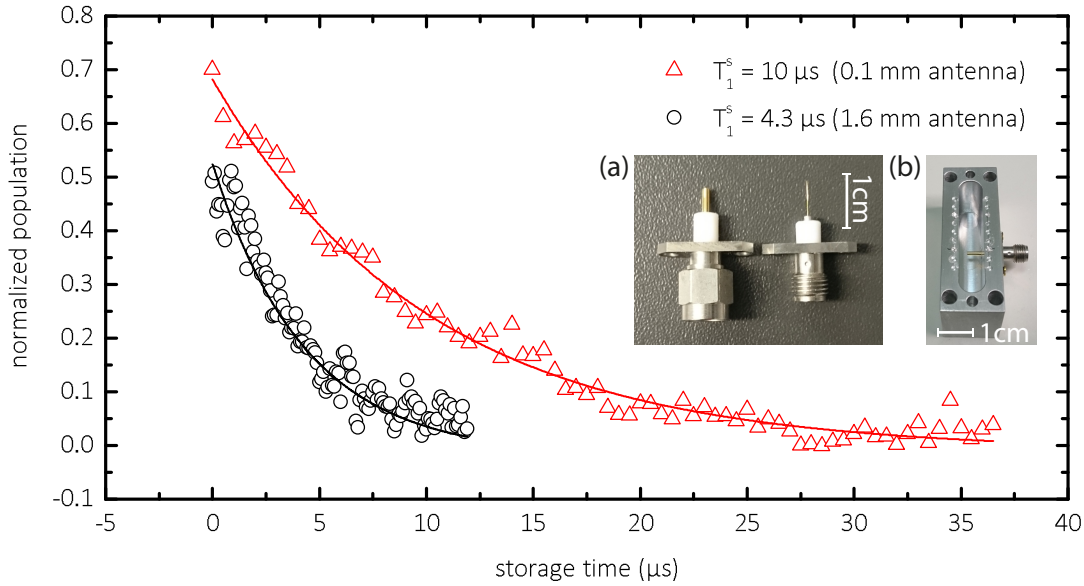


**Figure 3.3:** Comparison of storage mode single photon Fock state decay for two different antenna configurations (cf. sample QMv3 2<sup>nd</sup> and QMv4 3<sup>rd</sup> in Tab. B.2 in the appendix). The reason for the population loss at zero storage time is found in state leakage (cf. Sec. 3.2). Inset (a) Photograph of commercial antenna (left) and modified version with slimmer diameter (right). Inset (b) Photograph of commercial antenna mounted in open cavity.

### Slim antenna

The mode profile of the TE<sub>201</sub> mode in the  $x$ -direction at the antenna position favors slim antennas in order to keep the coupling low. Commercial antennas<sup>3</sup> come with a diameter of 1.6 mm. We slim it down to 0.1 mm as described in Sec. 2.1.1.

As already pointed out in Fig. 2.4 (b), the highest  $Q_x^s$  is achieved at a center position at exactly  $x = 0$ . However, in experiment, such conditions are difficult to fulfill. Deviations from this sweet spot let  $Q_x^s$  drop rapidly. In the case of the modified slim antenna, this  $Q$ -factor decrease is alleviated as compared to the off-the-shelf antenna. In the end, for reaching high  $Q_x^s$  this means that the positioning accuracy becomes less demanding when using a slim antenna. In Fig. 3.3, we present storage mode Fock state decay data from two different quantum memory samples, where both samples feature the symmetric chip mounting and differ only in the antenna diameter (cf. sample QMv3 2<sup>nd</sup> and QMv4 3<sup>rd</sup> in Tab. B.2 in the appendix). With the slim antenna, we are able to increase  $T_1^s$  by approximately a factor of 2.3.

If we conclude the improvements from using a symmetric chip configuration and from using a slimmer antenna, we reason that both approaches are necessary. In the first step, the symmetric chip configuration ensures the antinode of the storage mode to coincide exactly with the antenna position. Only if this criterion is met, the coupling to

<sup>3</sup>Huber+Suhner 23\_SMA-50-0-13

the antenna can be reduced even more by choosing a slimmer antenna diameter.

### 3.1.2 Memory pulse sequence

We now discuss the storage protocol based on the energy level diagram shown in Fig. 3.4 (a). Neglecting small second-order shifts, the equidistant ladder of the harmonic storage mode is shifted by the amount of the qubit energy if the qubit is excited. For the quantum memory protocol, we need to drive the blue sideband transition from  $|g0\rangle$  to  $|e1\rangle$  between these two ladders with the frequency  $\omega_b \equiv \omega_s + \omega_q + \chi_s + (2n_{\text{RO}} - 1)\chi_{\text{RO}}$ . Here, we take into account the dispersive shifts  $\chi_{\text{RO}}$  of the readout and  $\chi_s$  of the storage mode. In the experiment, we keep  $n_{\text{RO}} \simeq 0$  during the protocol sequence. To fulfill parity conservation [142], we drive the BSB transition with two photons at  $\omega_b/2$ . This transition is described by the effective BSB Hamiltonian from Eq. (1.65).

Our measurement protocol [cf. Fig. 3.4 (b)] starts with a qubit preparation pulse. By placing it at the beginning of the memory sequence, we are able to transfer various states into the memory. The actual memory sequence begins with a  $\pi$ -pulse on the BSB transition. In this way, the ground state population of the qubit  $p_g$  is transferred to the first excited memory state on the right ladder. Then, by means of a qubit  $\pi$ -pulse, the qubit is deexcited and all population is swapped back to the left ladder. As a result, the qubit state is now encoded in the first two states of the storage mode [43]. Specifically, the qubit ground (excited) state is transferred to the first excited (ground) state of the storage.

For state retrieval, we use the same pulse scheme in a reverse order and map the excitation back onto the qubit, which we read out dispersively. In general, we use flat-top Gaussian pulses with a rise time of 20 ns to minimize leakage to higher qubit levels (cf. Sec. 2.3.3).

## 3.2 Coherent population transfer and decoherence effects

When considering the qubit-resonator energy level diagram with its many levels, we are not limited to the qubit subspace only, but are able to coherently swap population to and from composite states of qubit and resonator. In our protocols, we typically start in  $|g0\rangle$ , where the resonator and the qubit are not excited. Applying a coherent drive pulse at  $\omega_q$  with a certain pulse length creates a driven Rabi oscillation between  $|g0\rangle$  and  $|e0\rangle$ , which is depicted in Fig. 3.5 (a)<sup>4</sup>. The Rabi oscillation measurements

<sup>4</sup>Please note, that the qubit-cavity system used in this section is different from the one used for the full quantum memory protocol. The key parameters are:  $\omega_q/2\pi \simeq 5.360$  GHz,  $\alpha/h \simeq -300$  MHz,  $\omega_r/2\pi \simeq 5.485$  GHz,  $g/2\pi \simeq 32$  MHz,  $T_1^{\text{q}0} \simeq 159$  ns and  $T_1^{\text{s}} \simeq 3.8$   $\mu\text{s}$  (cf. sample QMv4 2<sup>nd</sup> in Tab. B.2 in the appendix).

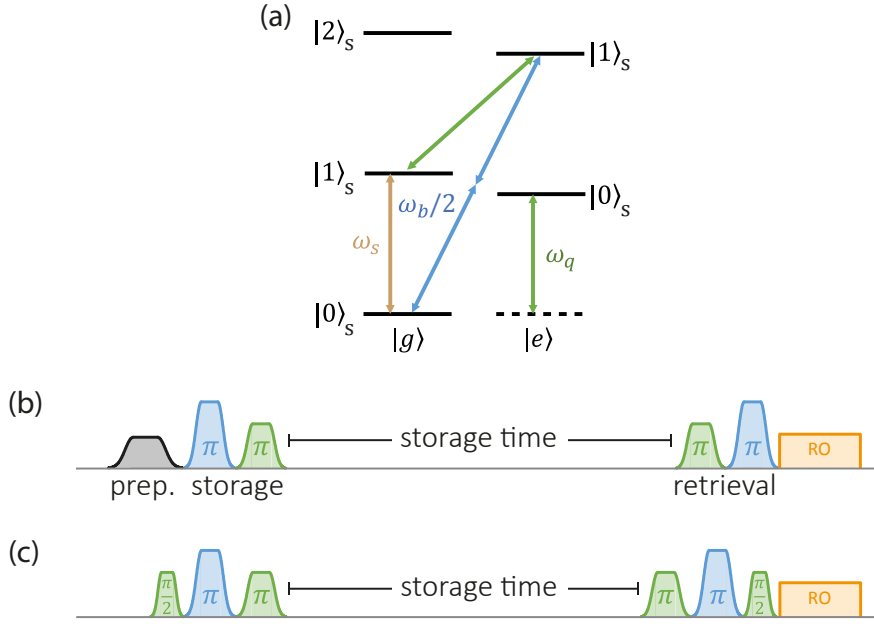


**Figure 3.4:** (a) Level scheme of the qubit ( $\omega_q$ ) coupled to the storage mode ( $\omega_s$ ). The second-order transition from  $|g0\rangle$  to  $|e1\rangle$  is driven with two photons of frequency  $\omega_b/2$ . (b) Quantum memory protocol for storage and retrieval. Grey: Qubit preparation pulse. Blue: BSB pulse. Green: Qubit pulse. Orange: Readout (RO) pulse applied to the readout mode. (c) Ramsey-type sequence for the quantum memory protocol. The preparation pulse is a  $\pi/2$ -pulse in order to bring the qubit into a superposition state. Another  $\pi/2$ -pulse is sequenced in front of the readout pulse in order to map the qubit state back onto the  $z$ -axis.

are performed by reading out the qubit state dispersively (cf. Sec. 2.2.4). From the fit to the data, we determine  $T_1^{q0} = 159 \pm 7$  ns, which is well below the Purcell limit of 822 ns of the qubit-resonator system [cf. Eq. (1.74)]. The qubit-resonator detuning is  $\Delta \simeq -125$  MHz. Due to decoherence, the total coherent population is diminished exponentially with time. After a time of  $t \approx T_1^{q0}$ , only  $p_e \simeq 0.37p_e^0$  remain, where  $p_e^0$  is the initial excited state population, and for  $t \gg T_1^{q0}$ , we obtain a mixed state with a steady state population  $p_e^{\text{st}}$ .

From  $|g0\rangle$  we can reach the  $|e1\rangle$  level by coherently pumping two photons at  $\omega_b/2$  into the system. Here, a single photon Fock state is created in the resonator and the excited level of the qubit is populated simultaneously. We notice that the steady state population for long Rabi drive pulses is not centered around 0.5 anymore. This can be explained via a rate equation [143], where we take into account the drive rate  $\Omega_b/2\pi \simeq 3.3$  MHz, the qubit decay rate  $\gamma/2\pi \simeq 6.3$  MHz and the storage mode decay rate  $\kappa_s/2\pi \simeq 0.26$  MHz. The value for the drive rate is extracted from the Rabi oscillation fit, whereas the other two values are from separate measurements. Since  $\gamma$  is the dominating decay in this configuration, in the steady state, population will be built up on the  $|g1\rangle$  level. Then,

the steady state excited population can be estimated to

$$p_e^{\text{st}} = 1 - \frac{\gamma\Omega_b}{\gamma\Omega_b + \kappa_s\Omega_b + \gamma\kappa_s} \simeq 11\%. \quad (3.1)$$

This value coincides well with the Rabi oscillation data of the BSB transition in Fig. 3.5 (b).

In order to determine the maximum initial population  $p_e^0$  at  $t = 0$ , we extrapolate the curve with an exponential function, which has the same decay time as the BSB Rabi oscillation  $T_1^{\text{b}} = 497 \pm 53$  ns. This decay time is a combination of the storage mode decay time and the qubit decay time. As a result, we obtain  $p_e^0 \simeq 30\%$ , which means, that  $p_L = 1 - p_e^0 = 70\%$  of the population is not transferred via the BSB transition in the first place and is not available for further processing. Due to the use of rectangular pulses with 1 ns rise times and the required high power to drive the BSB, we can attribute this leakage population to parasitic population transfers to higher levels of the transmon qubit. The qubit in this experiment has an anharmonicity of  $\alpha/h \simeq -300$  MHz. In this extreme case, where  $p_L$  is very large, the memory enhancement will only work for a small percentage of the population. By means of diminishing  $p_L$ , more population can be transferred into the long-lived cavity mode leading to a higher visibility. In another experiment (cf. sample QMv3 2<sup>nd</sup> in Tab. B.2 in the appendix), where the anharmonicity of the qubit is even lower ( $\alpha/h \simeq -185$  MHz), we achieve with flat-top Gaussian pulses  $p_L \simeq 35\%$  [cf. Fig. 3.5 (d)]. Consequently, for transmon qubits with their low anharmonicity, the use of flat-top Gaussian pulses is much more advantageous than the use of rectangular pulses.

Next, we investigate Rabi oscillations of the qubit with a single photon Fock state in the cavity. The  $|e1\rangle$  state is reached with a BSB  $\pi$ -pulse. Then a coherent drive at  $\omega_q$  is applied to coherently swap the qubit population. Hence, the driven Rabi oscillation occurs between  $|e1\rangle$  and  $|g1\rangle$ . In Fig. 3.5 (c), we show such a Rabi oscillation measurement. Compared to the qubit Rabi oscillations with no photon inside the cavity, we notice that the oscillation starts with  $|e1\rangle$  and the oscillation amplitude is much smaller. The reduced oscillation amplitude is due to the preceding 160 ns BSB  $\pi$ -pulse, which is comparable to  $T_1^{\text{q}}$  and, hence, the loss of population due to energy relaxation is significant. Apart from this, there is no measurable difference between Rabi oscillations with zero or one photon in the cavity. An energy relaxation time  $T_1^{\text{q}1} = 130 \pm 20$  ns is determined from the fit, which agrees well with  $T_1^{\text{q}0}$ .

### 3.3 Enhanced quantum information storage time

In order to study the decay time of the quantum memory (cf. sample QMv3 2<sup>nd</sup> in Tab. B.2 in the appendix), we use a protocol preparing the qubit in the  $|g\rangle$  state to obtain the Fock state  $|1\rangle_s$  in the memory. The decay of this state is plotted versus the

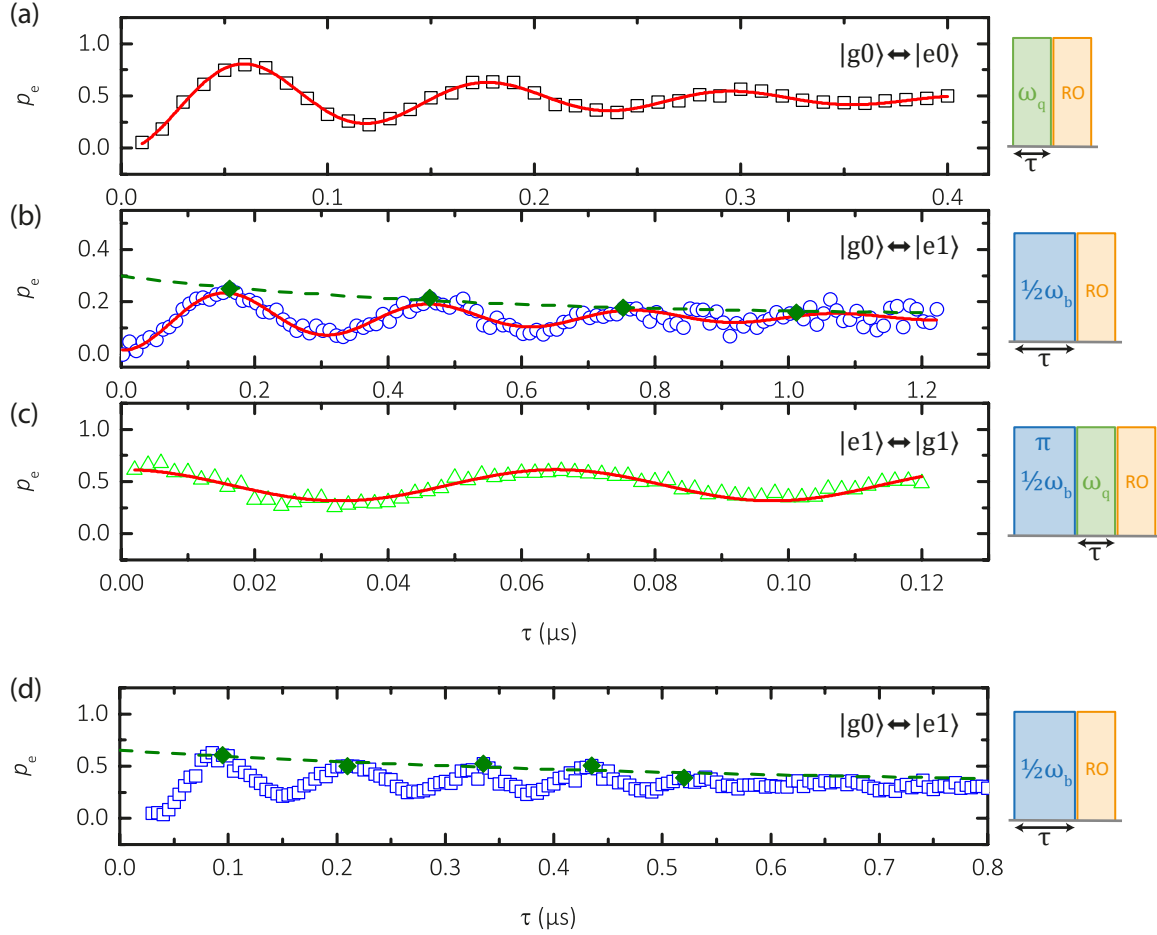


**Figure 3.5:** Driven Rabi oscillation measurement between various states of the qubit-cavity system (cf. sample QMv4 2<sup>nd</sup> in Tab. B.2 in the appendix). The data (dots) is fitted with a damped sine function (red line). Next to the graphs, we draw the corresponding pulse schemes. (a) Qubit-only Rabi oscillation between  $|g0\rangle$  and  $|e0\rangle$  without an excitation in the cavity. (b) Blue sideband two-photon transition driven with a coherent drive at  $\omega_b/2$ . Green diamonds are local maxima used for fitting the exponential envelope (dotted green). The leakage population at  $t = 0$  is  $p_L = 70\%$ . (c) Qubit Rabi oscillations with a single photon Fock state in the cavity. The drive power used here differs from the drive power used in (a) leading to an altered Rabi frequency. (d) Coherently driven blue sideband transition performed on a different sample (cf. sample QMv3 2<sup>nd</sup> in Tab. B.2 in the appendix) as compared to the data in (a)-(c). Another difference is the use of flat-top Gaussian pulses with a rise time of 20 ns in (d) in contrast to rectangular pulses with a 1 ns rise time in (a)-(c). Consequently, the leakage population at  $t = 0$  is reduced to  $p_L = 35\%$ .

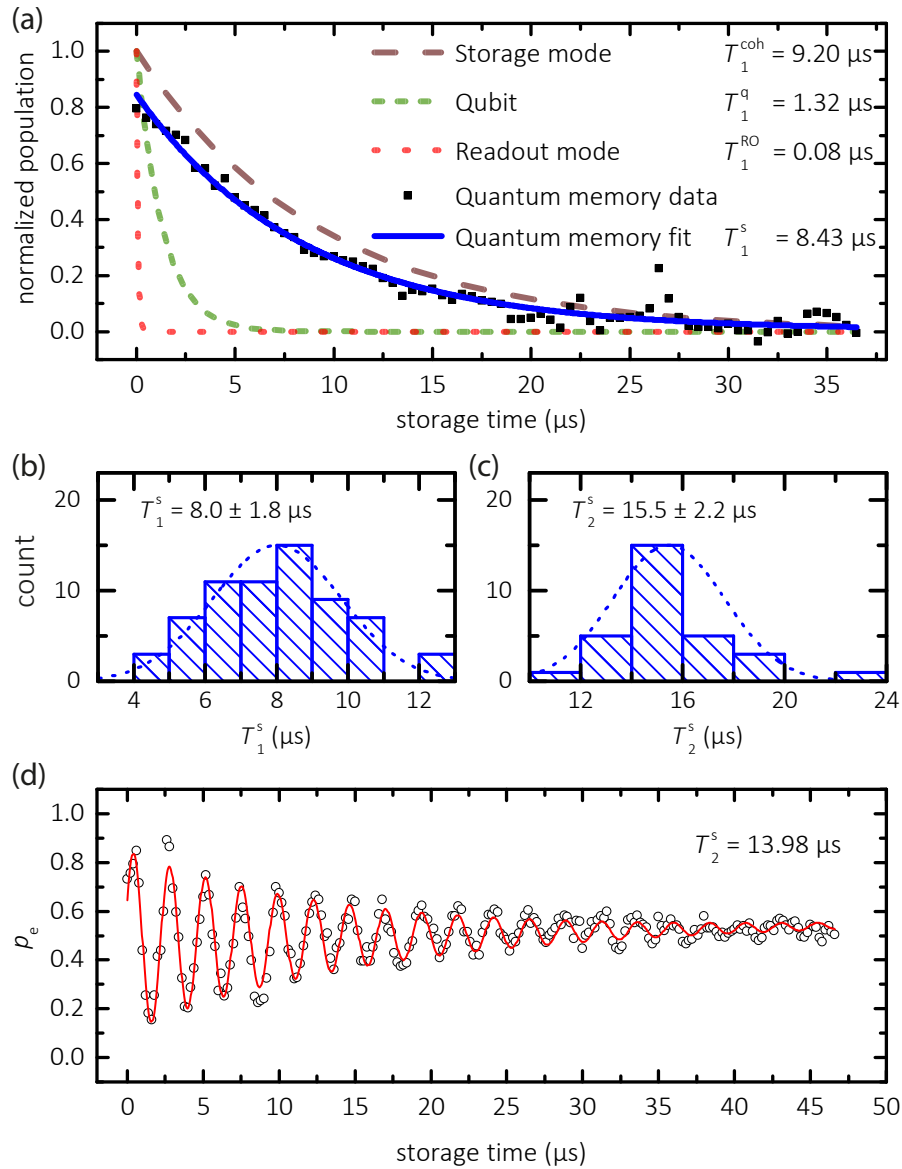


**Figure 3.6:** (a) Comparison of decay rates of the quantum memory system (cf. sample QMv3 2<sup>nd</sup> in Tab. B.2 in the appendix). (b) and (c) Statistics of the  $T_1^{\text{s}}$  and  $T_2^{\text{s}}$  of a Fock state  $|1\rangle_{\text{s}}$  in the storage mode. (d) Ramsey-type  $T_2^{\text{s}}$  measurement data (dots) fitted with a damped sine function (red line).

storage time in Fig. 3.6 (a). We measure an average relaxation time  $T_1^s = 8.0 \pm 1.8 \mu\text{s}$ . The data is in good agreement with an exponential decay. Small deviations from this behavior can be attributed to measurement artifacts. We can also perform a protocol preparing the qubit in state  $1/\sqrt{2}(|g\rangle + |e\rangle)$  and rotating the qubit by  $\pi/2$  at the end of the protocol [cf. Fig. 3.4 (c)]. Such Ramsey-type measurement yields  $T_2^s = 15.5 \pm 2.2 \mu\text{s}$ . Figure 3.6 (b) and (c) display histograms of the measured memory decay and decoherence times, respectively. Both follow a normal distribution. These fluctuations are frequently observed in literature and typically explained by ensembles of microscopic two-level fluctuators [91, 144]. The measured coherence time is slightly lower than expected from the  $2T_1$ -bound [cf. Eq. (1.71)]. As a result, we extract a dephasing time  $T_\varphi^s = (1/T_2^s - 1/2T_1^s)^{-1} = 0.5 \text{ ms}$  for the storage mode. Originally, a bare harmonic oscillator exhibits no dephasing, however, in our case, we can explain this behavior by considering a stochastic qubit jump rate [42] between  $|g\rangle$  and  $|e\rangle$ . This process results in frequency jumps of  $\omega_s$  due to the dispersive interaction and, as a consequence, in a loss of phase information. We consider this mechanism to be dominant in our experiment because, via the relation [41]  $\gamma_\varphi \simeq p_e \gamma$  [cf. Eq. (1.76)], with  $\gamma$  being the qubit decay rate and  $\gamma_\varphi$  the pure dephasing rate, we extract a qubit excited state population in equilibrium  $p_e = 0.3\%$  in agreement with an estimate [145] based on the temperature of the cavity walls of 50 mK. Furthermore, both  $T_1^s$  and  $T_2^s$  are by a factor of 6 longer than their bare-qubit counterparts. This observation is another indication, that the storage mode partially inherits the dephasing properties of the qubit. Finally, we compare the quantum storage time with the decay time of a coherent state in the storage mode. To this end, we excite the storage mode directly with a sufficiently long microwave pulse of frequency  $\omega_s$  and directly monitor the field leaking out of the resonator (cf. Fig. 3.7). The resulting value  $T_1^{\text{coh}} = 9.2 \mu\text{s}$  agrees well with the Fock state storage time  $T_1^s$  within the expected statistical variation.

The next parameter of interest is the decay time of the readout mode  $T_1^{\text{RO}}$ , which we determine to  $T_1^{\text{RO}} = 80 \text{ ns}$  in a similar way. This values shows that the overcoupled antenna configuration allows us to read out the qubit state on a time scale 100 times shorter than the storage time. A similar 2D system [43] with a single planar on-chip resonator reaches only a factor of 37. With a single 3D cavity [140, 141], ratios of 16.7 and 154 have been demonstrated. Using a combination of two rectangular superconducting 3D cavities [32, 33, 137–139], where one serves for readout and the other one for storage, ratios of 15.8, 45.8, 1500, 1818 and 2500 are obtained. By proper surface treatment of the cavity, we expect to be able to increase  $Q_0^s$  to approximately  $5 \cdot 10^7$  as demonstrated in Ref. [49]. Our simulations [cf. Fig. 3.1(e)] show that comparable values can be obtained for  $Q_x^s$  with a more accurate antenna positioning of  $\pm 0.016 \text{ mm}$ . In this way, we predict that the ratio between readout and storage time could be extended to 25 000, exceeding the highest currently reported value of 7300 for superconducting qubit-memory architectures employing cylindrical 3D cavities [35]. Other memory

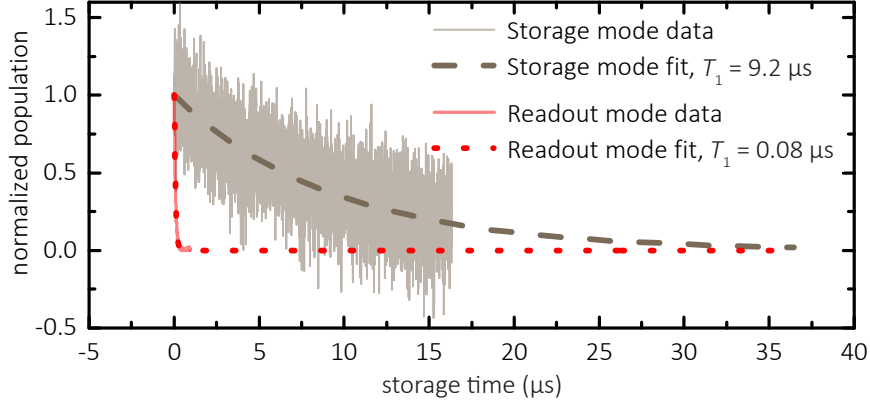


**Figure 3.7:** Decay of a coherent state in the storage mode and the readout mode (cf. sample QMv3 2<sup>nd</sup> in Tab.B.2 in the appendix). Dotted and dashed lines are fits to the data. Details on the measurement technique are found in Sec. A.3 in the appendix.

systems, such as spin-ensembles coupled to superconducting qubits, exhibit storage times comparable to rectangular superconducting 3D cavities [46, 146]. However, the spread in Rabi frequencies is a source for dephasing and the low cooperativity leads to a low efficiency in terms of the absorbed and re-emitted signal. Both drawbacks are not present in our type of system. Quantum memories based on nano-mechanical resonators also have similar storage times [45], but currently suffer from access times which are two orders of magnitude higher than those presented in this work.

### 3.3.1 Higher cavity memory modes

The placement of the antenna pins enables us to analyze higher cavity modes, other than the TE201 mode, as memory modes. These are modes, which couple well to the qubit, but only weakly to the antennas. According to Tab. 2.5, these are TE203, TE401 and TE403. The electric field distribution for these modes is depicted in Fig. 3.8 (a)-(c). We perform the memory protocol from Fig. 3.4 on the TE203 mode<sup>5</sup> and find a storage time of  $T_1^{302} = 1.5 \mu\text{s}$  (cf. sample QMv3 2<sup>nd</sup> in Tab. B.2 in the appendix). This value is only slightly higher than the bare qubit decay time. From simulations, we expect the TE203, TE401 and TE403 modes to have lower storage times due to a steeper mode profile in the  $x$ -direction at the antenna position, since the antinodes are more cramped in the cavity volume [cf. Fig. 3.8 (d)]. Consequently, the modes are more difficult to decouple from the antenna because small antenna positioning inaccuracies lead to a relatively high residual electric field interacting with the antenna.

To improve these storage times, which means to decrease the external coupling, one

<sup>5</sup>The BSB  $\pi$ -pulse is limited by the output power  $P_d \simeq 25 \text{ dBm}$  of the PSG RF source. With this and the reduced effective coupling due to a larger detuning, a minimum  $\pi$ -pulse length of 150 ns is achieved.

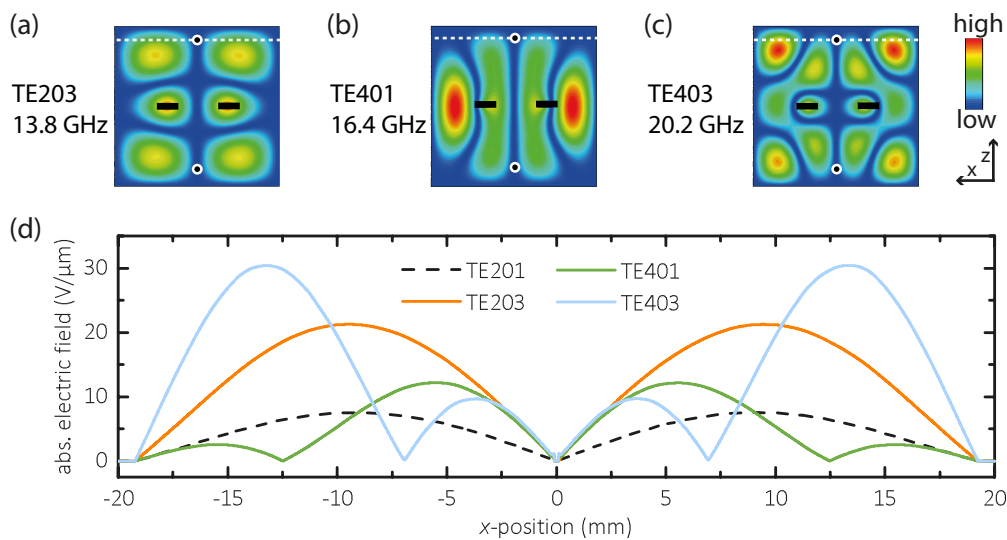


**Figure 3.8:** (a)-(c) Electric field distribution of higher cavity modes for potential quantum memory applications. The coupling to the antennas (white circles) is low, whereas the coupling to the off-center qubit chips (black rectangles) is high. (d) Absolute electric field evaluated along the white dashed line in (a)-(c). The electric field of the TE201 mode (black dashed line) is plotted for comparison and has a significantly smaller slope around  $x = 0$  than the field of the other modes. For all modes, the electric field vanishes at  $\pm 19.2$  mm due to the cavity wall. Simulations are performed using CST Microwave Studio [50] on the cavity model described in Sec. C.1 in the appendix.

has to optimize the cavity antennas to fit these modes better by making them even slimmer. A more precise chip positioning helps to maintain the symmetry of the electric field and lets the positions of the nodes of the higher modes coincide with the antennas. With regard to the memory protocol, a higher drive power for the BSB is required to obtain short pulses, since higher cavity modes are further detuned from the qubit and the effective coupling decreases with  $1/\Delta$ . A small drawback of the higher cavity modes is that the frequency spectrum at these higher mode frequencies is crowded due to second- and third-order transitions, which occur as multiples or combinations of lower frequency transitions. Nevertheless, we have demonstrated that the option to access these higher modes as quantum memories is given despite the fact that optimization remains a technical challenge.

### 3.3.2 Storage of superposition states

So far, only the ground state of the qubit has been stored in the memory. In this section, we investigate the storage of superposition states. In Fig. 3.9, the decay during the storage time is shown for qubit states prepared with different preparation pulse lengths. The typical Rabi oscillation pattern is visible, however, with a significantly smaller decay rate as compared to that of the bare qubit. Hence, we find that superposition

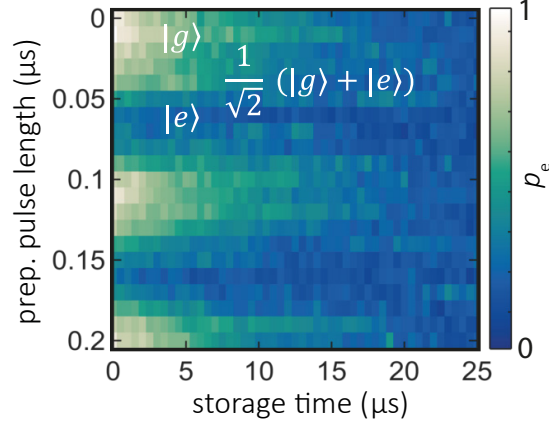


**Figure 3.9:** Decay of qubit superposition states transferred to the memory (cf. sample QMv3 2<sup>nd</sup> in Tab. B.2 in the appendix). The quantum memory protocol is applied to qubit states with different Rabi angles. An equal superposition state of the qubit is stored as  $1/\sqrt{2}(|0\rangle_s + |1\rangle_s)$  in the memory.

states of the qubit are stored as superpositions of Fock states in the storage mode as expected.

### 3.4 Quantum memory fidelity

The next step is to quantify how well a quantum state can be stored in the memory. To this end, we characterize the fidelity of the protocol by means of the retrieved qubit population  $p_g(t_p)$  after the protocol of duration  $t_p$ . The  $Z$  fidelity  $F_Z = p_g(t_p)/p_g(0)$ , which is the fidelity obtained from measurements along the quantization axis, is depicted in Fig. 3.11 (a) for seven different working points of the quantum memory protocol. At each working point, we perform several quantum memory measurements with calibrated  $\pi$ -pulses. The working points differ in the average protocol length  $t_p$ . When using short pulses, which require a higher drive power to accomplish a  $\pi$ -rotation, we achieve a maximum of  $F_Z = 82 \pm 7\%$ . Longer  $t_p$  let the maximum fidelity drop to  $76 \pm 3\%$  due to qubit decay during the pulse sequence. However, within the statistical error margins,  $F_Z$  is constant over the range of protocol lengths. As a cross-check, we perform quantum process tomography of the memory protocol starting in the  $|g0\rangle$  state. We find a process fidelity  $F_{\text{QPT}} = 78\%$ . The process matrix is plotted in Fig. 3.10 (for technical details cf. Sec. E.2 in the appendix). This value coincides very well with the outcomes of the  $Z$  fidelity measurements and proves that our experiment is not limited by dephasing. Hence, further analysis is performed using  $F_Z$ . To shed more light onto the origin of these observations, we make  $F_Z$  from protocols of various lengths comparable by computationally eliminating the qubit decay. From this corrected  $Z$  fidelity  $F_Z^{\text{corr}} = F_Z/\exp(-t/T_1^q)$ , we determine a maximum value of  $F_Z^{\text{corr}} = 96 \pm 4\%$

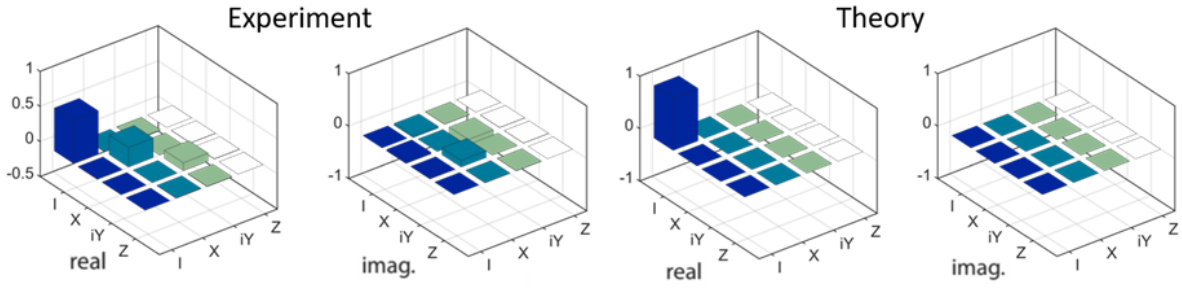


**Figure 3.10:** Measured  $\hat{\chi}$  and theoretical  $\hat{\chi}_t$  for the quantum memory protocol performed on sample QMv3 2<sup>nd</sup> (cf. Tab. B.2 in the appendix).

for  $t_p = 370$  ns as shown in Fig. 3.11 (b). This value is already very close to the ideal fidelity and errors come from state leakage as discussed in Sec. 3.4.2.

### 3.4.1 Reduction of fidelity variation

In this section, we analyze the stability of the setup with regard to drive power fluctuations. To this end, we use the memory fidelity variations as a figure of merit. We find that the qubit participating in the memory experiment is subdued to AC Stark shifts from various mode populations [cf. Eq. (1.58)]. Strong drives at the cavity antenna lead to such populations and, hence, shifted transition frequencies. Especially the strong drive necessary for the BSB transition suffers from a drive power dependent frequency shift. In Fig. 3.12 (a), we plot the AC Stark shift of  $\omega_b/2$  for different drive powers. In a setup without any band-pass filters, the shift accounts to approximately 150 MHz for the relevant drive powers. We test various band-pass filter configurations<sup>6</sup> by recording the shifted  $1/2\omega_b$ . The transmission characteristics of the inserted filters is shown in App. A.2. These band-pass filters prove to be a practical solution to suppress spurious population of other cavity modes. The total shift can be decreased to 10 MHz. However, it remains unknown, which mode exactly causes the AC Stark shift. According to Eq. (1.66) and Fig. 2.22, candidates are modes, which couple well to the antenna (high  $\Omega_d$ ) and well to the qubit (high  $g$ ) simultaneously. Additionally, they are relatively close to the qubit in frequency (low  $\Delta$ ).

We benchmark these filter configurations by looking at  $F_Z^{\text{corr}}$ . The fidelity for each configuration is averaged over multiple runs of the same memory experiment. For each run, the pulse lengths for the  $\pi$ -pulses and the frequency of the drives are automatically determined by a tune-up procedure (cf. Fig. 2.26). We report on a decrease in fidelity variation as demonstrated in Fig. 3.12 (b) with a more or less constant absolute  $F_Z^{\text{corr}}$ . Conclusively, we gain more stable experimental conditions when limiting the drive bandwidth of the pulsed microwave signal. This result is supported by the decrease in

<sup>6</sup>Mini Circuits VBF-7200+ and VBF-7350+

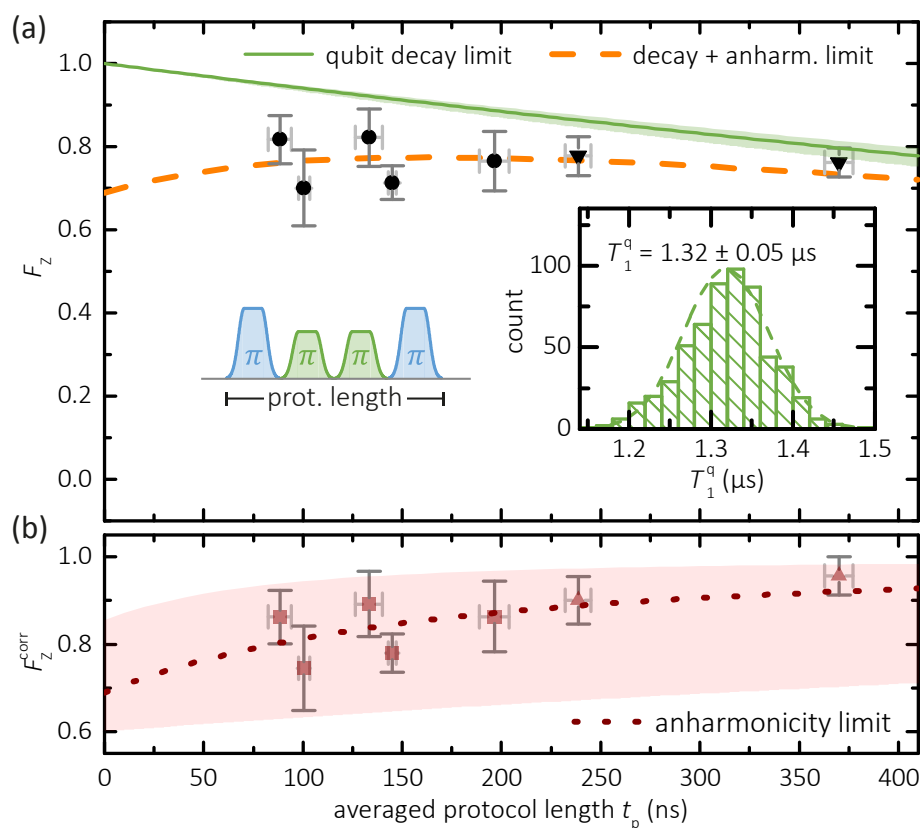


**Figure 3.11:** (a)  $Z$  fidelity measurements of the quantum memory protocol depending on the protocol length. Green line: maximum fidelity limited by qubit decay with  $T_1^q$ . Light green area: Statistical variations. Protocol lengths (inset) are set using different drive powers. Triangles: Long protocol lengths are achieved using  $3\pi$  pulses for the qubit transition. Orange dashed line: product of the qubit decay limited fidelity and the anharmonicity limited fidelity  $F_Z^{\text{corr}}$ . Inset: Histogram of  $T_1^q$ . (b)  $Z$  fidelity corrected for the qubit decay in order to make different protocol lengths comparable. Dotted line: fit. Red transparent region: Fit uncertainty.

relative variations in  $t_p$ . The effect of using different pulse shapes, such as rectangular or flat-top Gaussian pulses, is discussed in the next paragraph in terms of qubit state leakage.

### 3.4.2 State leakage fidelity limit

Interestingly, in Fig.3.11 we observe a lower  $F_Z^{\text{corr}}$  for shorter protocol lengths in contradiction to the expectation that the fidelity could be limited by qubit decay. This result points to a typical source of error for transmon qubits, namely state leakage caused by the low anharmonicity. To quantify the leakage [76], we use a simplified picture and define the leakage rate as  $\gamma_L = \gamma^\uparrow + \gamma^\downarrow + \gamma_{\text{sp}}$ , with the excitation rate  $\gamma^\uparrow$ , the stimulated emission rate  $\gamma^\downarrow$  and the spontaneous emission rate  $\gamma_{\text{sp}}$  to

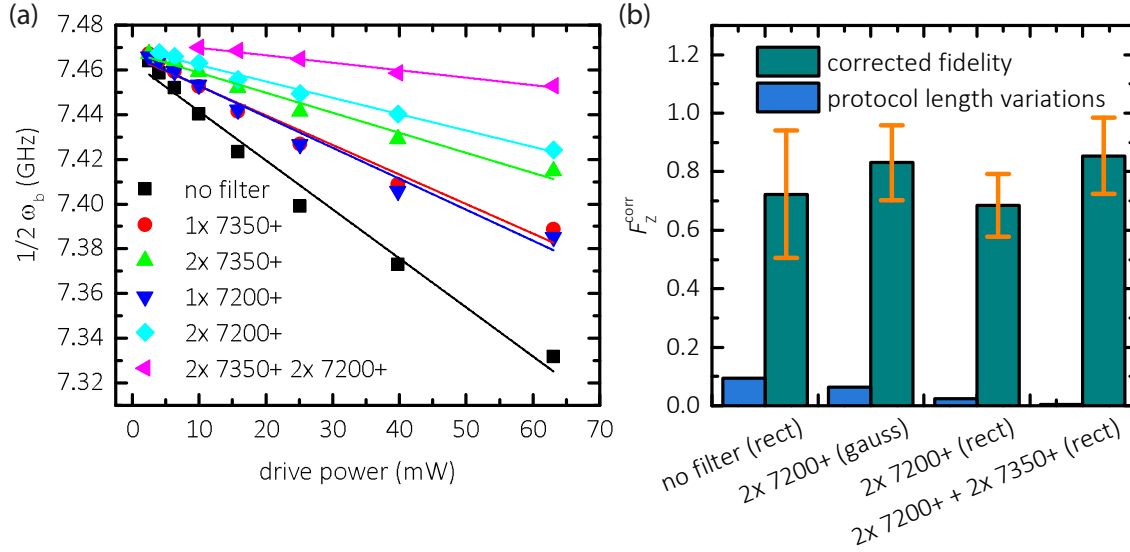


**Figure 3.12:** (a) AC Stark shift of the BSB transition for different drive line filter configurations. (b) Variations in  $F_Z^{\text{corr}}$  and  $t_p$  for different filter configurations. In the brackets, we state the pulse shape. The variations in  $t_p$  are relative to the total protocol length.

and from higher states, respectively. Then, we can write the steady state leakage population  $p_L = \gamma^\uparrow/\gamma_L [1 - \exp(-\gamma_L t_p)] = a/(2a + \gamma_{\text{sp}} t_p) [1 - \exp(-2a - \gamma_{\text{sp}} t_p)]$ , with  $a = \gamma^\uparrow t_p = \gamma^\downarrow t_p$ . The rates  $\gamma^\uparrow, \gamma^\downarrow$  are directly proportional to the drive strength  $\Omega_{\text{drv}}$  and indirectly proportional to  $t_p$ , because the spectral width of our flat-top Gaussian shaped pulses with a fixed rise time is independent of the plateau length. We can identify  $a$  with the ability of the drive pulse to create a leakage population, which depends on the fixed pulse rise time and the anharmonicity of the qubit. In the end, the corrected Z fidelity is expected to behave as  $F_Z^{\text{corr}} = 1 - p_L(t_p, a, \gamma_{\text{sp}})$ . We use this function with  $a$  and  $\gamma_{\text{sp}}$  as fit parameters to fit our data. Fitting the data we obtain the reasonable value  $\gamma_{\text{sp}}/2\pi = 13.8 \pm 11.5$  MHz for the spontaneous emission rate. The leakage population at  $t_p = 0$  is  $p_L = 31\%$ . This value coincides well with the calculated  $p_L = 35\%$  from Fig. 3.5 (d) for the same sample and pulse shapes. Therefore, when aiming for even shorter pulses, the fidelity will be limited to  $F_Z \simeq 69\%$  due to the qubit anharmonicity. To further increase the fidelity, optimal control pulses are necessary to reduce state leakage for short pulses [134]. In addition, a longer qubit lifetime [42] would allow for longer pulses and, in turn, for a higher fidelity at a given anharmonicity.

# Chapter 4

## Conclusions and Outlook

In conclusion, we have designed superconducting microwave 3D cavities suitable for quantum memory experiments [78, 97]. For cavity design, an FEM simulation procedure has been established using the eigenmode solver and the frequency domain solver of CST Microwave Studio [50], to study the electric field distribution of the fundamental and higher cavity modes. A machined cavity made of 99.99% Al displays an internal  $Q$ -factor exceeding one million at millikelvin temperatures without extensive surface treatment. The  $Q$ -factor is independent of the photon population inside the cavity and remains constantly high down to the single photon level. This stands in strong contrast to planar resonators, where the  $Q$ -factor decreases with decreasing photon population due to the strong coupling to omnipresent two-level fluctuators [60]. Complementary, the external  $Q$ -factor has been studied alongside with the coupling mechanism via the antennas. We have quantified the coupling of the antenna pins to the electric field, which can easily be adjusted by changing the length of the antennas and their position relative to a field antinode.

In order to make use of the high- $Q$  cavities for qubit experiments, the qubit design has to be adapted to fulfill the requirement of strong coupling. We have shown that the design parameters of the transmon qubits can be reduced to simply designing the geometry of the transmon qubit shunt capacitors. We have developed a method to successfully simulate the RF capacitance of a transmon qubit in CST Microwave Studio [50]. To do so, the transmon qubit can be treated as an  $LC$ -circuit with the inductance being a free adjustable parameter. In the simulation, we spectroscopically probe this circuit in a waveguide environment similar to the cavity geometry. This simulated capacitance has been validated in experiment to be sufficiently correct [103]. With this at hand, we are able to build 3D transmon qubits. In terms of nanoscale qubit fabrication, a new electron beam lithography system together with a new spin-coater has been set up. The fabrication recipe has been adapted to the new facilities and optimized towards high fabrication yield and reproducibility [107]. We pre-characterize the 3D transmon qubits with a defined set of spectroscopic measurements to gain the experimentally relevant parameters  $\omega_q$  and  $\alpha$  and the parameters relevant for fabrication such as  $C_\Sigma$  and  $I_c$ . In the end, combining both newly designed components, the highly coherent

3D cavity and the transmon qubit, we measure qubit energy relaxation properties in the microsecond regime. WMI record coherence times of  $T_1 \simeq 2.7 \mu\text{s}$  and  $T_2 \simeq 3.4 \mu\text{s}$  have been demonstrated in experiment. At the time of this thesis, coherence times of a transmon qubit in a superconducting 3D cavity are reported to be about  $150 \mu\text{s}$  for  $T_1$  and  $240 \mu\text{s}$  for  $T_2$  [147, 148].

This paves the way for more complex pulse protocols including multiple pulses at different transition frequencies. In this field, we have analyzed and optimized pulse shapes starting from simple rectangular pulses over (flattop) Gaussian shaped pulses up to  $IQ$ -modulated DRAG pulses. These are suitable remedies, counteracting the drawback of the low transmon qubit anharmonicity in order to keep unwanted state leakage low. In an experiment using a transmon qubit with a low anharmonicity of  $\alpha/h = -92 \text{ MHz}$ , the population leakage is reduced from 76 % with rectangular pulses to an estimated value close to 0 % with DRAG pulses.

For an accurate description of state leakage, several steps towards quantum state tomography of a qubit have been taken. We have implemented a measurement protocol for tomography and find that our state preparation occurs with a fidelity close to 1. Furthermore, for characterizing arbitrary quantum processes, we have experimentally demonstrated quantum process tomography for single qubit gates with decent fidelity. This protocol can be effortlessly adapted to more complex quantum operations.

As a final result, we have realized a quantum memory protocol for a fixed-frequency transmon qubit by harnessing the multimode structure of a single 3D cavity. In this way, we have access to a long-lived storage mode but retain a fast readout capability. We successfully store qubit superposition states into the memory. The ratio between the storage and the readout rate is determined to be 100 and shows a significant improvement compared to planar multimode resonators (ratio of 37) [43]. Our result is on a par with values measured for single rectangular 3D cavities (ratio of 154) [141]. Furthermore, our measurements indicate that the dephasing of the memory is limited by the coupling to the qubit. We find a maximum  $Z$  fidelity of  $82 \pm 7 \%$  for the optimal trade-off between qubit anharmonicity and relaxation rate in our sample. This value matches well with the quantum process fidelity of  $F_{\text{QPT}} = 78 \%$ .

With few straightforward technical improvements, our compact platform can be further improved to store cat states [33] or GHZ states [36] for continuous variable quantum computing. In detail, surface polishing techniques can enhance  $Q_0$  of the cavity [41, 149] and qubit chip substrate pre-treatment [60, 150] can increase the bare qubit lifetime.

Regarding scalability, there are multiple attractive options. For example, more superconducting qubits using the storage mode as a bus can be inserted into the cavity for building logical qubits [151]. Furthermore, coupling the qubit to higher cavity modes allows for a quantum memory register [152]. In this direction, we have already performed pre-characterization measurements. With respect to analog quantum simulation, the

implementation of Bose-Hubbard chains [153] with the storage modes acting as bosons is facilitated by our compact architecture and less constraints on the amount of control lines (cf. Fig. B.1 in the appendix). In particular, one can think of 2D lattice geometries for simulation of molecules [154] or solid state systems [155].



# Appendix A

## Experimental setup details

### A.1 Measurement strategy

Here, we describe an established measurement sequence to characterize the relevant parameters of a qubit-cavity system from the scratch. The procedure is summarized in Tab. A.1. We specify the input parameters, the measurement type and the obtained parameters.

Meas.	Known param.	X sweep	Y sweep	Meas. type	Meas. outcome
Disp. shift	-	$P_{\text{RO}}$	$\nu$	transm.	$\chi, Q, \nu_{\text{RO}}, \text{max. } P_{\text{RO}}$
AC Stark shift meas.	$\nu_{\text{RO}}$	$P_{\text{RO}}$	$\sim \nu_{\text{q}}$	CW at $\nu_{\text{RO}}$	$\nu_{\text{q}}, \Delta, g, \text{cal. of } P_{\text{RO}}$
Higher qubit levels	$\nu_{\text{RO}}, P_{\text{RO}}$	$P_{\text{d}}$	$\sim \nu_{\text{q}}$	CW at $\nu_{\text{RO}}$	$E_{\text{C}}, \alpha, E_{\text{J}}, I_{\text{c}}, C$
Sidebands	$\nu_{\text{RO}}, P_{\text{RO}}, \nu_{\text{q}}$	$P_{\text{d}}$	$\sim \nu_{\text{b}}$	CW at $\nu_{\text{RO}}$	$\nu_{\text{b}}$
Driven Rabi*	$\nu_{\text{RO}}, P_{\text{RO}}, \nu_{\text{q}}, (\alpha)^*$	$t_{\text{p}}$	transm. at $\nu_{\text{RO}}$	pulsed TD	$T_{\pi}$
Qubit decay*	$\nu_{\text{RO}}, P_{\text{RO}}, \nu_{\text{q}}, T_{\pi}, (\alpha)^*$	$\tau$	transm. at $\nu_{\text{RO}}$	pulsed TD	$T_1$
Qubit dephasing*	$\nu_{\text{RO}}, P_{\text{RO}}, \nu_{\text{q}}, T_{\pi}, (\alpha)^*$	$\tau$	transm. at $\nu_{\text{RO}}$	Ramsey or spin echo	$T_2$

**Table A.1:** Measurement strategy for characterization of a qubit-cavity system. (\* = IQ-modulated pulse generation with one additional AFG and PSG RF source)

### A.2 Band-pass filter for RF drive line

The drive of the BSB requires high-power pulses due to its second-order nature. This drive supposedly creates off-resonant cavity population, which causes the qubit frequency

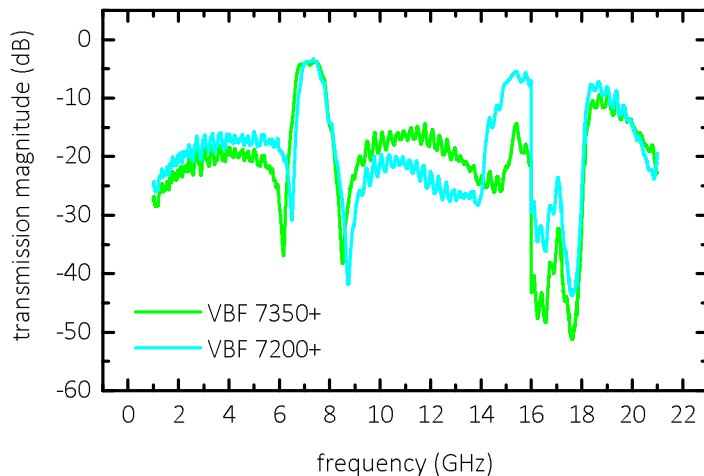


**Figure A.1:** Filter transmission characteristics of Mini Circuits VPF-7200+ and VPF-7350+.

to shift. To prevent this effect, we add band-pass filters to the BSB drive line, which have their passband around the drive frequency. The filters are added at room temperature in front of the output port of the Agilent E8267 PSG microwave source, where the pulsed RF signal is emitted. The transmission characteristics of these filters is measured with a VNA and shown in Fig. A.1.

### A.3 Direct measurement of coherent state decay

We measure the decay of a coherent state in the readout and the storage mode, respectively, by applying a microwave pulse at the required mode frequency. The duration of the pulse is longer than the ring up of the corresponding mode. We then use heterodyne detection with an IF frequency of 62.5 MHz to downconvert the signal for digitizing. The recording limit of our FPGA card is around 16  $\mu$ s. We observe a much noisier signal at the storage mode frequency due to bandwidth limitations of our HEMT amplifiers, which are limited to 4 to 8 GHz according to their specifications.

# Appendix B

## Sample overview

### B.1 Cavity samples

All single 3D cavities used in this work have inner dimensions and positions of the antenna insertion holes as depicted in Fig. 2.1. The material of the cavities is always Al, but differs in its purity (cf. Tab. B.1).

	Alloy cavity	Al cavity	pure Al cavity
Material	EN AW-2007	99.5% Al	99.99% Al

**Table B.1:** Summary of measured cavity samples. The Al alloy EN AW-2007 is a composition of 88 % to 93 % Al, 3.3 % to 4.6 % Cu,  $\leq 1.8$  % Mn,  $\leq 1.5$  % Pb, 0.8 % Fe, Si, Zn, 0.2 % Ni, Ti and 0.1 % Cr.

### B.2 Qubit samples

In Tab. B.2, we summarize measured qubits during the work of this thesis. Not all of them are mentioned in the main text. "QMv3 2<sup>nd</sup>" is the 2nd cooldown of the same sample. The last three qubits in the table are all built into one double cavity system with cavities C1 and C2. The bridge qubit is connected to both and characterized using C1. In Fig. B.1, we show a photograph of the opened double cavity system with the technical drawing in Fig. B.2.

### B.3 Sample fabrication recipe

The cavity is made in the in-house workshop out of 99.5 % bulk aluminum. The slim cavity connector is a 100  $\mu\text{m}$  gold wire soldered onto the tip of a commercial connector. We fabricate the transmon qubit on a silicon substrate with standard electron-beam lithography. For shadow evaporation of the Josephson junctions we use a double layer resist system of 700 nm PMMA 33 % and 70 nm PMMA 950K. Development is done

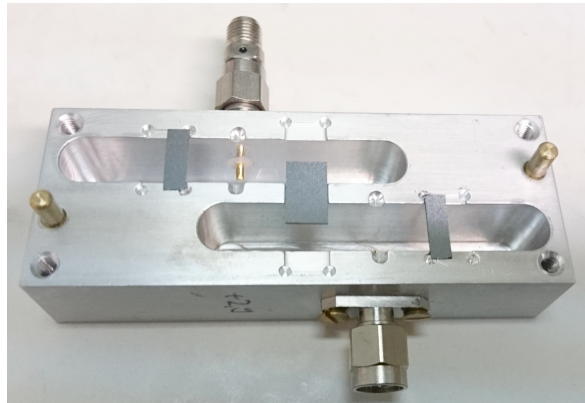


**Figure B.1:** Photograph of opened double cavity system with 3 qubit chips. On the center chip is the bridge qubit. All three chips are viewed from their unpolished backside.

first with AR600-56 for 30 s at room temperature and followed by IPA for 20 min at 4 °C. We evaporate a bottom layer Al of 50 nm, then oxidize in pure oxygen for 70 min at a constant pressure of  $7.85 \cdot 10^{-3}$  mbar. The top layer is 70 nm Al. The lift-off process is performed in Acetone at 70 °C.

	TQ1	QMv3 1 <sup>st</sup>	QMv3 2 <sup>nd</sup>	QMv4 1 <sup>st</sup>	QMv4 2 <sup>nd</sup>	QMv4 3 <sup>rd</sup>	C1	B	C2
qubit chip position	center	off-center (asymm.)	off-center (symm.)	off-center (asymm.)	off-center (asymm.)	off-center (symm.)	double cavity	bridge qubit	double cavity
$\nu_q$ (GHz)	3.650	7.602	6.234	5.284	5.36	5.203	6.310	3.871	7.402
$\alpha/h$ (MHz)	-168	-190	-187	-301	-300	-317	-694	-92	-821
$E_J/E_C$	60	206	142	37.8	40	33.9	9.1	221	10.09
$T_1$ ( $\mu$ s)	-	2.8	1.3	-	0.159	0.2	0.64	2.47*	-
$T_2$ ( $\mu$ s)	-	3.4	2.5	-	-	-	-	0.37	-
$\nu_{RO}$ (GHz)	5.462	5.604	5.518	5.485	5.485	5.4785	5.7154	5.717	5.7244
FWHM <sub>RO</sub> (MHz)	0.3	2.844	4	19	19	21.5	16.5	16.5	17
$\chi'_{RO}$ (MHz)	1.18	2	3.6	-8	-8	-5.5	1.5	-2	0.55
$g_{RO}/2\pi$ (MHz)	49.3	62.3	53	40	31.6	39.3	29.9	60.8	30.4
$\Delta_{q,RO}/2\pi$ (GHz)	1.8	1.944	0.716	-0.2	-0.13	-0.3	0.595	-1.847	1.678
$\nu_s$ (GHz)	-	8.904	8.707546	-	8.454	8.6371	7.696	-	7.726
FWHM <sub>s</sub> (kHz)	-	39	24.7	-	42	48	776	-	555
$\chi'_s$ (MHz)	-	-	-1.1	-	-	-	-	-	-
$g_s/2\pi$ (MHz)	-	-	53	-	-	-	-	-	-
$\Delta_{q,s}/2\pi$ (GHz)	-	-1.302	-2.474	-	-3.094	-3.434	-1.386	-	-0.324
$C$ (fF)	123	104	105	63.7	64.6	61.3	26.18	211	23.51
$I_c$ (nA)	20	76.7	53	23.1	24.1	21.6	13.54	41	16.7
$w_q$ ( $\mu$ m)	705	305	305	305	305	305	230	80	230
$l_q$ ( $\mu$ m)	760	760	760	760	760	760	760	7760	760
$g_q$ ( $\mu$ m)	50	50	50	50	50	50	50	50	50
$t_{ox}$ (s)					4200				
$p_{ox}$ ( $\mu$ bar)					7.85				

**Table B.2:** Summary of measured qubit samples. (\* = measured with DRAG). The QMv3 2<sup>nd</sup> sample has a 0.1 mm thin antenna. All other samples have the commercial Huber+Suhner 23.SMA-50-0-13 with a diameter of 1.6 mm. Between the cooldowns of QMv4 1st and QMv4 2nd, K&L 6L-250-12000 tubular low-pass filters are added to the QMv4 sample RF input and output lines, which leads to a rise in  $\nu_q$  and  $I_c$ .

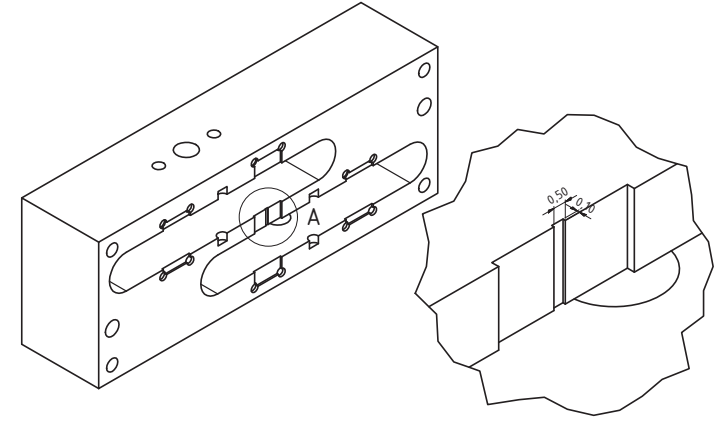
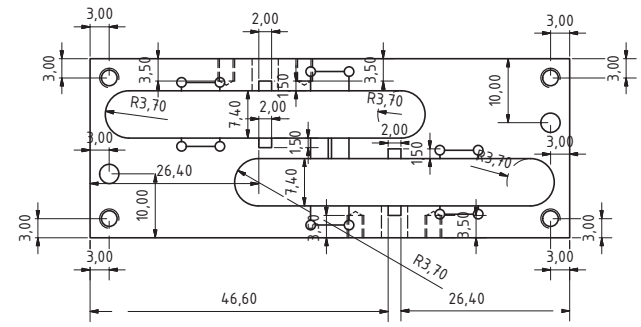
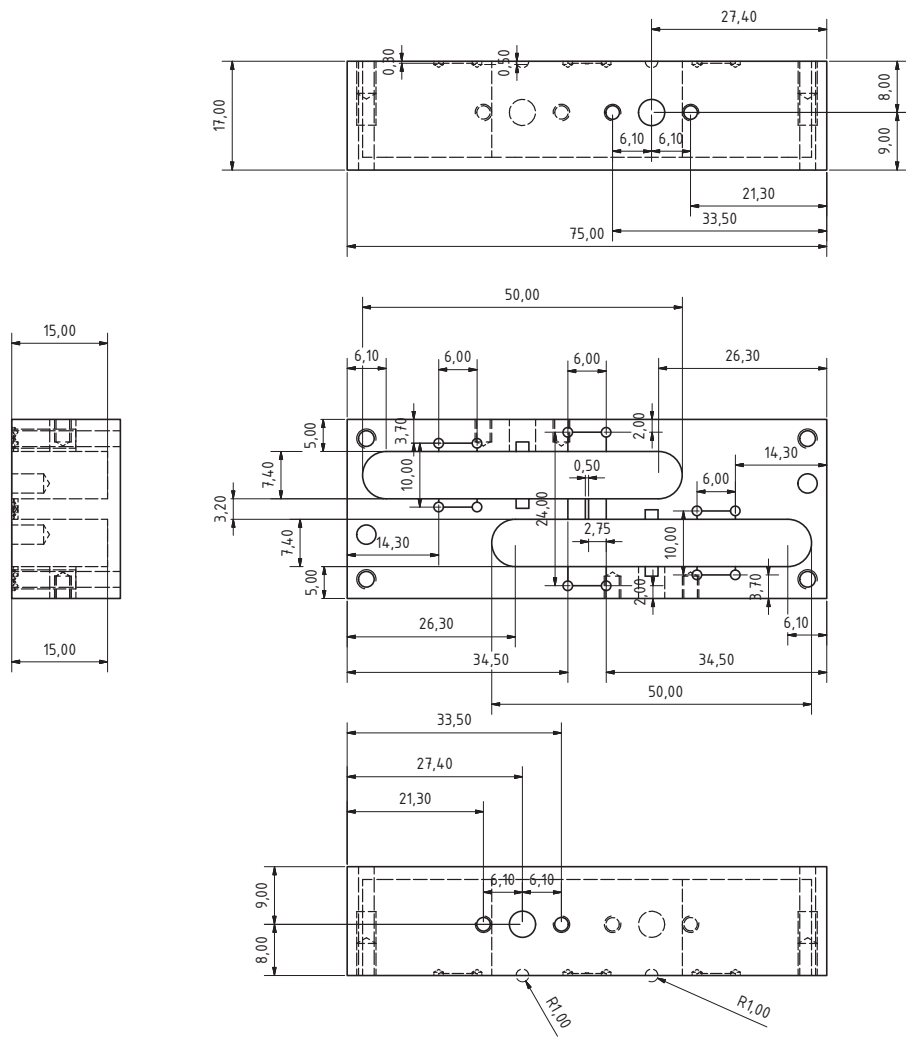


Figure B.2: CAD drawing of double cavity parts.

# Appendix C

## FEM simulation with CST

### C.1 Cavity simulation models

The FEM simulations with CST Microwave Studio [50] are based on the CAD drawings of the cavities [cf. Fig. C.1 (a)]. Typically, the cavity volume can also be modeled as a vacuum surrounded by PEC as depicted in Fig. C.1 (b). In a few cases, where the actual dimensions of the cavity are unimportant, such as in the simulation of the antenna coupling [cf. Fig. 2.2 (a)] or in the theoretical electric field distribution (cf. Fig. 1.1), we use a simple rectangular model without the semicircular edges [cf. Fig. C.1 (c)] to accelerate the simulation.

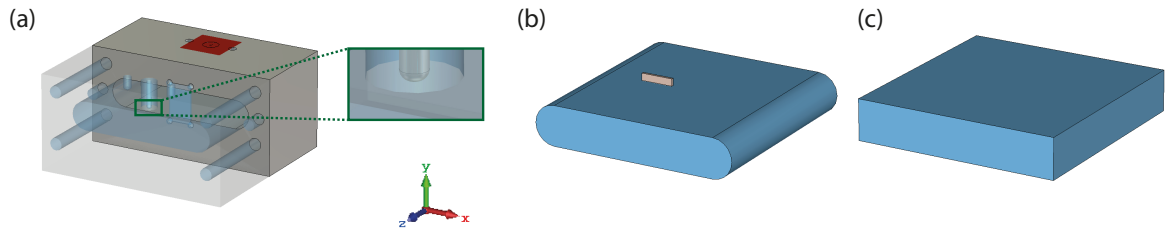


**Figure C.1:** (a) CST cavity model based on imported CAD file of cavity (SAT format). In the simulation software, the vacuum is depicted blue and PEC grey. The red rectangle on top is the waveguide port. The blowup is the antenna pin with rounded edges. (b) Cavity model with dimensions as described in Fig. 2.1. The vacuum is surrounded by PEC (not visible). The light brown structure in the center is the Si chip. (c) Simplified cavity model with  $a = 10$  mm,  $d = 10$  mm and  $b = 5$  mm.

The waveguide structure for the transmon qubit capacitance determination (cf. Sec. 2.1.2) has the same dimensions  $a$  and  $b$ , but  $d = 60$  mm. Here, it is especially important to create a local mesh for the transmon qubit capacitances due to the large difference in length scales of the waveguide ( 40 mm) and of the transmon qubit capacitances ( 100  $\mu$ m).

Since CST Microwave Studio [50] does not support the simulation of a superconductor, we always use PEC for the cavity casing and the antenna pins. If the transmon qubit chip

is necessary for the simulation, we insert a rectangular structure of the corresponding size and use Silicon with  $\epsilon_r = 11.9$  and  $\mu_r = 1$  as the material.

## C.2 Frequency solver

The frequency solver probes the cavity model in transmission through an input and output port, which are the antennas in our case. The waveguide ports in the frequency domain simulation are  $10 \times 10 \text{ mm}^2$  large (compared to an aperture diameter of 4.7 mm) in order to couple in all relevant frequencies. In the simulations, the antenna pins possess rounded edges in order to prevent the emergence of high electric fields at sharp corners [cf. Fig. C.1 (a)].

The results of the frequency solver are the scattering parameters (S-parameters) of the system for the specified frequency range. Hence, it can directly be compared with the results obtained via a VNA measurement. Furthermore, by defining a goal function and variable parameters, the frequency solver can be used to optimize the cavity dimensions to fit a desired mode frequency.

## C.3 Eigenmode solver

The eigenmode solver is a very efficient solver to determine the eigenmodes of the cavity and the corresponding electric and magnetic field distribution. Moreover, the surface current distribution is also obtained. To calculate in addition the external quality factor of the simulated eigenmodes, one has to define input and output waveguide ports similar to the those in frequency solver setup.

# Appendix D

## Maximum likelihood estimation

### D.1 MLE for the density matrix

Theoretically  $\hat{\rho}$  is physical, however, in experiment it is not always the case that positivity is guaranteed and there can be reconstructed states with  $\text{Tr}\hat{\rho}^2 > 1$ . The reason for this behavior is (thermal) noise caused by the environment or the experimental setup or systematic errors in the setup. If unphysical results are obtained, physicality can be enforced by using a maximum-likelihood-estimation (MLE) approach. This means that the physical density operator  $\tilde{\rho}$ , which has the highest probability to describe the system, is approximated with the measured  $\hat{\rho}$ . For a single qubit, the general form of a physical density matrix is given by

$$\tilde{\rho} = \frac{T^\dagger T}{\text{Tr}(T^\dagger T)}. \quad (\text{D.1})$$

with a matrix

$$T = \begin{pmatrix} t_1 & 0 \\ t_3 + it_4 & t_2 \end{pmatrix} \quad (\text{D.2})$$

where  $t_1, t_2, t_3, t_4 \in \mathbb{R}$  are the coefficients to be determined with the MLE.

If it is considered that  $\tilde{\varphi}_{x,y,z}$  are the phases that yield the physical density matrix  $\tilde{\rho}$ , we get according to the relation Eq. (2.25)

$$\tilde{\varphi}_x = \bar{\varphi} - \frac{\text{Tr}(\tilde{\rho}X)}{2}(\varphi_0 - \varphi_1) \quad (\text{D.3})$$

$$\tilde{\varphi}_y = \bar{\varphi} - \frac{\text{Tr}(\tilde{\rho}Y)}{2}(\varphi_0 - \varphi_1) \quad (\text{D.4})$$

$$\tilde{\varphi}_z = \bar{\varphi} + \frac{\text{Tr}(\tilde{\rho}Z)}{2}(\varphi_0 - \varphi_1). \quad (\text{D.5})$$

These equations depend on the yet unknown parameters  $t_1, t_2, t_3, t_4$ . The  $\tilde{\varphi}_{x,y,z}$  are now chosen such that the probability of the  $\tilde{\varphi}_{x,y,z}$  representing the actual physical mean

values is maximized.

$$P(t_1, t_2, t_3, t_4) = \mathcal{N} \prod_{i=x,y,z} \prod_{j=1}^N \exp \left[ -\frac{(\varphi_i^{(j)} - \tilde{\varphi}_i)^2}{2\sigma_i^2} \right] \quad (\text{D.6})$$

$\mathcal{N}$  is a constant for normalization. Mathematically, the problem can be reformulated as a minimization problem of the function

$$\mathcal{L}(t_1, t_2, t_3, t_4) = \sum_{i=x,y,z} \sum_{j=1}^N \frac{(\varphi_i^{(j)} - \tilde{\varphi}_i)^2}{2\sigma_i^2} \quad (\text{D.7})$$

Furthermore, it can be shown that the minimum of this function is identical to the minimum of

$$\mathfrak{L}(t_1, t_2, t_3, t_4) = \sum_{i=x,y,z} \frac{1}{2\sigma_i^2} (\tilde{\varphi}_i - \varphi_i)^2 \quad (\text{D.8})$$

from which the parameters  $t_1, t_2, t_3, t_4$ , which yield the optimal physical  $\tilde{\rho}$ , are obtained.

## D.2 MLE for the process matrix

For the same reasons as in QST, it may occur that the  $\hat{\chi}$ -matrix does not satisfy the physicality conditions. Again, a MLE approach is necessary to determine the optimal physical process matrix  $\tilde{\chi}$ , which describes the quantum operation best. To guarantee that  $\tilde{\chi}$  is positive Hermitian, we choose the ansatz:

$$\tilde{\chi}(t) = T(t)^\dagger T(t) \quad (\text{D.9})$$

with a lower triangular matrix  $T$  that depends on  $d^4$  parameters  $t_i \in \mathbb{R}$  and  $\vec{t} = (t_1, \dots, t_{d^4})$ . For the single qubit case with  $d = 2$ , this matrix is given as

$$T = \begin{pmatrix} t_1 & 0 & 0 & 0 \\ t_5 + it_6 & t_2 & 0 & 0 \\ t_{11} + it_{12} & t_7 + it_8 & t_3 & 0 \\ t_{15} + it_{16} & t_{13} + it_{14} & t_9 + it_{10} & t_4 \end{pmatrix}. \quad (\text{D.10})$$

The minimization problem consists of minimizing the distance  $\Delta$  of  $\chi$  and  $\tilde{\chi}$  under the trace preserving constraint ( $\sum_{m,n} B_m \hat{\chi}_{mn} B_n^\dagger = I$ ). It is expressed as

$$\Delta(\vec{t}) = \sum_{m,n} |\tilde{\chi}_{mn}(\vec{t}) - \chi_{mn}|^2 + \lambda \left| \sum_{m,n} B_m^\dagger \tilde{\chi}_{mn}(\vec{t}) B_n - I \right|^2 \quad (\text{D.11})$$

with a Lagrange multiplier  $\lambda$ . For better practical implementation, a vector quantity that contains all basis matrices is defined.

$$\mathbf{B} \equiv (B_1^\dagger, \dots, B_{d^2}^\dagger) \quad (\text{D.12})$$

Hence, the problem can be reformulated as

$$\Delta(t) = \|\tilde{\chi}(t) - \hat{\chi}\|_F^2 + \lambda \|\mathbf{B} \cdot (\tilde{\chi}(t) \otimes I) \cdot \mathbf{B}^\dagger - I\|_F^2 \quad (\text{D.13})$$

where  $\|\cdot\|_F$  denotes the Frobenius norm and  $\otimes$  is the Kronecker product. This optimization was performed using the `fminsearch()` function in Matlab<sup>®</sup>, but the trace-preserving condition was not fulfilled very well after convergence. As a result, trace-preserving was enforced before the minimization procedure. Again, for practical reasons, this condition is written in the form

$$M^\dagger(\vec{t})M(\vec{t}) = I \quad (\text{D.14})$$

with

$$M \equiv (T(t) \otimes I) \cdot \mathbf{B}. \quad (\text{D.15})$$

The optimization problem is then solved by minimizing

$$\Delta(t) = \|T^\dagger(t)T(t) - \hat{\chi}\|_F^2 \quad (\text{D.16})$$

under the constraint Eq. (D.14) using the `fmincon()` function in Matlab<sup>®</sup>. It is an important issue that the optimization problem for  $\Delta(\vec{t})$  is not convex in general, which means that many local minima may exist. The problem that the solving algorithm converges towards such a local minimum has to be avoided. This can be achieved by assuming that the physical process matrix  $\tilde{\chi}$  does only slightly differ from the measured unphysical matrix  $\hat{\chi}$ . Let  $\hat{\chi}_0$  denote the initial guess matrix for the minimization algorithm. Physicality of  $\hat{\chi}_0$  enforces the matrix can be decomposed in the way described in Eq. (D.9).

$$\hat{\chi}_0 = T_0(t)^\dagger T_0(t) \quad (\text{D.17})$$

This can be achieved via Cholesky decomposition [156]. In order to realize this,  $\hat{\chi}_0$  needs to be constructed as a positive definite matrix, which means that all eigenvalues have to be larger than 0. Let  $\{q_i\}$  be the set of the eigenvalues of the experimentally determined  $\hat{\chi}$ . A diagonal matrix  $D_0 = \text{diag}(p_1, \dots, p_{d^2})$  is constructed in the way

$$p_i = \begin{cases} q_i & \text{if } q_i > 0 \\ \varepsilon & \text{else} \end{cases} \quad (\text{D.18})$$

where  $\varepsilon > 0$  is a tolerance limit, which is set to double type machine precision ( $1.1 \cdot 10^{-16}$ ). Equation (2.33) is used in order to obtain an expression for  $\hat{\chi}_0$ , which is positive definite by construction and optimally close to the measured  $\hat{\chi}$ -matrix.

$$\chi_0 = UD_0U^\dagger \tag{D.19}$$

# Appendix E

## Additional measurement data

### E.1 Quantum state tomography and quantum process tomography of a single qubit

We obtain the following density matrices  $\hat{\rho}$ , which are depicted in Fig. 2.31.

For the  $|1\rangle$ -state:

$$\hat{\rho} = \begin{pmatrix} 0.0354 & 0.1841 - 0.0169i \\ 0.1841 + 0.0169i & 0.09646 \end{pmatrix} \quad \hat{\rho}_t = \begin{pmatrix} 0 & 0 \\ 0 & 1 \end{pmatrix} \quad F(\hat{\rho}, \hat{\rho}_t) = 0.9821$$

For the  $|+\rangle$ -state:

$$\hat{\rho} = \begin{pmatrix} 0.5372 & 0.4925 + 0.0778i \\ 0.4925 - 0.0778i & 0.4628 \end{pmatrix} \quad \hat{\rho}_t = \frac{1}{2} \begin{pmatrix} 1 & 1 \\ 1 & 1 \end{pmatrix} \quad F(\hat{\rho}, \hat{\rho}_t) = 0.9962$$

For the  $|-\rangle$ -state:

$$\hat{\rho} = \begin{pmatrix} 0.5850 & -0.0962 - 0.4832i \\ -0.0962 + 0.4832i & 0.4150 \end{pmatrix} \quad \hat{\rho}_t = \frac{1}{2} \begin{pmatrix} 1 & -i \\ i & 1 \end{pmatrix} \quad F(\hat{\rho}, \hat{\rho}_t) = 0.9916$$

We obtain the following process matrices  $\hat{\chi}$ -matrices, which are depicted in Fig. 2.33.

For the identity operation:

$$\hat{\chi} = \begin{pmatrix} 0.9480 & -0.0118i & 0 & 0 \\ 0.0118i & 0.0520 & 0 & 0 \\ 0 & 0 & 0 & 0 \\ 0 & 0 & 0 & 0 \end{pmatrix}$$

$$\hat{\chi}_t = \begin{pmatrix} 1 & 0 & 0 & 0 \\ 0 & 0 & 0 & 0 \\ 0 & 0 & 0 & 0 \\ 0 & 0 & 0 & 0 \end{pmatrix}$$

$$F(\hat{\chi}, \hat{\chi}_t) = 0.9737$$

For the  $R_y\left(\frac{\pi}{2}\right)$  - operation:

$$\hat{\chi} = \begin{pmatrix} 0.4538 & -0.0023 - 0.2252i & 0.3671 - 0.0006i & 0.0004 + 0.0286i \\ -0.0023 + 0.2252i & 0.1435 & -0.0004 + 0.1337i & -0.0151 + 0.0006i \\ 0.3671 + 0.0006i & -0.0004 - 0.1337i & 0.3975 & -0.0023 + 0.0260i \\ 0.0004 - 0.0286i & -0.0151 - 0.0006i & -0.0023 - 0.0260i & 0.0053 \end{pmatrix}$$

$$\hat{\chi}_t = \frac{1}{2} \begin{pmatrix} 1 & 0 & 1 & 0 \\ 0 & 0 & 0 & 0 \\ 1 & 0 & 1 & 0 \\ 0 & 0 & 0 & 0 \end{pmatrix}$$

$$F(\hat{\chi}, \hat{\chi}_t) = 0.8903$$

For the  $R_x\left(\frac{\pi}{2}\right)$  - operation:

$$\hat{\chi} = \begin{pmatrix} 0.4927 & 0.0108 - 0.3536i & -0.0191 - 0.0071i & -0.0200 - 0.0396i \\ 0.0108 + 0.3536i & 0.4509 & 0.0200 - 0.0176i & 0.0401 + 0.0071i \\ -0.0191 + 0.0071i & 0.0200 + 0.0176i & 0.0109 & 0.0108 + 0.0128i \\ -0.0200 + 0.0396i & 0.0401 - 0.0071i & 0.0108 - 0.0128i & 0.0455 \end{pmatrix}$$

$$\hat{\chi}_t = \frac{1}{2} \begin{pmatrix} 1 & -i & 0 & 0 \\ i & 1 & 0 & 0 \\ 0 & 0 & 0 & 0 \\ 0 & 0 & 0 & 0 \end{pmatrix}$$

$$F(\hat{\chi}, \hat{\chi}_t) = 0.9085$$

## E.2 Quantum process tomography of the quantum memory protocol

We perform quantum process tomography on the memory protocol with an initial state  $|g0\rangle$ . We choose a total protocol length of  $t_p = 332$  ns. In order to obtain the process matrix  $\hat{\chi}$ , we need to measure the density matrix  $\hat{\rho}$  using quantum state tomography

before and after the memory operation. Quantum state tomography is done using the set of independent states  $|e\rangle, |g\rangle, |-\rangle$  and  $|+\rangle$ . We use the maximum likelihood estimation to enforce physicality for the  $\hat{\rho}$  and  $\hat{\chi}$  matrices. The fidelity is defined as  $F_{\text{QPT}} = \text{Tr} \sqrt{\sqrt{\hat{\chi}} \hat{\chi}_t \sqrt{\hat{\chi}}}$ , where  $\hat{\chi}_t$  is the ideal process matrix. For our memory application, this  $\hat{\chi}_{\text{id}}$  coincides with  $I$  (cf. Fig. 2.33). Here, we show the  $\hat{\chi}$  and the  $\hat{\chi}_t$  matrices.

$$\hat{\chi} = \begin{pmatrix} 0.6115 & -0.0054 - 0.0305i & -0.0015 - 0.0047i & -0.0002 + 0.0008i \\ -0.0054 + 0.0305i & 0.2761 & 0.0002 - 0.1263i & 0.0044 + 0.0047i \\ -0.0015 + 0.0047i & 0.0002 + 0.1263i & 0.1118 & -0.0054 + 0.0047i \\ -0.0002 - 0.0008i & 0.0044 - 0.0047i & -0.0054 - 0.0047i & 0.0005 \end{pmatrix}$$

$$\hat{\chi}_t = \begin{pmatrix} 1 & 0 & 0 & 0 \\ 0 & 0 & 0 & 0 \\ 0 & 0 & 0 & 0 \\ 0 & 0 & 0 & 0 \end{pmatrix}$$



# Bibliography

- [1] J. Vansina, *Oral Tradition as History* (James Currey, 1985).
- [2] M. Lyons and R. Marquilhas, *Approaches to the History of Written Culture: A World Inscribed*, New Directions in Book History (Springer International Publishing, 2017).
- [3] E. Eisenstein, *The Printing Press as an Agent of Change* (Cambridge University Press, 1980).
- [4] J. Von Neumann, *Die Rechenmaschine und das Gehirn*, Scientia Nova Series (Oldenbourg, 1991).
- [5] W. K. Wootters and W. H. Zurek, “A single quantum cannot be cloned”, [Nature](#) **299**, 802 (1982).
- [6] L. Hartmann, I. Goychuk, M. Grifoni, and P. Hänggi, “Driven tunneling dynamics: Bloch-Redfield theory versus path-integral approach”, [Phys. Rev. E](#) **61**, R4687 (2000).
- [7] M. Schlosshauer, “Decoherence, the measurement problem, and interpretations of quantum mechanics”, [Rev. Mod. Phys.](#) **76**, 1267 (2005).
- [8] C. H. Bennett and D. P. DiVincenzo, “Quantum information and computation”, [Nature](#) **404**, 247 (2000).
- [9] L. M. Vandersypen, M. Steffen, G. Breyta, C. S. Yannoni, M. H. Sherwood, and I. L. Chuang, “Experimental realization of Shor’s quantum factoring algorithm using nuclear magnetic resonance.”, [Nature](#) **414**, 883 (2001).
- [10] L. K. Grover, in *Proceedings of the Twenty-eighth Annual ACM Symposium on Theory of Computing* (ACM, New York, NY, USA, 1996), STOC ’96, pp. 212–219.
- [11] P. W. Shor, “Polynomial-Time Algorithms for Prime Factorization and Discrete Logarithms on a Quantum Computer”, [SIAM Review](#) **41**, 303 (1999).
- [12] A. Furusawa, J. L. Sørensen, S. L. Braunstein, C. A. Fuchs, H. J. Kimble, and E. S. Polzik, “Unconditional Quantum Teleportation”, [Science](#) **282**, 706 (1998).

- 
- [13] R. Di Candia, K. Fedorov, L. Zhong, S. Felicetti, E. Menzel, M. Sanz, F. Deppe, A. Marx, R. Gross, and E. Solano, “Quantum teleportation of propagating quantum microwaves”, *EPJ Quant. Tech.* **2**, 25 (2015).
- [14] L. Lamata, “Digital-analog quantum simulation of generalized Dicke models with superconducting circuits”, *Sci. Rep.* **7**, 43768 (2017).
- [15] A. K. Ekert, “Quantum cryptography based on Bell’s theorem”, *Phys. Rev. Lett.* **67**, 661 (1991).
- [16] D. Schuster, “Circuit Quantum Electrodynamics”, Ph.D. thesis, Yale University (2007).
- [17] A. Wallraff, D. I. Schuster, A. Blais, L. Frunzio, R.-S. Huang, J. Majer, S. Kumar, S. M. Girvin, and R. J. Schoelkopf, “Strong coupling of a single photon to a superconducting qubit using circuit quantum electrodynamics”, *Nature* **431**, 162 (2004).
- [18] G. Wendin, “Quantum information processing with superconducting circuits: a review”, *Rep. Prog. Phys.* **80**, 106001 (2017).
- [19] C. Vu, “IBM Announces Advances to IBM Quantum Systems & Ecosystem”, (2017), URL <https://www-03.ibm.com/press/us/en/pressrelease/53374.wss{#}resource>.
- [20] J. M. Raimond, M. Brune, and S. Haroche, “Colloquium: Manipulating quantum entanglement with atoms and photons in a cavity”, *Rev. Mod. Phys.* **73**, 565 (2001).
- [21] H. Paik, D. I. Schuster, L. S. Bishop, G. Kirchmair, G. Catelani, A. P. Sears, B. R. Johnson, M. J. Reagor, L. Frunzio, L. I. Glazman, S. M. Girvin, M. H. Devoret, and R. J. Schoelkopf, “Observation of High Coherence in Josephson Junction Qubits Measured in a Three-Dimensional Circuit QED Architecture”, *Phys. Rev. Lett.* **107**, 240501 (2011).
- [22] A. Blais, R.-S. Huang, A. Wallraff, S. M. Girvin, and R. J. Schoelkopf, “Cavity quantum electrodynamics for superconducting electrical circuits: An architecture for quantum computation”, *Phys. Rev. A* **69**, 062320 (2004).
- [23] H. Padamsee, *RF Superconductivity: Science, Technology, and Applications*, RF Superconductivity (Wiley, 2009).
- [24] W. Weingarten, *Superconducting Cavities* (World Scientific, 2013), pp. 363–382.

- [25] M. H. Devoret and R. J. Schoelkopf, “Superconducting Circuits for Quantum Information: An Outlook”, *Science* **339**, 1169 (2013).
- [26] K. Juliusson, “Quantum Zeno Dynamics in 3D Circuit-QED”, Ph.D. thesis, Université Pierre et Marie Curie - Paris (2016).
- [27] S. Hacoen-Gourgy, L. P. García-Pintos, L. S. Martin, J. Dressel, and I. Siddiqi, “Incoherent Qubit Control Using the Quantum Zeno Effect”, *Phys. Rev. Lett.* **120**, 020505 (2018).
- [28] Y. Tabuchi, S. Ishino, A. Noguchi, T. Ishikawa, R. Yamazaki, K. Usami, and Y. Nakamura, “Coherent coupling between a ferromagnetic magnon and a superconducting qubit”, *Science* **349**, 405 (2015).
- [29] A. Narla, K. M. Sliwa, M. Hatridge, S. Shankar, L. Frunzio, R. J. Schoelkopf, and M. H. Devoret, “Wireless Josephson amplifier”, *Appl. Phys. Lett.* **104**, 232605 (2014).
- [30] S. J. Weber, K. W. Murch, M. E. Kimchi-Schwartz, N. Roch, and I. Siddiqi, “Quantum trajectories of superconducting qubits”, *Comptes Rendus Physique* **17**, 766 (2016).
- [31] K. Juliusson, S. Bernon, X. Zhou, V. Schmitt, H. le Sueur, P. Bertet, D. Vion, M. Mirrahimi, P. Rouchon, and D. Esteve, “Manipulating Fock states of a harmonic oscillator while preserving its linearity”, *Phys. Rev. A* **94**, 063861 (2016).
- [32] W. Wang, L. Hu, Y. Xu, K. Liu, Y. Ma, S.-B. Zheng, R. Vijay, Y. P. Song, L.-M. Duan, and L. Sun, “Converting Quasiclassical States into Arbitrary Fock State Superpositions in a Superconducting Circuit”, *Phys. Rev. Lett.* **118**, 223604 (2017).
- [33] B. Vlastakis, G. Kirchmair, Z. Leghtas, S. E. Nigg, L. Frunzio, S. M. Girvin, M. Mirrahimi, M. H. Devoret, and R. J. Schoelkopf, “Deterministically Encoding Quantum Information Using 100-Photon Schrodinger Cat States”, *Science* **342**, 607 (2013).
- [34] C. Wang, Y. Y. Gao, P. Reinhold, R. W. Heeres, N. Ofek, K. Chou, C. Axline, M. Reagor, J. Blumoff, K. M. Sliwa, L. Frunzio, S. M. Girvin, L. Jiang, M. Mirrahimi, M. H. Devoret, and R. J. Schoelkopf, “A Schrödinger cat living in two boxes”, *Science* **352**, 1087 (2016).
- [35] S. Rosenblum, Y. Y. Gao, P. Reinhold, C. Wang, C. J. Axline, L. Frunzio, S. M. Girvin, L. Jiang, M. Mirrahimi, M. H. Devoret, and R. J. Schoelkopf, “A CNOT gate between multiphoton qubits encoded in two cavities”, *Nat. Comm.* **9**, 652 (2018).

- [36] H. Paik, A. Mezzacapo, M. Sandberg, D. T. McClure, B. Abdo, A. D. Córcoles, O. Dial, D. F. Bogorin, B. L. T. Plourde, M. Steffen, A. W. Cross, J. M. Gambetta, and J. M. Chow, “Experimental Demonstration of a Resonator-Induced Phase Gate in a Multiqubit Circuit-QED System”, *Phys. Rev. Lett.* **117**, 250502 (2016).
- [37] C. Axline, M. Reagor, R. Heeres, P. Reinhold, C. Wang, K. Shain, W. Pfaff, Y. Chu, L. Frunzio, and R. J. Schoelkopf, “An architecture for integrating planar and 3D cQED devices”, *Appl. Phys. Lett.* **109**, 042601 (2016).
- [38] W. Pfaff, C. J. Axline, L. D. Burkhardt, U. Vool, P. Reinhold, L. Frunzio, L. Jiang, M. H. Devoret, and R. J. Schoelkopf, “Controlled release of multiphoton quantum states from a microwave cavity memory”, *Nat. Phys.* **13**, 882 (2017).
- [39] C. J. Axline, L. D. Burkhardt, W. Pfaff, M. Zhang, K. Chou, P. Campagne-Ibarcq, P. Reinhold, L. Frunzio, S. M. Girvin, L. Jiang, M. H. Devoret, and R. J. Schoelkopf, “On-demand quantum state transfer and entanglement between remote microwave cavity memories”, *Nat. Phys.* (2018).
- [40] P. Campagne-Ibarcq, E. Zalusky-Geller, A. Narla, S. Shankar, P. Reinhold, L. Burkhardt, C. Axline, W. Pfaff, L. Frunzio, R. J. Schoelkopf, and M. H. Devoret, “Deterministic Remote Entanglement of Superconducting Circuits through Microwave Two-Photon Transitions”, *Phys. Rev. Lett.* **120**, 200501 (2018).
- [41] M. Reagor, W. Pfaff, C. Axline, R. W. Heeres, N. Ofek, K. Sliwa, E. Holland, C. Wang, J. Blumoff, K. Chou, M. J. Hatridge, L. Frunzio, M. H. Devoret, L. Jiang, and R. J. Schoelkopf, “Quantum memory with millisecond coherence in circuit QED”, *Phys. Rev. B* **94**, 014506 (2016).
- [42] C. Rigetti, J. M. Gambetta, S. Poletto, B. L. T. Plourde, J. M. Chow, A. D. Córcoles, J. A. Smolin, S. T. Merkel, J. R. Rozen, G. A. Keefe, M. B. Rothwell, M. B. Ketchen, and M. Steffen, “Superconducting qubit in a waveguide cavity with a coherence time approaching 0.1 ms”, *Phys. Rev. B* **86**, 100506 (2012).
- [43] P. J. Leek, M. Baur, J. M. Fink, R. Bianchetti, L. Steffen, S. Filipp, and A. Wallraff, “Cavity Quantum Electrodynamics with Separate Photon Storage and Qubit Readout Modes”, *Phys. Rev. Lett.* **104**, 100504 (2010).
- [44] M. Neeley, M. Ansmann, R. C. Bialczak, M. Hofheinz, N. Katz, E. Lucero, A. O’Connell, H. Wang, A. N. Cleland, and J. M. Martinis, “Process tomography of quantum memory in a Josephson-phase qubit coupled to a two-level state”, *Nat. Phys.* **4**, 523 (2008).
- [45] A. P. Reed, K. H. Mayer, J. D. Teufel, L. D. Burkhardt, W. Pfaff, M. Reagor, L. Sletten, X. Ma, R. J. Schoelkopf, E. Knill, and K. W. Lehnert, “Faithful

- conversion of propagating quantum information to mechanical motion”, *Nat. Phys.* **13**, 1163 (2017).
- [46] Y. Kubo, C. Grezes, A. Dewes, T. Umeda, J. Isoya, H. Sumiya, N. Morishita, H. Abe, S. Onoda, T. Ohshima, V. Jacques, A. Dréau, J.-F. Roch, I. Diniz, A. Auffeves, D. Vion, D. Esteve, and P. Bertet, “Hybrid Quantum Circuit with a Superconducting Qubit Coupled to a Spin Ensemble”, *Phys. Rev. Lett.* **107**, 220501 (2011).
- [47] X. Zhu, S. Saito, A. Kemp, K. Kakuyanagi, S.-i. Karimoto, H. Nakano, W. J. Munro, Y. Tokura, M. S. Everitt, K. Nemoto, M. Kasu, N. Mizuochi, and K. Semba, “Coherent coupling of a superconducting flux qubit to an electron spin ensemble in diamond”, *Nature* **478**, 221 (2011).
- [48] M. Steger, K. Saeedi, M. L. W. Thewalt, J. J. L. Morton, H. Riemann, N. V. Abrosimov, P. Becker, and H.-J. Pohl, “Quantum Information Storage for over 180 s Using Donor Spins in a  $^{28}\text{Si}$  “Semiconductor Vacuum””, *Science* **336**, 1280 (2012).
- [49] M. Reagor, H. Paik, G. Catelani, L. Sun, C. Axline, E. Holland, I. M. Pop, N. A. Masluk, T. Brecht, L. Frunzio, M. H. Devoret, L. Glazman, and R. J. Schoelkopf, “Reaching 10 ms single photon lifetimes for superconducting aluminum cavities”, *Appl. Phys. Lett.* **102**, 192604 (2013).
- [50] CST STUDIO SUITE [www.cst.com](http://www.cst.com).
- [51] E. Maxwell, “Conductivity of metallic surfaces at microwave frequencies”, *J. Appl. Phys.* **18**, 629 (1947).
- [52] D. M. Pozar, *Microwave Engineering* (John Wiley & Sons, Inc., 2012), 2nd ed.
- [53] R. Gross and A. Marx, *Applied Superconductivity: Josephson Effect and Superconducting Electronics* (WMI, 2011).
- [54] S. M. Girvin, *Circuit QED: superconducting qubits coupled to microwave photons* (Oxford University Press, 2014).
- [55] P. Tipler and G. Mosca, *Physik: für Wissenschaftler und Ingenieure* (Springer Berlin Heidelberg, 2014).
- [56] B. E. A. Saleh and M. C. Teich, *Fundamentals of Photonics* (Wiley, 2007), 2nd ed.
- [57] T. Niemczyk, F. Deppe, H. Huebl, E. P. Menzel, F. Hocke, M. J. Schwarz, J. J. Garcia-Ripoll, D. Zueco, T. Hümmer, E. Solano, A. Marx, and R. Gross, “Circuit

- quantum electrodynamics in the ultrastrong-coupling regime”, *Nat. Phys.* **6**, 772 (2010).
- [58] B. Aune, R. Bandelmann, D. Bloess, B. Bonin, A. Bosotti, M. Champion, C. Crawford, G. Deppe, B. Dwersteg, D. A. Edwards, H. T. Edwards, M. Ferrario, M. Fouaidy, P.-D. Gall, A. Gamp, A. Gössel, J. Graber, D. Hubert, M. Hüning, M. Juillard, T. Junquera, H. Kaiser, G. Kreps, M. Kuchnir, R. Lange, M. Leenen, M. Liepe, L. Lilje, A. Matheisen, W.-D. Möller, A. Mosnier, H. Padamsee, C. Paganì, M. Pekeler, H.-B. Peters, O. Peters, D. Proch, K. Rehlich, D. Reschke, H. Safa, T. Schilcher, P. Schmüser, J. Sekutowicz, S. Simrock, W. Singer, M. Tigner, D. Trines, K. Twarowski, G. Weichert, J. Weisend, J. Wojtkiewicz, S. Wolff, and K. Zapfe, “Superconducting TESLA cavities”, *Phys. Rev. Spec. Top. - Accel. Beams* **3**, 092001 (2000).
- [59] G. Catelani, J. Koch, L. Frunzio, R. J. Schoelkopf, M. H. Devoret, and L. I. Glazman, “Quasiparticle Relaxation of Superconducting Qubits in the Presence of Flux”, *Phys. Rev. Lett.* **106**, 077002 (2011).
- [60] J. Goetz, F. Deppe, M. Haeberlein, F. Wulschner, C. W. Zollitsch, S. Meier, M. Fischer, P. Eder, E. Xie, K. G. Fedorov, E. P. Menzel, A. Marx, and R. Gross, “Loss mechanisms in superconducting thin film microwave resonators”, *J. Appl. Phys.* **119**, 015304 (2016).
- [61] D. L. Creedon, M. Goryachev, N. Kostylev, T. B. Sercombe, and M. E. Tobar, “A 3D printed superconducting aluminium microwave cavity”, *Appl. Phys. Lett.* **109**, 032601 (2016).
- [62] Y. Nakamura, Y. A. Pashkin, and J. S. Tsai, “Coherent control of macroscopic quantum states in a single-Cooper-pair box”, *Nature* **398**, 786 (1999).
- [63] A. A. Houck, J. Koch, M. H. Devoret, S. M. Girvin, and R. J. Schoelkopf, “Life after charge noise: Recent results with transmon qubits”, *Quantum Inf. Process.* **8**, 105 (2009).
- [64] J. Koch, T. M. Yu, J. Gambetta, A. A. Houck, D. I. Schuster, J. Majer, A. Blais, M. H. Devoret, S. M. Girvin, and R. J. Schoelkopf, “Charge-insensitive qubit design derived from the Cooper pair box”, *Phys. Rev. A* **76**, 042319 (2007).
- [65] R. Barends, J. Kelly, A. Megrant, D. Sank, E. Jeffrey, Y. Chen, Y. Yin, B. Chiaro, J. Mutus, C. Neill, P. O’Malley, P. Roushan, J. Wenner, T. C. White, A. N. Cleland, and J. M. Martinis, “Coherent Josephson Qubit Suitable for Scalable Quantum Integrated Circuits”, *Phys. Rev. Lett.* **111**, 080502 (2013).

- [66] R. Versluis, S. Poletto, N. Khammassi, B. Tarasinski, N. Haider, D. J. Michalak, A. Bruno, K. Bertels, and L. DiCarlo, “Scalable Quantum Circuit and Control for a Superconducting Surface Code”, *Phys. Rev. Applied* **8**, 034021 (2017).
- [67] J. Kelly, “A Preview of Bristlecone, Google’s New Quantum Processor”, (2018), URL <https://research.googleblog.com/2018/03/a-preview-of-bristlecone-googles-new.html>.
- [68] R. Blatt and D. Wineland, “Entangled states of trapped atomic ions”, *Nature* **453**, 1008 (2008).
- [69] R. Blatt and C. F. Roos, “Quantum simulations with trapped ions”, *Nat. Phys.* **8**, 277 (2012).
- [70] S. Murmann, F. Deuretzbacher, G. Zürn, J. Bjerlin, S. M. Reimann, L. Santos, T. Lompe, and S. Jochim, “Antiferromagnetic Heisenberg Spin Chain of a Few Cold Atoms in a One-Dimensional Trap”, *Phys. Rev. Lett.* **115**, 215301 (2015).
- [71] A. C. Johnson, J. R. Petta, J. M. Taylor, A. Yacoby, M. D. Lukin, C. M. Marcus, M. P. Hanson, and A. C. Gossard, “Triplet-singlet spin relaxation via nuclei in a double quantum dot”, *Nature* **435**, 925 (2005).
- [72] S. Plugge, A. Rasmussen, R. Egger, and K. Flensberg, “Majorana box qubits”, *New Journal of Physics* **19**, 012001 (2017).
- [73] M. A. Nielsen and I. L. Chuang, *Quantum Computation and Quantum Information: 10th Anniversary Edition* (Cambridge University Press, 2011), 10th ed.
- [74] B. Josephson, “Possible new effects in superconductive tunnelling”, *Phys. Lett.* **1**, 251 (1962).
- [75] Y. Reshitnyk, M. Jerger, and A. Fedorov, “3D microwave cavity with magnetic flux control and enhanced quality factor”, *EPJ Quant. Tech.* **3**, 13 (2016).
- [76] Z. Chen, J. Kelly, C. Quintana, R. Barends, B. Campbell, Y. Chen, B. Chiaro, A. Dunsworth, A. G. Fowler, E. Lucero, E. Jeffrey, A. Megrant, J. Mutus, M. Neeley, C. Neill, P. J. J. O’Malley, P. Roushan, D. Sank, A. Vainsencher, J. Wenner, T. C. White, A. N. Korotkov, and J. M. Martinis, “Measuring and Suppressing Quantum State Leakage in a Superconducting Qubit”, *Phys. Rev. Lett.* **116**, 020501 (2016).
- [77] C. Cohen-Tannoudji, J. Dupont-Roc, and G. Grynberg, *Photons and atoms: introduction to quantum electrodynamics* (Wiley, 1989).

- [78] G. Andersson, “Circuit quantum electrodynamics with a transmon qubit in a 3D cavity”, Master’s thesis, TU München (2015).
- [79] D. I. Schuster, A. A. Houck, J. A. Schreier, A. Wallraff, J. M. Gambetta, A. Blais, L. Frunzio, J. Majer, B. Johnson, M. H. Devoret, S. M. Girvin, and R. J. Schoelkopf, “Resolving photon number states in a superconducting circuit”, [Nature](#) **445**, 515 (2007).
- [80] A. P. Sears, A. Petrenko, G. Catelani, L. Sun, H. Paik, G. Kirchmair, L. Frunzio, L. I. Glazman, S. M. Girvin, and R. J. Schoelkopf, “Photon shot noise dephasing in the strong-dispersive limit of circuit QED”, [Phys. Rev. B](#) **86**, 180504 (2012).
- [81] A. Blais, J. Gambetta, A. Wallraff, D. I. Schuster, S. M. Girvin, M. H. Devoret, and R. J. Schoelkopf, “Quantum-information processing with circuit quantum electrodynamics”, [Phys. Rev. A](#) **75**, 032329 (2007).
- [82] A. Wallraff, D. I. Schuster, A. Blais, J. M. Gambetta, J. Schreier, L. Frunzio, M. H. Devoret, S. M. Girvin, and R. J. Schoelkopf, “Sideband Transitions and Two-Tone Spectroscopy of a Superconducting Qubit Strongly Coupled to an On-Chip Cavity”, [Phys. Rev. Lett.](#) **99**, 050501 (2007).
- [83] S. E. Nigg, H. Paik, B. Vlastakis, G. Kirchmair, S. Shankar, L. Frunzio, M. H. Devoret, R. J. Schoelkopf, and S. M. Girvin, “Black-box superconducting circuit quantization.”, [Phys. Rev. Lett.](#) **108**, 240502 (2012).
- [84] G. Kirchmair, B. Vlastakis, Z. Leghtas, S. E. Nigg, H. Paik, E. Ginossar, M. Mirrahimi, L. Frunzio, S. M. Girvin, and R. J. Schoelkopf, “Observation of quantum state collapse and revival due to the single-photon Kerr effect”, [Nature](#) **495**, 205 (2013).
- [85] D. F. Walls and G. J. Milburn, “Effect of dissipation on quantum coherence”, [Phys. Rev. A](#) **31**, 2403 (1985).
- [86] G. Lindblad, “On the generators of quantum dynamical semigroups”, [Commun. Math. Phys.](#) **48**, 119 (1976).
- [87] H.-P. Breuer and F. Petruccione, *The Theory of Open Quantum Systems* (Oxford University Press, 2007).
- [88] A. G. Redfield, “The Theory of Relaxation Processes”, [Adv. Magn. Opt. Reson.](#) **1**, 1 (1965).
- [89] E. M. Purcell, “Spontaneous Emission Probabilities at Radio Frequencies”, [Phys. Rev.](#) **69**, 674 (1946).

- [90] K. L. Geerlings, “Improving Coherence of Superconducting Qubits and Resonators Improving Coherence of Superconducting Qubits and Resonators”, Ph.D. thesis, Yale University (2013).
- [91] J. Goetz, F. Deppe, P. Eder, M. Fischer, M. Müting, J. P. Martínez, S. Pogorzalek, F. Wulschner, E. Xie, K. G. Fedorov, A. Marx, and R. Gross, “Second-order decoherence mechanisms of a transmon qubit probed with thermal microwave states”, *Quant. Sci. Tech.* **2**, 025002 (2017).
- [92] G. M. Whitesides, J. K. Kriebel, and B. T. Mayers, *Nanoscale Assembly: Chemical Techniques* (Springer US, 2005).
- [93] E. Xie, “Investigation of Alternative Methods for Graphene Production”, Graduation project, Istanbul Technical University (2011).
- [94] W. M. Moreau, *Semiconductor Lithography* (Springer US, 1988).
- [95] E. P. Menzel, F. Deppe, M. Mariantoni, M. Á. Araque Caballero, A. Baust, T. Niemczyk, E. Hoffmann, A. Marx, E. Solano, and R. Gross, “Dual-path state reconstruction scheme for propagating quantum microwaves and detector noise tomography”, *Phys. Rev. Lett.* **105** (2010).
- [96] S. Pogorzalek, K. G. Fedorov, L. Zhong, J. Goetz, F. Wulschner, M. Fischer, P. Eder, E. Xie, K. Inomata, T. Yamamoto, Y. Nakamura, A. Marx, F. Deppe, and R. Gross, “Hysteretic flux response and nondegenerate gain of flux-driven josephson parametric amplifiers”, *Phys. Rev. Appl.* **8** (2017).
- [97] J. Müller, “3D Cavities for Circuit Quantum Electrodynamics”, Bachelor’s thesis, TU München (2014).
- [98] P. D. Desai, H. M. James, and C. Y. Ho, “Electrical Resistivity of Aluminum and Manganese”, *J. Phys. Chem. Ref. Data* **13**, 1131 (1984).
- [99] W. Hesse, *Aluminium-Werkstoff-Datenblätter* (Beuth Verlag, 2017), 7th ed.
- [100] D. J. Whitehouse, “Surface metrology”, *Meas. Sci. Technol.* **8**, 955 (1997).
- [101] C. M. Quintana, A. Megrant, Z. Chen, A. Dunsworth, B. Chiaro, R. Barends, B. Campbell, Y. Chen, I.-C. Hoi, E. Jeffrey, J. Kelly, J. Y. Mutus, P. J. J. O’Malley, C. Neill, P. Roushan, D. Sank, A. Vainsencher, J. Wenner, T. C. White, A. N. Cleland, and J. M. Martinis, “Characterization and reduction of microfabrication-induced decoherence in superconducting quantum circuits”, *Appl. Phys. Lett.* **105**, 062601 (2014).

- [102] H. Wang, M. Hofheinz, J. Wenner, M. Ansmann, R. C. Bialczak, M. Lenander, E. Lucero, M. Neeley, A. D. O’Connell, D. Sank, M. Weides, A. N. Cleland, and J. M. Martinis, “Improving the coherence time of superconducting coplanar resonators”, *Appl. Phys. Lett.* **95**, 233508 (2009).
- [103] J. Lederer, “Hohlraumresonator- und Qubitdesign für dreidimensionale Schaltkreisquantenelektrodynamik”, Bachelor’s thesis, TU München (2015).
- [104] S. T. Skacel, C. Kaiser, S. Wuensch, H. Rotzinger, A. Lukashenko, M. Jerger, G. Weiss, M. Siegel, and A. V. Ustinov, “Probing the density of states of two-level tunneling systems in silicon oxide films using superconducting lumped element resonators”, *Appl. Phys. Lett.* **106**, 022603 (2015).
- [105] A. Bruno, G. de Lange, S. Asaad, K. L. van der Enden, N. K. Langford, and L. DiCarlo, “Reducing intrinsic loss in superconducting resonators by surface treatment and deep etching of silicon substrates”, *Appl. Phys. Lett.* **106**, 182601 (2015).
- [106] P. Summer, “Characterization of superconducting coplanar waveguide resonators at millikelvin temperatures”, Master’s thesis, TU München (2014).
- [107] L. Wang, “Fabrication stability of Josephson junctions for superconducting qubits”, Master’s thesis, TU München (2015).
- [108] G. J. Dolan, “Offset masks for lift-off photoprocessing”, *Appl. Phys. Lett.* **31**, 337 (1977).
- [109] F. Sterr, “Optimization of Josephson Junction Nanofabrication for Superconducting Quantum Circuits”, Diploma thesis, TU München (2013).
- [110] E. Xie, “Optimized fabrication process for nanoscale Josephson junctions used in superconducting quantum circuits”, Master’s thesis, TU München (2013).
- [111] Allresist, “Positiv-PMMA E-Beamresists AR-P 630-670er”, (2014).
- [112] M. A. Mohammad, K. P. Santo, S. K. Dew, and M. Stepanova, “Study of the interaction of polymethylmethacrylate fragments with methyl isobutyl ketone and isopropyl alcohol”, *J. Vac. Sci. Technol.* **30**, 06FF11 (2012).
- [113] NanoBeam, “NanoBeam and Technology”, (2014).
- [114] A. Broers, A. Hoole, and J. Ryan, “Electron beam lithography - Resolution limits”, *Microelectron. Eng.* **32**, 131 (1996).
- [115] N. Anupongpaibool and S. Y. Lee, in *18th International Parallel and Distributed Processing Symposium, 2004. Proceedings.* (2004).

- [116] E. Rutherford, “The scattering of  $\alpha$  and  $\beta$  particles by matter and the structure of the atom”, [The London, Edinburgh, and Dublin Philosophical Magazine and Journal of Science](#) **21**, 669 (1911).
- [117] NanoBeam, “EB resist list”, (2014).
- [118] J. E. Boggio, “The pressure dependence of the oxidation of aluminum at 298 K”, [Surf. Sci.](#) **14**, 1 (1969).
- [119] I. M. Pop, T. Fournier, T. Crozes, F. Lecocq, I. Matei, B. Pannetier, O. Buisson, and W. Guichard, “Fabrication of stable and reproducible submicron tunnel junctions”, [J. Vac. Sci. Technol.](#) **30**, 010607 (2012).
- [120] J. Goetz, “The Interplay of Superconducting Quantum Circuits and Propagating Microwave States”, Ph.D. thesis, TU München (2017).
- [121] J. Bindslev Hansen, in *Nonlinear Supercond. Electron. Josephson Devices* (Springer US, Boston, MA, 1991), pp. 161–180.
- [122] R. Gross and A. Marx, *Festkörperphysik* (De Gruyter Oldenbourg, 2012).
- [123] D. Repp, “Towards a compact 3D quantum memory”, Bachelor’s thesis, TU München (2016).
- [124] A. Abragam, *Principles of Nuclear Magnetism* (Oxford University Press, 1983).
- [125] H. Nyquist, “Thermal Agitation of Electric Charge in Conductors”, [Phys. Rev.](#) **32**, 110 (1928).
- [126] C. E. Shannon, “Communication in the Presence of Noise”, [Proceedings of the IRE](#) **37**, 10 (1949).
- [127] I. N. Bronstein, K. A. Semendjajew, G. Musiol, and H. Mühlig, *Taschenbuch der Mathematik*, vol. 23 (Harri Deutsch, 2008).
- [128] R. Dorf, *The Electrical Engineering Handbook, Second Edition*, Electrical Engineering Handbook (Taylor & Francis, 1997).
- [129] R. Schmied, “Quantum state tomography of a single qubit: comparison of methods”, [Journal of Modern Optics](#) **63**, 1744 (2016).
- [130] S. Gantner, “Vector Modulation of Microwaves for Circuit QED Experiments”, Bachelor’s thesis, TU München (2013).
- [131] F. Deppe, “Superconducting flux quantum circuits: characterization, quantum coherence, and controlled symmetry breaking”, Ph.D. thesis, TU München (2009).

- [132] M. Howard, J. Twamley, C. Wittmann, T. Gaebel, F. Jelezko, and J. Wrachtrup, “Quantum process tomography and Linblad estimation of a solid-state qubit”, [New J. Phys.](#) **8**, 33 (2006).
- [133] K. Kraus, A. Böhm, J. D. Dollard, and W. H. Wootters, eds., *States, Effects, and Operations Fundamental Notions of Quantum Theory*, vol. 190 of *Lecture Notes in Physics*, Berlin Springer Verlag (1983).
- [134] F. Motzoi, J. M. Gambetta, P. Rebentrost, and F. K. Wilhelm, “Simple Pulses for Elimination of Leakage in Weakly Nonlinear Qubits”, [Phys. Rev. Lett.](#) **103**, 110501 (2009).
- [135] J. M. Gambetta, F. Motzoi, S. T. Merkel, and F. K. Wilhelm, “Analytic control methods for high-fidelity unitary operations in a weakly nonlinear oscillator”, [Phys. Rev. A](#) **83**, 012308 (2011).
- [136] F. Motzoi and F. K. Wilhelm, “Improving frequency selection of driven pulses using derivative-based transition suppression”, [Phys. Rev. A](#) **88**, 062318 (2013).
- [137] A. J. Sirois, M. A. Castellanos-Beltran, M. P. DeFeo, L. Ranzani, F. Lecocq, R. W. Simmonds, J. D. Teufel, and J. Aumentado, “Coherent-state storage and retrieval between superconducting cavities using parametric frequency conversion”, [Appl. Phys. Lett.](#) **106**, 172603 (2015).
- [138] K. Liu, Y. Xu, W. Wang, S.-B. Zheng, T. Roy, S. Kundu, M. Chand, A. Ranadive, R. Vijay, Y. Song, L. Duan, and L. Sun, “A twofold quantum delayed-choice experiment in a superconducting circuit”, [Science Advances](#) **3**, 5 (2017).
- [139] N. Ofek, A. Petrenko, R. Heeres, P. Reinhold, Z. Leghtas, B. Vlastakis, Y. Liu, L. Frunzio, S. M. Girvin, L. Jiang, M. Mirrahimi, M. H. Devoret, and R. J. Schoelkopf, “Extending the lifetime of a quantum bit with error correction in superconducting circuits”, [Nature](#) **536**, 441 (2016).
- [140] S. Gasparinetti, S. Berger, A. A. Abdumalikov, M. Pechal, S. Filipp, and A. J. Wallraff, “Measurement of a vacuum-induced geometric phase”, [Science Advances](#) **2**, 5 (2016).
- [141] E. Flurin, V. V. Ramasesh, S. Hacoheh-Gourgy, L. S. Martin, N. Y. Yao, and I. Siddiqi, “Observing Topological Invariants Using Quantum Walks in Superconducting Circuits”, [Phys. Rev. X](#) **7**, 031023 (2017).
- [142] J. Goetz, F. Deppe, K. G. Fedorov, P. Eder, M. Fischer, S. Pogorzalek, E. Xie, A. Marx, and R. Gross, “Parity-engineered light-matter interaction”, [ArXiv e-prints:1708.06405](#) (2017).

- [143] P. J. Leek, S. Filipp, P. Maurer, M. Baur, R. Bianchetti, J. M. Fink, M. Göppl, L. Steffen, and A. Wallraff, “Using sideband transitions for two-qubit operations in superconducting circuits”, *Phys. Rev. B* **79**, 180511 (2009).
- [144] C. Müller, J. Lisenfeld, A. Shnirman, and S. Poletto, “Interacting two-level defects as sources of fluctuating high-frequency noise in superconducting circuits”, *Phys. Rev. B* **92**, 035442 (2015).
- [145] X. Y. Jin, A. Kamal, A. P. Sears, T. Gudmundsen, D. Hover, J. Miloshi, R. Slattery, F. Yan, J. Yoder, T. P. Orlando, S. Gustavsson, and W. D. Oliver, “Thermal and Residual Excited-State Population in a 3D Transmon Qubit”, *Phys. Rev. Lett.* **114**, 240501 (2015).
- [146] C. Grezes, B. Julsgaard, Y. Kubo, W. L. Ma, M. Stern, A. Bienfait, K. Nakamura, J. Isoya, S. Onoda, T. Ohshima, V. Jacques, D. Vion, D. Esteve, R. B. Liu, K. Mølmer, and P. Bertet, “Storage and retrieval of microwave fields at the single-photon level in a spin ensemble”, *Phys. Rev. A* **92**, 020301 (2015).
- [147] Z. Wang, S. Shankar, Z. K. Mineev, P. Campagne-Ibarcq, A. Narla, and M. H. Devoret, “Cavity Attenuators for Superconducting Qubits”, [ArXiv:1807.04849](https://arxiv.org/abs/1807.04849) (2018).
- [148] O. Dial, D. T. McClure, S. Poletto, G. A. Keefe, M. B. Rothwell, J. M. Gambetta, D. W. Abraham, J. M. Chow, and M. Steffen, “Bulk and surface loss in superconducting transmon qubits”, *Supercond. Sci. Technol.* **29**, 044001 (2016).
- [149] D. F. Bogorin, D. T. McClure, M. Ware, and B. L. Plourde, “Copper Waveguide Cavities with Reduced Surface Loss for Coupling to Superconducting Qubits”, *IEEE Trans. Appl. Supercond.* **24**, 4 (2014).
- [150] J. M. Gambetta, C. E. Murray, Y. K. K. Fung, D. T. McClure, O. Dial, W. Shanks, J. W. Sleight, and M. Steffen, “Investigating Surface Loss Effects in Superconducting Transmon Qubits”, *IEEE Trans. Appl. Supercond.* **27**, 1 (2017).
- [151] J. M. Gambetta, J. M. Chow, and M. Steffen, “Building logical qubits in a superconducting quantum computing system”, *npj Quantum Information* **3**, 2 (2017).
- [152] R. K. Naik, N. Leung, S. Chakram, P. Groszkowski, Y. Lu, N. Earnest, D. C. McKay, J. Koch, and D. I. Schuster, “Random access quantum information processors using multimode circuit quantum electrodynamics”, *Nat. Comm.* **8**, 1904 (2017).
- [153] M. Leib and M. J. Hartmann, “Bose-Hubbard dynamics of polaritons in a chain of circuit quantum electrodynamics cavities”, *New J. Phys.* **12**, 093031 (2010).

- [154] A. Aspuru-Guzik, A. D. Dutoi, P. J. Love, and M. Head-Gordon, “Simulated quantum computation of molecular energies.”, *Science* **309**, 1704 (2005).
- [155] I. Buluta and F. Nori, “Quantum Simulators”, *Science* **326**, 108 (2009).
- [156] J. H. Wilkinson and C. Reinsch, *Handbook for Automatic Computation* (Springer-Verlag Berlin Heidelberg, 1971).

# List of publications

- [1] E. Xie, F. Deppe, M. Renger, D. Repp, P. Eder, M. Fischer, J. Goetz, S. Pogorzalek, K. G. Fedorov, A. Marx, and R. Gross, “Compact 3D quantum memory”, [Appl. Phys. Lett.](#) **112**, 202601 (2018).
- [2] P. Eder, T. Ramos, J. Goetz, M. Fischer, S. Pogorzalek, J. P. Martinez, E. P. Menzel, F. Loacker, E. Xie, J. J. Garcia-Ripoll, K. G. Fedorov, A. Marx, F. Deppe, and R. Gross, “Quantum probe of an on-chip broadband interferometer for quantum microwave photonics”, [Supercond. Sci. Technol.](#) **31**, 115002 (2018).
- [3] J. Goetz, F. Deppe, K. G. Fedorov, P. Eder, M. Fischer, S. Pogorzalek, E. Xie, A. Marx, and R. Gross, “Parity-Engineered Light-Matter Interaction”, [Phys. Rev. Lett.](#) **121**, 060503 (2018).
- [4] K. G. Fedorov, S. Pogorzalek, U. Las Heras, M. Sanz, P. Yard, P. Eder, M. Fischer, J. Goetz, E. Xie, K. Inomata, Y. Nakamura, R. Di Candia, E. Solano, A. Marx, F. Deppe, and R. Gross, “Finite-time quantum entanglement in propagating squeezed microwaves”, [Sci. Rep.](#) **8**, 6416 (2018).
- [5] S. Pogorzalek, K. G. Fedorov, L. Zhong, J. Goetz, F. Wulschner, M. Fischer, P. Eder, E. Xie, K. Inomata, T. Yamamoto, Y. Nakamura, A. Marx, F. Deppe, and R. Gross, “Hysteretic Flux Response and Nondegenerate Gain of Flux-Driven Josephson Parametric Amplifiers”, [Phys. Rev. Appl.](#) **8**, 024012 (2017).
- [6] J. Goetz, S. Pogorzalek, F. Deppe, K. G. Fedorov, P. Eder, M. Fischer, F. Wulschner, E. Xie, A. Marx, and R. Gross, “Photon Statistics of Propagating Thermal Microwaves”, [Phys. Rev. Lett.](#) **118**, 103602 (2017).
- [7] J. Goetz, F. Deppe, P. Eder, M. Fischer, M. Müting, J. P. Martinez, S. Pogorzalek, F. Wulschner, E. Xie, K. G. Fedorov, A. Marx, and R. Gross, “Second-order decoherence mechanisms of a transmon qubit probed with thermal microwave states”, [Quantum Sci. Technol.](#) **2**, 025002 (2017).
- [8] F. Wulschner, J. Goetz, F. R. Koessel, E. Hoffmann, A. Baust, P. Eder, M. Fischer, M. Haeberlein, M. J. Schwarz, M. Pernpeintner, E. Xie, L. Zhong, C. W. Zollitsch, B. Peropadre, J.-J. García Ripoll, E. Solano, K. G. Fedorov, E. P. Menzel, F. Deppe, A. Marx, and R. Gross, “Tunable coupling of transmission-line microwave resonators mediated by an rf SQUID”, [EPJ Quant. Technol.](#) **3**, 10 (2016).

- 
- [9] K. G. Fedorov, L. Zhong, S. Pogorzalek, P. Eder, M. Fischer, J. Goetz, E. Xie, F. Wulschner, K. Inomata, T. Yamamoto, Y. Nakamura, R. Di Candia, U. Las Heras, M. Sanz, E. Solano, E. P. Menzel, F. Deppe, A. Marx, and R. Gross, “Displacement of Propagating Squeezed Microwave States”, *Phys. Rev. Lett.* **117**, 020502 (2016).
- [10] A. Baust, E. Hoffmann, M. Haeberlein, M. J. Schwarz, P. Eder, J. Goetz, F. Wulschner, E. Xie, L. Zhong, F. Quijandría, D. Zueco, J.-J. G. Ripoll, L. García-Álvarez, G. Romero, E. Solano, K. G. Fedorov, E. P. Menzel, F. Deppe, A. Marx, and R. Gross, “Ultrastrong coupling in two-resonator circuit QED”, *Phys. Rev. B* **93**, 214501 (2016).
- [11] J. Goetz, F. Deppe, M. Haeberlein, F. Wulschner, C. W. Zollitsch, S. Meier, M. Fischer, P. Eder, E. Xie, K. G. Fedorov, E. P. Menzel, A. Marx, and R. Gross, “Loss mechanisms in superconducting thin film microwave resonators”, *J. Appl. Phys.* **119**, 015304 (2016).
- [12] M. Haeberlein, F. Deppe, A. Kurcz, J. Goetz, A. Baust, P. Eder, K. Fedorov, M. Fischer, E. P. Menzel, M. J. Schwarz, F. Wulschner, E. Xie, L. Zhong, E. Solano, A. Marx, J.-J. García-Ripoll, and R. Gross, “Spin-boson model with an engineered reservoir in circuit quantum electrodynamics”, arXiv:1506.09114 (2015).
- [13] A. Baust, E. Hoffmann, M. Haeberlein, M. J. Schwarz, P. Eder, J. Goetz, F. Wulschner, E. Xie, L. Zhong, F. Quijandría, B. Peropadre, D. Zueco, J.-J. García Ripoll, E. Solano, K. Fedorov, E. P. Menzel, F. Deppe, A. Marx, and R. Gross, “Tunable and switchable coupling between two superconducting resonators”, *Phys. Rev. B* **91**, 014515 (2015).

# Acknowledgments

谢 (*Xie*) is the Chinese character for "gratitude"

Most importantly, I am grateful to my *Lord and Savior Jesus Christ*, who has proven to be the light, that truly shines in darkness.

I am indebted to the director of the WMI, *Prof. Dr. Rudolf Gross*, for giving me the opportunity to complete my scientific career in the qubit group at the WMI. It all began during the Ferienakademie in 2009, continued with a Bachelor's thesis, a Master's thesis and now comes to an end in the form of a PhD thesis.

During that time, *Dr. Frank Deppe* was always a great help and guidance. You introduced me to the topic of quantum information processing, in the first place by explaining the working principle of a copper powder filter. I admire your practical lab skills including the construction and operation of a cryostat and laying pumptubes right below the WMI roof. On the theory side, you were always able to give sound answers to my (often naive) questions. I thank you for the discussions, your patience and profound supervision.

For proofreading and questions concerning cryostats or the elevator, I was always able to approach *Dr. Achim Marx*, who does a great job in managing all kind of matters at the WMI and the qubit group. Thank you very much for keeping everything running, especially during the massive reconstruction project.

I also express my gratitude for our postdocs *Dr. Hans Hübl* and *Dr. Kirill G. Fedorov* for their support and counsel in various ways. Moreover, I thank our post-postdocs *Dr. Kurt Uhlig* and *Dr. Christian Probst* for their unlimited knowledge about low-temperature technology and the construction of such devices. I learned a lot during the planning and the assembly of the new AK cryostat.

I really enjoyed working in the qubit group due to the down-to-earth colleagues. Many thanks go to *Stefan P.*, *Peter*, *Michael*, *Daniel*, *Stefan W.* and *Philip* for hints and practical help. Sharing instruments and thoughts has always been very easy. Special thanks go to *Peter*, with whom working in the lab was always fun and who saved the

Circus cryostat multiple times way after midnight.

At this point, I would particularly like to thank some of the former members of the qubit group, who paved the way (or lab, to be precise) for our qubit group generation. My measurements were distributed over all three labs, hence I might appreciate their work most. Thanks to *Manuel, Friedrich* and *Jan* we have a fully equipped Circus Lab with a working time-domain setup. *Max, Elly, Alex* and *Edwin* made tremendous effort in rebuilding the Qubit Lab, which deserves our gratitude. Furthermore, we thank *Ling* for her help setting up the K21 Lab. Thank you all for sharing your good and bad lab experiences and your knowledge about RF technology, cryogenics and LV programming.

The best officemate prize goes to *Kathrin, Hannes* and *Edwin*. You guys just left me all alone in the office with our two youngsters *Stefan W.* and *Lukas*. Thank you all for the comfortable office atmosphere and our common postcard/certificate/calendar/funny pictures wall.

My former bachelor and master students all did a great job and contributed significantly to this work. *Jonathan* analyzed the 3D cavities for the first time at the WMI. *Gustav* characterized the first 3D transmon qubit. *Lujun* set up a fabrication recipe using the new spin coater and the new e-beam system. *Jonas* worked out the transmon design process using CST Microwave Studio [50]. *Daniel* investigated the BSB transition. *Michael* implemented the QST and QPT procedure in the measurement setup. I wish all of you good luck with your own Master's/PhD thesis or other engagement.

I appreciate the work from our in-house workshop consisting of *Helmut, Georg, Christian, Alex* and formerly *Klaus* and *Robert*. There would be not a single 3D cavity, if you guys did not machine it with an unmatched precision. And thank you for the clues and tools for repairing my car.

I am obliged to *Tom, Sebastian, Sepp, Karen, Astrid* and *Christoph* for their immediate help regarding pumps, pressure sensors, helium gas bottles, chemicals, electronics and other major and minor technical issues. Moreover, I would like to thank you for keeping the whole clean room facility and fabrication devices in an up and running condition.

Talking about the clean room, I would like to thank *Maria* and *Sybilla* for making the WMI a pleasant place to work by keeping the offices and labs clean. I also enjoyed the nice chit-chat about children.

No low-temperature measurement would have been possible without the helium liquefaction team *Jan, Peter* and *Harald*, who also took care of the recovery line, if I

accidentally left it kind of open, or were generous with liquid helium, when I forgot to make a reservation.

Very helpful advice concerning all kind of organizational issues came from *Ludwig* and *Emel*. Thank you for handling my purchase orders, reimbursements, employment contracts and parental leaves always in time.

I thank my parents *You* and *Shenhua* for providing me with the possibility to study physics and to start my own family. I consider their good education and their everyday hard work as worthy of imitation.

Last but not least, I cordially thank my wife *Maria*, who willingly took care of our daughter and everything else when I was frequently absent in the lab. Thank you for your support, your faithfulness and your love. I also thank my little daughter *Clara* for cheering me up so often. And I thank you, my second little daughter *Lina*, for seeing the light of day not before I was able to finish the first version of this work.